TARGETING EARLY VASCULAR DYSFUNCTION FOLLOWING SPINAL CORD INJURY

Chen Chen

Submitted to the faculty of the University Graduate School
in partial fulfillment of the requirements
for the degree
Doctor of Philosophy
in the Program of Medical Neuroscience,
Indiana University

October 2019

Accepted by the Graduate Faculty of Indiana University, in partial fulfillment of the requirements for the degree of Doctor of Philosophy.

Doctoral Committee

Theodore R. Cummins, Ph.D, Chair

Xiaoming Jin, MS, Ph.D

May 15, 2019

Kathryn J. Jones, Ph.D, PT, FAAA

Karmen Yoder, Ph.D

Xiao-ming Xu, Ph.D

ACKNOWLEDGEMENTS

This dissertation represents a significant period in my life. I would not get to this point without the support of many people, to whom I would like to express my most enormous gratitude.

First and foremost, I would like to thank my mentor Dr. Xiao-ming Xu for his guidance and patience he has provided me throughout my doctoral training. He has been extraordinarily trusting and supportive of allowing me to explore my research interest since day one. I am also grateful to his consistent encouragement, especially when I am in doubt about myself. Beyond research, he has taught me how to be a better person who dares to fail but never forgets to smile and get back on track. Besides my mentor, I would also like to thank the rest of my thesis committee: Dr. Theodore Cummins, Dr. Kathryn Jones, Dr. Xiaoming Jin, and Dr. Karmen Yoder. I am gracious for their insightful comments and moral support, but also for the challenging questions which incented me to widen my research from various perspectives. Likewise, I owe a debt of gratitude to current and former the Stark Neuroscience Research Institute (SNRI) and Medical Neuroscience program staff members, especially Nastassia Belton and Diana Kelley, for keeping my paperwork up to date and in top form. I would also like to thank Indiana Spinal Cord and Traumatic Brain Injury Research Fund Grant Program to give generous support to my research project.

Among my coworkers, I especially want to thank Dr. Yan Sun for her extraordinary patience and generous support in helping me becoming an adequate scientific thinker and experimentalist. I thank Dr. Xiongwen Hui from Dr. Xiaoming Jin lab and Dr. Xiang Gao

from Dr. Jinhui Chen lab for their countless valuable time in teaching and troubleshooting with me on *in vivo* two-photon imaging protocols and confocal microscopy. Finally, I want to thank all the current and former lab members on the fifth floor of the Neuroscience Research Building for being part of my journey.

Along this journey, I would not have my sanities without my two great friends: Dr. Xingjie Ping and Dr. Xiaoting Wang. They have not only generously shared their wisdom, countless brainstorming, and constructive advice, but also always been there when I am up for a chat. I would also extend my appreciation to my fellow graduate students and friends, Liangping Li, Victoria Ma, Sreeparna Majumdar, Yuanyuan Chen, Marisol Resendiz, Chunxiang Wu, Yangshin Park, Jie Lan, and Baylen Ravenscraft. I consider myself extremely lucky to have these amazing friends along this journey and for life.

I want to save the last part to my dearest family close to my heart. My mom, dad, and grandma have been the best support system throughout all my life, and they have shaped me into the best person I could be. Special thanks go to all my family members, uncles, aunts, Xiao Tan, Yangzhi Zhao, Jessie Zhao, Fangjian Chen, Kevin Zhang, Yuki Takahashi, Heidi for their unwavering love and support.

Chen Chen

TARGETING EARLY VASCULAR DYSFUNCTION FOLLOWING SPINAL CORD INJURY

The vascular network highly coordinates with the central nervous system (CNS) on exchanging oxygen, nutrients and information transfer. The resemblance of the two systems at anatomical, cellular, and molecular levels also demonstrates their interdependence. The spinal cord is an integrated part of the CNS. Traumatic spinal cord injury (SCI) causes rapid systemic vascular responses and local neural tissue damage at the initial phase. The early disruption of the spinal vasculature breaks the supply-and-demand balance and facilitates the deterioration of the spinal cord tissue and functional deficits. Therefore, it is important to dissect the mechanism underlying vascular injury-mediated histological and functional consequences in order to develop potential therapeutic strategies.

To visualize dynamic vascular changes after an acute SCI, a novel duo-color *in vivo* imaging technique was successfully developed in adult rats at the cervical level. This technique overcomes previous technical hurdles allowing real-time observation of vascular changes in live animals. Correlated with histological measures, *in vivo* vascular outcomes revealed a temporospatial relationship with neuronal and axonal loss, myelin disruption, inflammation, and glial responses. For the first time, we defined a “transitional zone” where significant blood vessel dilation and vascular leakage were observed simultaneously with vascular changes occurred at the injury epicenter acutely after SCI. These vascular changes at the transitional zone happened before any other cellular damage after SCI, suggesting a time window to prevent further neuronal damage in this region. Targeting the observed vascular leakage can work as a proof of concept that early vascular dysfunction contributes to the secondary neural tissue damage. Indeed, intravenous delivery of ferulic acid conjugated with glycol chitosan (FA-GC) to the injured sites immediate after SCI resulted in reduced vascular leakage, ventral horn neuronal loss, and partial recovery of forelimb function following a clinically-relevant contusive SCI at the 7th cervical spinal cord level.

In conclusion, this work elucidated a novel role and mechanism of early vascular damage in the "transitional zone" prior to the secondary damage of neural tissue in this region and provided a novel treatment strategy for early neuroprotection and functional recovery.

Theodore R. Cummins, Ph.D, Chair

TABLE OF CONTENTS

List of Tables x

List of Figures xi

Chapter 1 INTRODUCTION 1

Overview 1

The vascular system of the spinal cord 2

Blood-CNS barrier 6

Subsequent vascular and inflammatory responses to SCI 11

Current limitation/challenge to study vascular injury 13

Current knowledge on the expansion of secondary injury 14

The knowledge gaps 15

Chapter 2 DEVELOPING A NOVEL IN VIVO IMAGING METHOD TO MONITOR DYNAMIC VASCULAR DAMAGES FOLLOWING ACUTE SPINAL CORD INJURY 17

Hypothesis 17

Introduction 17

Step-by-step procedure 19

Data analysis and representative results 26

Discussion 33

Chapter 3 CHARACTERIZATION OF A TEMPOROSPATIAL PROFILE IN DYNAMIC VASCULAR CHANGES CORRELATING WITH DIFFERENT CELLULAR CHANGES FOLLOWING A CERVICAL SPINAL CORD

INJURY 36

Hypotheses 36

Introduction 36

Materials and methods 38

Results 48

Discussion 69

Chapter 4 TARGETING VASCULAR LEAKAGE WITH INTRAVENOUS DELIVERY OF FERULIC ACID (FA) - GLYCOL CHITOSAN (GC) NANOPARTICLES FOLLOWING SPINAL CORD INJURY 75

Hypothesis 75

Introduction 75

Materials and methods 78

Results 86

Discussion 99

Chapter 5 CONCLUSIONS 103

Appendix 107

References 108

Curriculum Vitae

LIST OF TABLES

Table 2.1. Criteria for identifying vessel types 30

Table 2.2. List of materials for *in vivo* duo-color method 31

Table 3.1. Primary and secondary antibodies used in this study 43

LIST OF FIGURES

Figure 2.1. Jugular vein catheterization and spine stabilization 21

Figure 2.2. Schematic diagram of optic window installation step-by-step 23

Figure 2.3. The *in vivo* duo-color method procedure step-by-step 25

Figure 2.4. Acquisition and quantification of spinal vessel diameters 27

Figure 2.5. Measurement of vascular permeability 28

Figure 2.6. Acquisition and quantification of spinal vessel velocity 29

Figure 3.1. Immediate vascular dilation occurs simultaneously in the epicenter and the adjacent zone after SCI 49

Figure 3.2. Simultaneous increase of the vascular permeability in the epicenter and the transitional zone after SCI 52

Figure 3.3. Histological evidence of simultaneous leaky vessels in the epicenter and the transitional zone in the white matter 53

Figure 3.4. Histology also validates the vessel leakage in the gray matter 56

Figure 3.5. Neuronal loss lags vessel leakages in the transitional zone 58

Figure 3.6. Microglial activation also lags vascular changes in the transitional zone 60

Figure 3.7. Reactivation of astrocytes lags vascular changes in the gray matter 63

Figure 3.8. Axonal loss and myelin responses 66

Figure 3.9. The loss of oligodendrocytes parallels the timescale for myelin response 68

Figure 4.1. FA-GC nanoparticles exhibited long blood retention time and targeted delivery to injured spinal cord 77

Figure 4.2. FA-GC reduces vascular leakage but has no effect on the vessel diameter following C7 contusion SCI 87

Figure 4.3. FA-GC prevented neuronal loss of the ventral horn in the transitional zone 89

Figure 4.4. Experimental design and timeline for behavior assessments 91

Figure 4.5. Adhesive removal test 92

Figure 4.6. Grid walking 94

Figure 4.7. Modified grip strength 96

Figure 4.8. Rotarod 98

CHAPTER 1

INTRODUCTION

Overview

Spinal cord injury (SCI) is one of most challenging worldwide medical conditions that patients suffer either high mortality or lifelong disability accompanying with permanent and profound neurologic deficits (Singh et al., 2014, NSCISC, 2019). Following SCI, the integrity of vascular structures is disrupted (Benton and Hagg, 2011). Ultrastructural studies show vascular pathology minutes after SCI (Goodman et al., 1979, Koyanagi et al., 1993a) and this is consistent throughout the acute injury phase (Whetstone et al., 2003, Benton et al., 2008). In fact, blood vessel endothelial cells appear to be the first cells that are vulnerable to the insult from a contusive SCI (Griffiths et al., 1978, Casella et al., 2006). These immediate vascular events, including increased permeability of the blood-spinal cord-barrier (BSCB), induce edema and contribute to detrimental secondary injury events, resulting in histopathology and functional deficits (Benton et al., 2009a, Nelson et al., 1977). Since vascular injury is a hallmark of SCI, targeting its disruption may represent a promising strategy as the preservation of metabolic support of spinal tissue spared by the primary injury should result in an enhanced substrate for functional recovery (Benton et al., 2009a). To date, research on vascular injury and repair remains to be a largely underexplored therapeutic avenue and an urgent medical need.

To emphasize the necessity to study vascular injury following SCI, the following sections address a few fundamental topics. First, this chapter delivers an overview of the vascular supply of the spinal cord and the Blood-CNS barriers. Second, I cover the topics including vascular responses to SCI, and current limitations/challenge to study vascular injury, and knowledge gap. Finally, I go over the strategies I chose to tackle these research questions.

The vascular system of the spinal cord

The rat model highly resembles the human spinal cord blood supply except for minor differences. Therefore, it is frequently used as an experimental model for spinal cord injury. The normal vascular supply to the spinal cord can be divided into two main systems: the arterial supply and the venous drainage. The arterial supply system replenishes oxygen and nutrients, and the venous drainage system takes away carbon dioxide and waste products. These two systems connect via the capillary network in local tissues to fulfill the blood circulatory functions.

The segmental spinal branches support the major arterial supply to the spinal cord. The origins of the segmental spinal branches differ in different spinal cord regions. In the cervical spinal cord, the vertebral arteries (VA) give rises to segmental spinal branches. Both lateral VAs come from subclavian arteries. Posterior inferior cerebellar arteries (PICA) also supplies the most cranial part of the 1st segment of the cervical spinal cord. In the thoracolumbar region, segmental spinal branches arise from dorsal intercostal arteries (DIA) and lumbar arteries (LA), which mainly originate from the descending thoracic aorta and subclavian arteries (Mazensky et al., 2017). In this particular study of a cervical SCI, I mainly focus on the blood supply of the cervical spinal cord. The cervical segmental spinal branches, arising from the VAs, enter the spinal cord through the intervertebral foramina accompanied with the corresponding nerve roots. Some of the spinal branches divide into ventral spinal arteries (VSA) and dorsal spinal arteries (DSAs) extending in longitudinal direction. VSA is lying in the ventral median fissure, and DSAs are near the entry zone of dorsal root in gray matter. Small branches, budding from both VSA and DSAs, form a spinal arterial ring on the surface of the spinal cord (Turnbull, 1973). This constitutes the extrinsic arteries of the spinal cord. The intrinsic arterial system can be further categorized into a central and a peripheral circuit. In the central circuit, the sulcal arteries branch off the VSA and enter the central gray matter area to supply most of the spinal cord gray matter in a centrifugal direction. The peripheral circuit includes a centripetal blood flow coming from the extrinsic arteries to supply the peripheral part of the spinal cord via small perforating arteries (Griessenauer et al., 2015). In the cervical spinal cord, the supply from the peripheral and central systems are approximately equal (Turnbull, 1973). Most importantly, the gray matter often presents with a higher density of microvasculature compared to the white matter of the spinal cord. Also, the spinal cord is much less vascularized than the brain. This may contribute to the outcome of cavitation often seen after a spinal cord injury, but not a traumatic brain injury (Losey and Anthony, 2014).

The spinal venous network can be divided into intrinsic, extrinsic and extradural components. The intrinsic system is separated into central and peripheral sections. In the central section, there are two axially-orientated veins: dorsal sulcal vein (DSV) and ventral sulcal vein (VSV). These veins collect deoxygenated blood from nearby capillary networks. Unlike the ventral dominance presented in the arterial supply system, both the DSV and VSV drain equally from the spinal cord. The DSV drains from dorsal gray matter and white matter, while the VSV collects blood from a ventral part of gray matter and white matter. The number of sulcal veins varies along the length of the spinal cord. In the cervical spinal cord, VSV is 4-8 per cm with the vessel diameter ranging from 100 to 200 µm; DSV is 4-6 per cm with a diameter range of 100-300 µm (Moes and Maillot, 1981, Lasjaunias and A., 1990, Thron and Rossberg, 1988). In the peripheral section, these axially-orientated periphery forming radial veins drain blood from these capillaries from the peripheral part of white matter and gray matter. Together with sulcal veins, the radial veins form an intricate network of anastomoses with small branches within the central and peripheral sections. Besides the axially-orientated veins, there is also longitudinal intrinsic anastomosis in both gray and white matter. In the periphery, there is a structure called “intersegmental bridges” linking between radial veins at the spinal pial level. These bridges are considered the extrinsic venous system. The extrinsic venous system includes three components: pial venous network, the longitudinally-orientated extrinsic venous system (ventral median vein and dorsal median vein), and radicular veins. The first two are considered as collectors, draining from the intrinsic system. The radiculomedullary veins, also called radicular veins, connect the extrinsic to the extradural system and receive blood from the ventral or dorsal median veins (Santillan et al., 2012). The radicular veins then drain into the vertebral venous plexus via the spinal nerve venous channels (Lasjaunias and A., 1990). Although the radicular veins lack valves, they present narrow lumens and take an oblique and tortuous course along the dura, allowing them to function as a one-way valve. For the extradural system, it is mainly the vertebral venous plexus (VVP) that collect blood from the radiculomedullary veins. There are internal and external VVPs. The internal VVPs (ventral and dorsal) locate extradurally within the vertebral canal, while the external VVPS (also ventral and dorsal) surrounds the vertebral column. After the radicular veins drain into the vertebral venous plexus, drainage occurs via the vertebral, deep cervical, and jugular veins which eventually lead to the superior vena cana (a large vein carrying deoxygenated blood from the upper body into the heart) in the cervical spinal cord region. A fundamental feature that distinguishes the vertebral venous system from the systemic venous system is the lack of valve allowing for bidirectional and retrograde flow (Groen et al., 1997; Tobinick and Vega, 2006). Thus, the venous system functions as a reservoir and equilibrates blood flow to and from the brain and other venous systems due to the change in posture and pressures. However, the “reflux-regulating” mechanisms of radicular veins provide a partial barrier to retrograde flow from the vertebral venous plexus back to the intrinsic and extrinsic systems.

A summary of the blood circulation in the spinal cord is as followed: The left ventricle of the heart pumps out the oxygenated blood through ascending aorta into the subclavian arteries. The blood passes into the segmental spinal branches through the vertebral arteries (VAs). The segmental spinal branches further divide into VSA and DSAs, which anastomose with each other forming a radial arterial network. This network supplies blood to the spinal cord at the capillary level in two different circuits: the centrifugal direction in the central section and centripetal direction in the peripheral section. After the oxygen in the blood is used and metabolized to carbon dioxide, the intrinsic venous system drains blood from the capillary network into the extrinsic system. After the radicular veins drain into the vertebral venous plexus in the extradural system, drainage occurs via the vertebral, deep cervical, and jugular veins which lead to the superior vena cana, eventually the right atrium of the heart. The low-oxygen blood passes to the right ventricle, and it is pumped into the pulmonary circulation, where the blood is replenished with oxygen and removal of carbon dioxide. Oxygenated blood then returns to the left atrium and passes into the left ventricle, waiting for the next circulation cycle.

Blood-CNS barrier

Blood-CNS barrier (BCB) is a term used to describe the unique properties of the microvasculature existing at all levels of the CNS, including the blood-brain barrier (BBB) and blood-spinal cord barrier (BSCB). Unlike the peripheral system, blood vessels in the CNS are continuous nonfenestrated vessels made of endothelial cells (EC), with a complete basement membrane (BM) and lacking fenestra (pores) in their plasma membrane. These structural features provide tight restriction of exchange between the blood and CNS, which maintains proper neuronal function, as well as protection from outside insults, including toxins, pathogens, inflammation, injury and disease (Daneman, 2012, Zlokovic, 2008).

The cellular components of BCB are ECs and mural cells. The barrier also highly interacts with astrocytes, neurons, and immune cells to manifest its functions.

Endothelial cells (EC)

ECs are simple squamous cells derived from the mesoderm that form a single cell layer lining the walls of blood vessels. Unlike ECs in peripheral tissues, CNS ECs possess two unique physical barrier properties, including tight paracellular flux regulated by tight junctions (TJ) and extremely low rates of transcytosis (Brightman and Reese, 1969, Reese and Karnovsky, 1967, Westergaard and Brightman, 1973, Coomber and Stewart, 1985). Transcytosis transports various macromolecules across the interior of a cell in the form of receptor-mediated vesicles. The extremely low rates of this transcellular movement of solutes indicate a much tighter barrier restriction compared to the peripheral tissue. In addition, ECs also present a few molecular barrier properties: efflux transporters (Loscher and Potschka, 2005), highly specific nutrient transporters (Mittapalli et al., 2010), high number of mitochondria for ATP generation supporting ion transportation (Oldendorf et al., 1977), and low level of leukocyte adhesion molecules (LAM) (Aird, 2007, Sohet and Daneman, 2013). Altogether, these features empower ECs to regulate the homeostasis tightly in the CNS.

Pericytes

There are two types of mural cells involved: vascular smooth muscle cells (SMC) and pericytes. Vascular SMCs typically encircle the large vessels such as arteries, whereas the pericytes provide high coverage on the endothelial cell layer of all vascular capillaries and post-capillary venules (Shepro and Morel, 1993). Pericytes sit on the abluminal surface of the microvascular endothelial tube, and are embedded in the vascular BM (Sims, 1986). The contractile proteins expressed in pericytes allow their regulation of the capillary diameter (Peppiatt et al., 2006, Hall et al., 2014). Previous studies have identified regulatory roles of pericytes in the following aspects: angiogenesis; deposition of extracellular matrix proteins; wound healing; immune cell infiltration; blood flow in response to the neural activity (Armulik et al., 2011). The pericytes are also reported as the multipotent stem cells of the CNS (Armulik et al., 2011). One major challenge to study these pericytes is lacking specific markers. Currently, a combination of PDGFR-beta and NG2 is widely accepted in the field to identify pericytes (Armulik et al., 2011). Uncovering of a more specific marker could unveil the answer to whether different subsets of pericytes possess different functions.

Basement Membrane

The basement membrane (BM) is comprised of type IV collagens, laminin, nidogen, heparin sulfate proteoglycans, and other glycoproteins (Sorokin, 2010). There are two layers of BM: the inner layer that mainly consists of laminin α4 and α5, secreted by neighboring ECs and pericytes; the outer parenchymal layer that comprises of laminin α1 and α2, produced by astrocytic processes extending onto the vasculature (Sorokin, 2010, Del Zoppo et al., 2006). Functionally, BM provides an anchor for signaling processes at the level of the vasculature; it also serves as another barrier to cells and molecules before entering the neural tissue. Matrix matalloproteinases (MMPs) often disrupt the BM that leads to BBB dysfunction and leukocyte infiltration in different neurological disorders (Daneman and Prat, 2015).

Astrocytes

Astrocytes extend their polarized processes to encircle either neuronal processes or blood vessels (Abbott et al., 2006). Astrocytes provide a cellular link between the neuronal circuitry and blood vessels, called neurovascular coupling. This neurovascular coupling allows astrocytes to relay signals that regulate blood flow in response to neuronal activity (Gordon et al., 2011, Attwell et al., 2010). Astrocytes take part in regulating the contraction/dilation of the blood vessels via vascular smooth muscle cells or pericytes depending on the vessel types. Rodent embryo studies suggest that astrocytes do not play a role in the initial induction phase of the BBB (Daneman et al., 2010). However, astrocytes modulate and maintain the BBB once formed. Previous studies have shown that purified astrocytes were able to induce barrier properties in non-CNS blood vessels during in vivo transplantation (Janzer and Raff, 1987). In addition, astrocytes could again induce barrier properties in ECs of a co-culture system in vitro (Abbott et al., 2006). At the molecular level, the endfeet of astrocytes contain a discrete array of proteins, including dystrophin, dystroglycan, and aquaporin-4 (AQP-4). The dystrophin-dystroglycan complex helps the endfeet cytoskeleton linking to the BM by binding agrin (Noell et al., 2011, Wolburg et al., 2011). This linkage coordinates AQP-4 into orthogonal arrays of particles, which is critical for regulating water homeostasis.

Immune Cells

Perivascular macrophages and resident microglia are two types of immune cells involved in the surveillance at the blood-CNS barrier. Perivascular macrophages are blood-borne monocyte lineage cells, which are able to cross the BBB and be 80% replenished every three months (Unger et al., 1993, Vass et al., 1993, Williams et al., 2001). The macrophages reside on the abluminal surface of the blood vessels facing toward the CNS parenchymal tissue, named the “Virchow-Robin” space (Polfliet et al., 2001, Hickey and Kimura, 1988). They are at the first line of immune defense system by phagocytosing cellular debris. Microglia are resident CNS immune cells in the parenchyma, which derived from the progenitor cells in the yolk sac and entered the brain during embryonic development (Ginhoux et al., 2010). Microglia regulate neuronal development, innate immune response, wound healing, and they can act as antigen-presenting cells in adaptive immunity (Streit et al., 2005, Ajami et al., 2007). Additionally, there are also other blood-borne immune cell populations, such as neutrophils, T cells, and macrophages. During cases of injury, infection or disease, these cells become activated and alter the BBB properties by releasing ROS to increase vascular permeability (Hudson et al., 2005, Persidsky et al., 1999). It still requires further studies to identify the mechanism of both BBB and immune cells becoming "activated" under different neurological conditions.

BCB Functional Properties

These unique barrier properties alow BBB to serve several important functions. First its tight restriction protects the CNS from 'foreign substances' which may insult the brain and spinal cord. Secondly, BBB compartmentalizes the CNS from peripheral tissue so that the CNS would not receive the 'crosstalk' effects of neurotransmitters and hormones that target the peripheral system; so similar agents can be applied to two systems for different purposes (Abbott et al., 2006). Thirdly, BBB tightly regulates the homeostasis of the microenvironment by restricting ion transportation and maintains the fluid balance between the blood and the CNS via different ion transporters and channels for proper neuronal functions. Additionally, the restriction avoids interference with synaptic transmission caused by fluctuations in ionic compositions that can occur after a meal or exercise.

Differences between BBB and BSCB

Previous studies reported elevated permeability in BSCB compared to BBB, suggesting there may be a region-specific difference (Prockop et al., 1995, Pan et al., 1997, Daniel et al., 1981). Although there are slight variances between the two structures, BSCB is often considered as the extension of the barrier from the brain to the spinal cord and shares similar structures and functions with BBB.

Besides a blunt trauma like SCI, disruption of the BSCB is also observed in many different spinal cord diseases, including spinal cord ischemia (Jacobs et al., 1992), multiple sclerosis (MS) (Schellenberg et al., 2007), posttraumatic syringomyelia (Hemley et al., 2009), amyotrphoic lateral sclerosis (ALS) (Garbuzova-Davis et al., 2007), radiation injury(Li et al., 2004), and neuropathic pain (Bartanusz et al., 2011, Beggs et al., 2010). In general, BSCB dysfunction can lead to ion dysregulation, altered signaling homeostasis, as well as the infiltration of immune cells and molecules into the CNS, processes that lead to neuronal dysfunction and degeneration (Bartanusz et al., 2011).

Subsequent vascular and inflammatory responses to SCI

The primary physical insult inflicted on the spinal cord leads to a subsequent temporospatial profile of secondary damages, which usually lasts for months and years since the initiation of the trauma. It is widely accepted that vascular disruption is one of the early consequences and hallmark of acute SCI (Benton et al., 2009b). During the first hour of injury, scientists have found signs of vascular disruption in the injury epicenter (Dohrmann and Allen, 1975). The initial vascular damage often results in hemorrhage, which is mainly located in the gray matter (Tator and Koyanagi, 1997). The blood undergoes hemolysis and the lysed product of red blood cells infiltrates into the perivascular space, which is rather toxic to the parenchyma and eventually leads to neuronal and axonal damage (Asano, 1980). The infiltration of neutrophils releases proteolytic enzymes, which also causes injury to local cells. At 24 hour post-injury, there is evidence of vasospasm (Anthes et al., 1996), hypo-vascularity (Benton et al., 2008, Loy et al., 2002), decreased blood flow in the injury epicenter (Rivlin and Tator, 1978). Reduction of blood flow leads to ischemic damage to the spinal cord, primarily in the white matter (Tator and Koyanagi, 1997). These pathological vascular changes trigger a multi-factorial event which is facilitated by inflammatory cytokines and chemokines, eventually lead to cell death and tissue destruction via various mechanisms, including glutamate excitotoxicity, oxidative stress, oxygen deprivation, and necrosis (Alizadeh et al., 2019).

In addition, vascular injury plays a key role in initiating secondary inflammatory responses via activation of CNS innate immune cells (microglia and astrocytes) and infiltrating leukocytes (neutrophils, monocyte, macrophages, and lymphocytes) (Mautes et al., 2000, Anwar et al., 2016). The initial vascular disruption leads to immediate response from endothelial cells (Benton et al., 2009b), loss of astrocytic investment (Whetstone et al., 2003), regression of pericytes (Benton et al., 2008), perivascular localization of infiltrating inflammatory cells (Popovich and Jones, 2003), activation of microglia (Li et al., 2013), astrocytes (Hawkins and Davis, 2005), subsequent loss of oligodendrocytes (Crowe et al., 1997, Liu et al., 1997), neurons and axons (Daneman et al., 2010). Specifically, microglia become activated after detecting cues of cellular or tissue damage in the CNS, including a pathway via extravasation of serum protein fibrinogen (Davalos et al., 2012). Upon activation, microglia undergoes hypertrophic morphological and functional transformation into two polarized states: the M1 (classically activated) pro-inflammatory phenotype and M2 (alternatively activated) anti-inflammatory phenotype (Witcher et al., 2015, Durafourt et al., 2012). The activated M1 phenotype initiates the inflammatory cascades which go through multiple pathophysiological signaling pathways, including cytokines (TNF-α, IL-1β, IL-6) (Rothwell et al., 1997, Pan et al., 2002, Pineau and Lacroix, 2007), chemokines (Mantovani et al., 2004), nitric oxide (Merrill et al., 1993, Matsui et al., 2010), reactive oxygen species (ROS) (Barger et al., 2007), glutamate (Barger et al., 2007), and proteases (Shields et al., 2000). The M2 phenotype releases anti-inflammatory cytokines (IL-4, IL-10, IL-13) (Witcher et al., 2015, Durafourt et al., 2012). Taken together, these two distinct microglia phenotypes and many intermediate states of cells participate in the regulation of the inflammatory response and reorganization of the homeostatic microenvironment. Astrocytes and macrophages also undergo polarization of pro- and anti-inflammatory states, which is similar to microglia (Cherry et al., 2014). Additionally, activation of microglia and macrophages leads to not only clearance of cellular and molecular debris, but also loss of oligodendrocytes, axon demyelination, and neuronal apoptosis (Merrill et al., 1993, Shuman et al., 1997, McTigue and Tripathi, 2008). This secondary wave of pathological damages has been considered to be a primary cause leading to functional deficits after SCI (Casella et al., 2002, Loy et al., 2002).

Current limitation/challenge to study vascular injury

There has been interest in studying vascular injuries following SCI for decades. However, one major challenge is the technical limitations. Traditional techniques are largely restricted to the investigation of vascular structural changes in post-mortem samples (Figley et al., 2014, Loy et al., 2002). For example, vascular corrosion casts were frequently used to obtain the structural information of the vasculature in various animal models (Koyanagi et al., 1993a, Mazensky et al., 2015, Naka et al., 1987). In brief, a three-dimensional mold of the blood vessel network was acquired by filling the perfused vasculature with polyester resin and dissolving surrounding tissues, followed by inspection of scanning electron microscopy (SEM). Although this technique showcased vascular organization, it cannot provide dynamic vascular changes at pre- and post-injury. In addition, this technique often encounters problems of insufficient perfusion in traumatic tissues, therefore, it cannot differentiate different types of morphological changes in blood vessels, such as loss of vasculature, occlusion, and rupture. Other techniques, including hydrogen clearance (Kobrine et al., 1974), autoradiography (Rivlin and Tator, 1978), and silicone rubber microangiography (Tator and Koyanagi, 1997), have also encountered difficulties in observing dynamic vascular changes. In addition, all techniques mentioned above require extensive time for processing the post-mortem samples, which in turn increases the difficulty of experimental operations.

Although laser doppler flowmetry (LDF) provides real-time measurement of gross regional blood flow *in vivo*, the major disadvantage of this method is the high variable results, affected by artifacts such as the probe placement and environmental factors (Tei et al., 2005). Besides a gross readout of the blood flow, this technique cannot provide information on morphological and physiological changes in spinal cord vasculature. A reliable and accurate method is still in urgent need to study vascular injury following SCI on living animals.

Current knowledge on the expansion of secondary injury

After the initial mechanical impact, the following secondary injury is held accountable to the continuing enlargement of lesion size from the initial injury for a long time after SCI (Liu and Xu, 2012). Previous studies indicate the lesion starts from the injury epicenter and expands rostrocaudally over time leading to the death of initially viable axons and cells resulting in deleterious functional loss, which became the most acceptable view of a "spindle-like" pattern in secondary injury progression (Tator and Fehlings, 1991, Onifer et al., 2007a). This "spindle-like" pattern considers the initial responses of all cellular components, including vasculature and neurons, are restricted within the mechanical impact site. However, the role and underlying mechanisms of early vascular disruption in progressive degeneration after SCI remain elusive.

The knowledge gaps

Several key questions remain to elucidate the vascular mechanisms contributing to SCI. First, to my knowledge there was no study available on *in vivo* vascular changes after acute SCI. Second, it is unknown whether SCI triggers immediate vascular responses in areas beyond the initial injury. Third, it is also unidentified whether the vascular injury precedes or is simultaneous with other cellular responses in the adjacent areas next to the initial injury. The last question I asked is whether a therapeutic strategy targeting acute vascular leakage could lead to histological and functional recoveries.

To address the first question, I developed a "duo-color" method using two-photon laser scanning microscopy (TPLSM) *in vivo* to visualize spinal cord vasculature. A sequential injection of two different colored tracers allows me to monitor changes in the same vessels before and after SCI. A single-color tracer will leak outside the blood vessel after the trauma to indicate the range of extravasation, but it can no longer trace the pattern of blood vessels. The following second color tracer can capture the post-trauma blood vessels within a period of time after injection. This imaging tool allows me to assess changes in both vessel diameter and permeability. Thus, I have successfully monitored various vascular changes *in vivo* in an SCI model for the first time, allowing me to identify potential vascular targets following SCI.

To address the second and third questions, I designed experiments to determine region-specific vascular changes at the injury epicenter (C7), the adjacent (C6) and the remote (C5) cord regions, using my *in vivo* duo-color approach and histological analyses. My results showed that vascular injury, including vasodilation and increased vascular permeability, occurred in areas beyond the initial injury site, and in a “transitional zone” vascular injury precedes other cellular changes. In conclusion, I found a time window between vascular injury and other secondary degeneration in the transitional zone.

To address the last question, I designed a three-part experiment to examine the effect of a nanoparticle, FA-GC, on targeting vascular leakage following injury. My results showed that FA-GC effectively reduced vascular leakage, resulted in acute neuroprotection and partial functional recovery. Thus, I believe that targeting vascular leakage is a potential therapeutic strategy, as well as a proof of concept that initial vascular damages are involved in subsequent secondary injuries.

In summary, this thesis highlighted a new role of early vascular injury on progressive secondary degeneration following SCI and tested a new therapeutic strategy for targeting microvasculature repair to achieve acute neuroprotection and functional recovery.

CHAPTER 2

DEVELOPING A NOVEL IN VIVO IMAGING METHOD TO MONITOR DYNAMIC VASCULAR DAMAGES FOLLOWING ACUTE SPINAL CORD INJURY

Hypothesis

A newly established *in vivo* imaging technique enables me to detect a temporospatial profile of dynamic spinal vascular changes, including blood vessel diameter and vascular permeability, in a contusive spinal cord injury rat model.

Introduction

In order of precedence, SCI is categorized into primary and secondary injury phases. The primary injury phase often refers to the direct mechanical impact which leads to hemorrhage and necrosis at the site of injury within minutes after SCI (Dumont et al., 2001). In the following hours and days, the range of damaged tissue is expanded due to a cascade of secondary injuries, including inflammation, cell apoptosis, and demyelination of remaining axons (Beattie et al., 2000, Liu et al., 2006, Wu and Xu, 2016, Li et al., 2016). Vascular disruption occurs immediately after SCI, indicated by the evident sign of hemorrhage (Kulkarni et al., 1987, Tator and Koyanagi, 1997). It is of great potential to target these acute vascular damages for neuroprotection, but a better knowledge of spinal vascular pathophysiology following SCI is vital.

Quite a number of techniques have been applied on spinal vascular studies since 1970s, such as hydrogen clearance (Kobrine et al., 1974), autoradiography (Rivlin and Tator, 1978), microangiogram (Tator and Koyanagi, 1997), vascular corrosion casts

(Koyanagi et al., 1993b), electron microscopy (Anthes et al., 1996), and immunohistochemistry (Noble and Wrathall, 1989a, Maikos and Shreiber, 2007). These methods indeed broaden my insights on the anatomy of the spinal vascular system, but their applications restricted to postmortem samples reveal a few limitations. All above-mentioned procedures are time-consuming, and the vascular structures receive various degrees of distortion depending on specific chemical steps during the processes. Most importantly, none of them can capture the morphological changes in these injured vessels accurately due to the technical limitations. For example, vascular corrosion casts often cannot generate the exact vascular structures due to either insufficient perfusion of the micro-vessels or excessive aggregation of the resin leaking outside the ruptured vessels. Altogether, these techniques are unable to monitor dynamic vascular changes following SCI.

There are some available imaging options providing real-time monitoring on living animals. Laser Doppler Flowmetry (LDF) provides a continuous measurement of microvascular blood perfusion in the spinal cord (Tei et al., 2005). Although LDF presents a great advantage with the noninvasive nature, its high sensitivity to all types of movements results in poor data reproducibility (Fagrell and Nilsson, 1995). In addition, LDF cannot provide information in vascular morphology. Another noninvasive method is Dynamic Contrast-enhanced MRI (DCE-MRI), but the required infrastructure is costly and DCE-MRI-related agents often present low sensitivity to vascular changes (Cohen et al., 2009, Yan et al., 2017). In order to study the vascular pathophysiology, a technique that can simultaneously provide in vivo changes and high-resolution images is highly required.

The in vivo imaging using 2-photon laser scanning microscopy (2P-LSM) is a great option for spinal vascular imaging given that it has been used for vascular dynamic studies in the cortex (Drew et al., 2011, Schaffer et al., 2006, Kim et al., 2012). In a spinal cord hemisection model, Tang et al. detected blood flow fluctuation at the periphery of the lesion site (Tang et al., 2015). However, it is not amenable to spinal vascular imaging because it requires technical optimization to adapt imaging at traumatic tissue areas. There are three main challenges. First, the installation of the imaging window allows repetitive imaging at the lesion epicenter pre- and post-injury. Second, SCI has technical limitations that make post-injury imaging difficult. Last, the stabilization of the spinal cord during imaging is critical for stable imaging but often affected by breathing and pulsation.

To overcome these difficulties, I first successfully established a novel *in vivo* method to visualize vascular dynamics. By sequentially injecting two different fluorescein-conjugated dextran tracers intravenously, this tool can provide a temporospatial profile in dynamic vascular changes, such as blood vessel diameter and permeability, before and after a contusive SCI model.

Step-by-step procedure

1. Animals and Surgical Preparation

Adult female Sprague-Dawley (SD) rats (180-220 gram, Harlan) were housed in controlled conditions with a 12:12 light: dark cycle, and free access to food and water *ad libitum*. To prepare for surgery, the rats were anesthetized with an intraperitoneal injection of ketamine (87.7mg/kg)/xylazine (12.3mg/kg) and confirmed with no response from a toe pinch stimulus. For the purpose of animal welfare, the animals also received a subcutaneous injection of Buprenorphine (0.01-0.05mg/kg) and Carprofen (5mg/kg) for analgesic and anti-inflammatory effects. Prior to surgery, both the cervical spine area (back side) and neck (breast side) were shaved, and the skin areas were swabbed with betadine and 70% alcohol. It is critical to maintain the body temperature of the rats by placing them on the heating pad. All surgical and animal handling procedures were performed as approved under the Guide for the Care and Use of Laboratory Animals (National Research Council) and the Guidelines of the Indiana University School of Medicine Institutional Animal Care and Use Committee.

2. External Jugular Vein Catheterization

On the breast side of the rat, a vertical incision was made on the skin near the right side of the clavicle to expose the external jugular vein, which is at the superficial layer of the neck amenable to visual identification. The landmark of the vein was the pulse point in the triangular area connected by three anatomical points: caudal ramus of the right mandible, greater tubercle of humerus and manubrium (**Fig. 2.1A**). After separating from adjacent muscles and connective tissues, the external jugular vein was first tied at the distal end to the heart (**Fig. 2.1C**) (Thrivikraman et al., 2002). At the proximal end, the vessel was incised with a small opening and inserted a specialized catheter (**Fig. 2.1B**) connected to a saline-filled syringe. The extra needle piece welded onto the specialized catheter was to secure the catheter placement from slipping out of the vein. The proper function of the catheter was confirmed by blood aspiration and successful subsequent flushing with saline. The catheter should then be sutured at the proximal end (**Fig. 2.1C**).

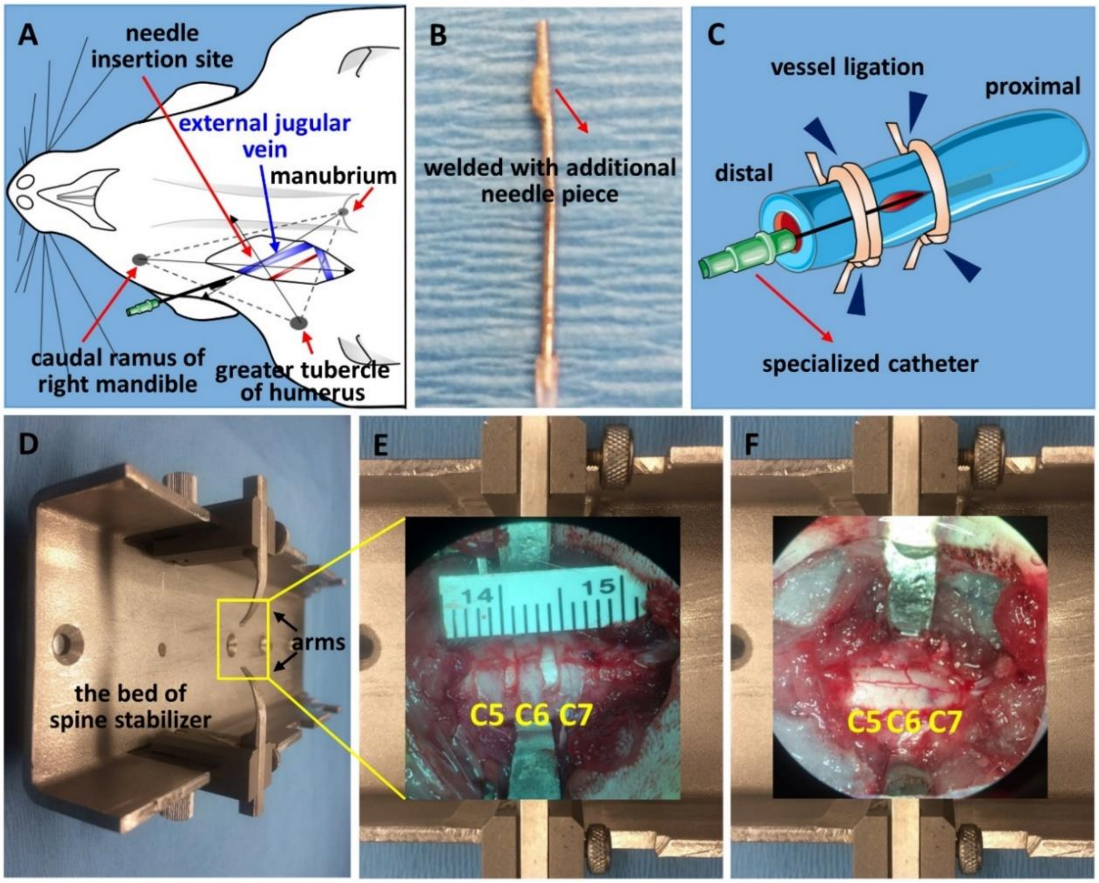

Figure 2.1. Jugular vein catheterization and spine stabilization.
(A) A schematic drawing for locating the external jugular vein. **(B**) The specialized catheter made from a 21-gauge needle. The tip was ground flat and welded with a piece of 2 millimeter tip cut off from another 21-gauge needle. **(C)** A schematic diagram of catheterization. The distal end is ligated first, followed by proximal catheter stabilization, ending with fastening the needle along with the vessel (vessel ligation, blue arrowheads). **(D)** An image of the modified spine stabilizer. A C5-C7 window prior to laminectomy **(E)** and after laminectomy and contusive SCI **(F)** is displayed.

3. Spine Stabilization and C5-C7 Laminectomy

This step is adapted from previous protocols (Walker et al., 2015, Anderson et al., 2009, Krishna et al., 2013, Lepore, 2011). In brief, a pair of customized spine stabilizers were utilized to fix the 5th to 7th cervical vertebrae and a C5-C7 laminectomy exposed the cord area with intact dura mater. Prior to the next step, a small piece of saline-soaked gelfoam was placed on top of the exposed cord to maintain moisture (**Fig. 2.2**).

4. Installation of Two-photon (2P) Imaging Window

To maximize the prevention of bleeding, small pieces of gelfoam were carefully placed into the gaps among spinal cord, muscles and vertebral bones, followed by sealing with tissue adhesive glue. After completely dry, 4% agar solution (dissolved in saline, preheated and cool down to room temperature) was added around the rim of the window to build a wall which quickly solidified (**Fig. 2.2E**). Then the imaging window is ready for the next step.

5. Baseline Imaging

The first fluorescent agent was prepared in saline with Rhodamine B isothiocyanate-Dextran (Rho-Dextran, 4 mg/ml, ~70 kDa in average molecular weight, $\lambda_{max.}$ ~543 nm). A dosage of 0.5 ml was filled in a 1 ml sterile syringe and connected to the installed catheter. The animals were then transferred to a two-photon laser-scanning microscope (TPLSM, Prairie Technologies, Middleton, WI). The area of exposed C5-C7 spinal cord segments was focused under bright-field. For baseline imaging, a bright-field image of the superficial spinal blood vessels was first captured at 4x magnification (NA 0.1; Olympus, Shinjuku, Tokyo, Japan). This image served as a map of landmarks to track individual blood vessels. The Rho-Dextran was then slowly administered through the external jugular vein catheter.

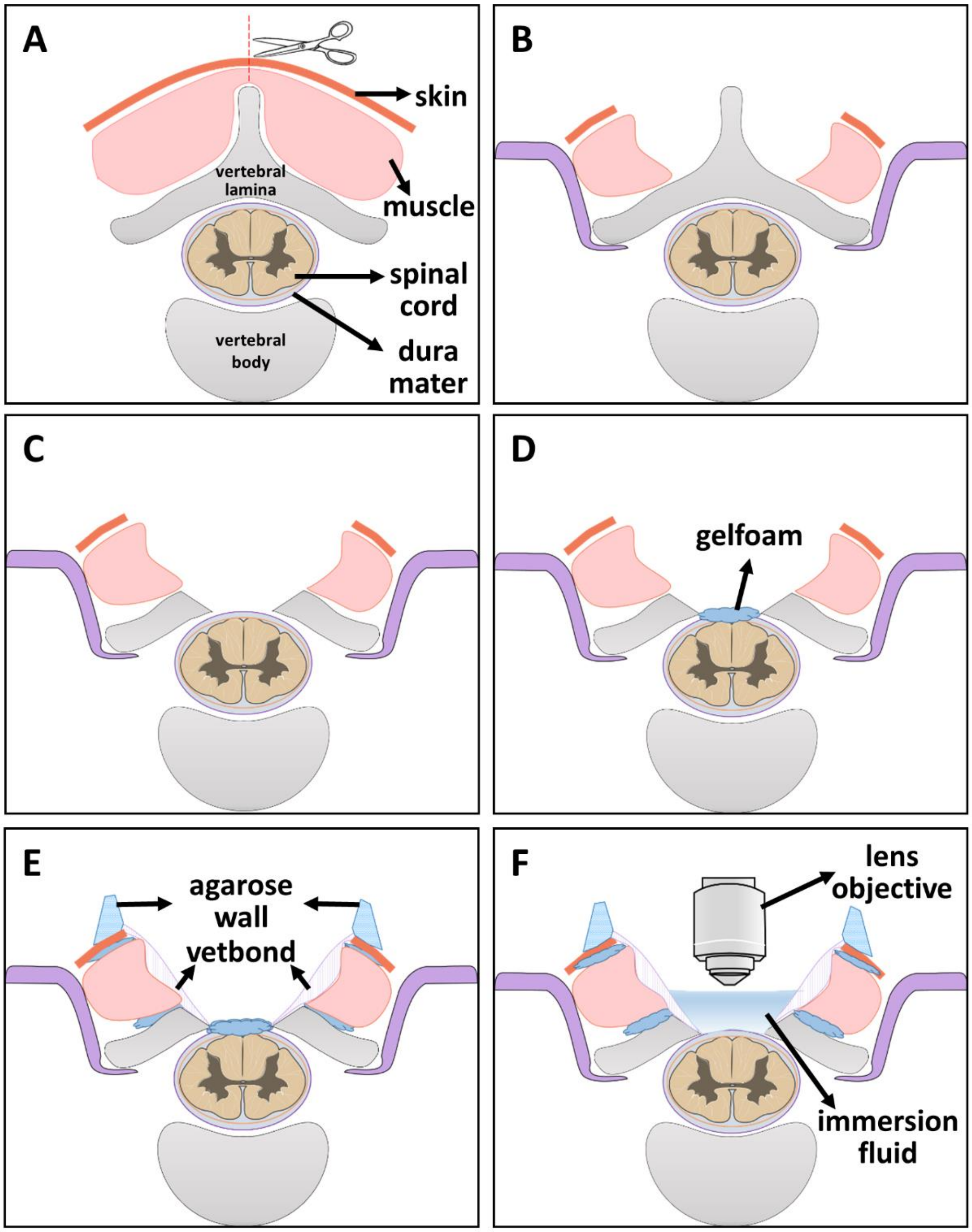

Figure 2.2. Schematic diagram of optic window installation step-by-step.
(A) Step 1: expose the vertebra by cutting skin and muscle along the midline. **(B**) Step 2: spine stabilization. **(C)** Step 3: laminectomy. **(D)** Step 4: maintain the moisture of the spinal cord by placing a piece of saline-soaked gelfoam. **(E)** Step 5: seal the gaps with sterile gelfoam and vetbond. After drying, a layer of agar wall is built on the edge of the window. **(F)** Step 6: when ready for imaging, remove the gelfoam and place immersion fluid inside 2P imaging window.

After switching to laser scanning mode, the proper 2P laser excitation wavelength, power and red fluorescent channel were selected (**Fig. 2.3E**). A series of Z-stack images with the thickness of 200-400 μm were obtained across C5-C7 dorsal spinal tissue at 10x magnification (NA 0.30; Olympus). In addition, the line-scan images were generated by fast scanning along a defined path on individual blood vessels. Within the view of each spinal cord segments, 5-10 blood vessels were captured. Each imaging session usually takes 30 to 45 minutes to complete starting from the injection of the tracer. The animals were placed on a heating pad during the whole process.

6. Contusive Spinal Cord Injury at C7

Spinal cord injury was performed using a Louisville Injury System Apparatus (LISA) device based on a previously established protocol (Zhang et al., 2008, Wu et al., 2017). LISA was calibrated every time prior to performing injury. Briefly, the animals received a midline contusive SCI at the 7th cervical spinal cord segment with an adjusted tissue displacement of 0.800mm. After the injury, the exposed dura mater was left with another piece of saline-soaked gelfoam on top to stay moisturized. The animal was placed back on a heating pad and appropriate anesthesia was given when necessary.

7. Post-injury Imaging

This step is similar to the previous baseline imaging step except that a second fluorescent dye, Fluorescein isothiocyanate-Dextran (FlTC-Dextran, 4 mg/ml, 0.5 ml, ~70 kDa in average molecular weight, $\lambda_{max.}$ ~492 nm), was slowly injected before post-injury imaging. After locating the same vessels, both red and green fluorescent channels were selected to capture both blood extravasation and post-injury blood vessels labeled by Rho-Dextran and FITC-dextran (**Fig. 2.3D, G**). Another series of Z-stack images were obtained, and line-

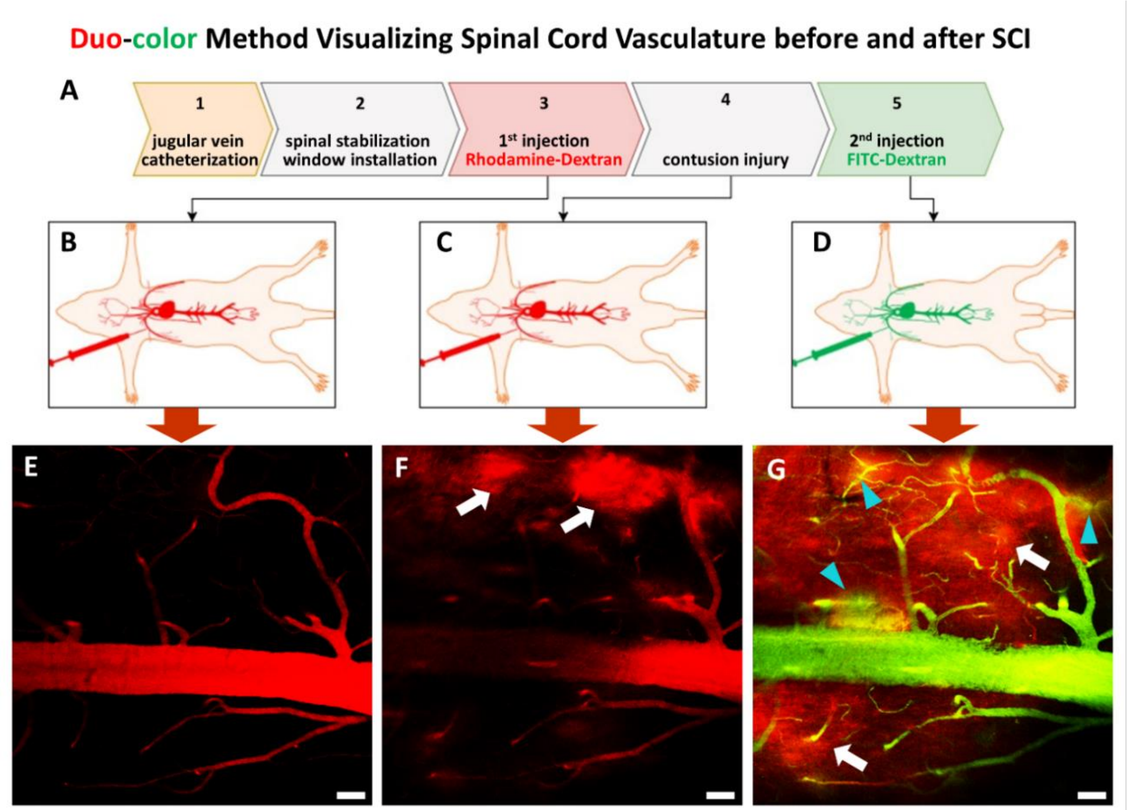

Figure 2.3. The in vivo duo-color method procedure step-by-step.

The whole procedure consists of 5 steps **(A)**. Following Step 1 and Step 2, a pair of dextran tracers with a size of approximate 70 KDa are injected in sequence to label the spinal cord vasculature before **(B** and **C**) and after contusive SCI **(D)**. **(E)-(G)** representative 2P images display the spinal cord vasculature at Step 3 through Step 5. White arrows point to first-wave red dye leaking areas (**F** and **G**), turquoise arrowheads display second-wave green dye leakage **(G)**. Scale bar = 50 µm.

scan images were generated by fast scanning along a defined path on individual blood vessels.

Data analysis and representative results

The measured parameters are vessel diameter, vascular permeability, and RBC velocity. The first two parameters were analyzed via ImageJ. The single image files were first calibrated true to scale (**Fig. 2.4A-C**). For vessel diameter, a line is drawn perpendicular to the long axis of the vessel segment to measure the diameter. Repeat 3 times across the vessel to acquire the average value (**Fig. 2.4D_{1-2} & E_{1-2}**). An example is presented here that the diameter of the vessel has been increased significantly in response to the injury at 30 minutes after SCI (**Fig. 2.4F**). For vascular permeability, a 200 µm line is drawn inside and outside the vessel to measure the fluorescence integrated density. The vascular permeability is calculated as the ratio of the outside value divided by the inside value (**Fig. 2.5**). A higher ratio means increased vascular permeability. The RBC velocity was quantified based on the line-scan images using MATLAB-based software adapted from a previously established protocol (Kim et al., 2012). In brief, each dark streak stands for the moving path of individual red blood cell (RBC) since the dextran dyes do not stain the RBCs. The speed is determined by the traveled distance of the RBC over time, shown as $\Delta x / \Delta t$ (**Fig. 2.6A**). The final RBC velocity along the scan line is determined from average peak values over time (**Fig. 2.6B-C**, middle dashed line). In addition, the observed vessels can be categorized into arteries and veins based on the following criteria: blood vessel morphology, blood flow velocity, and vessel diameter (**Table 2.1**). All required materials to complete this procedure are included in the following table (**Table 2.2)**.

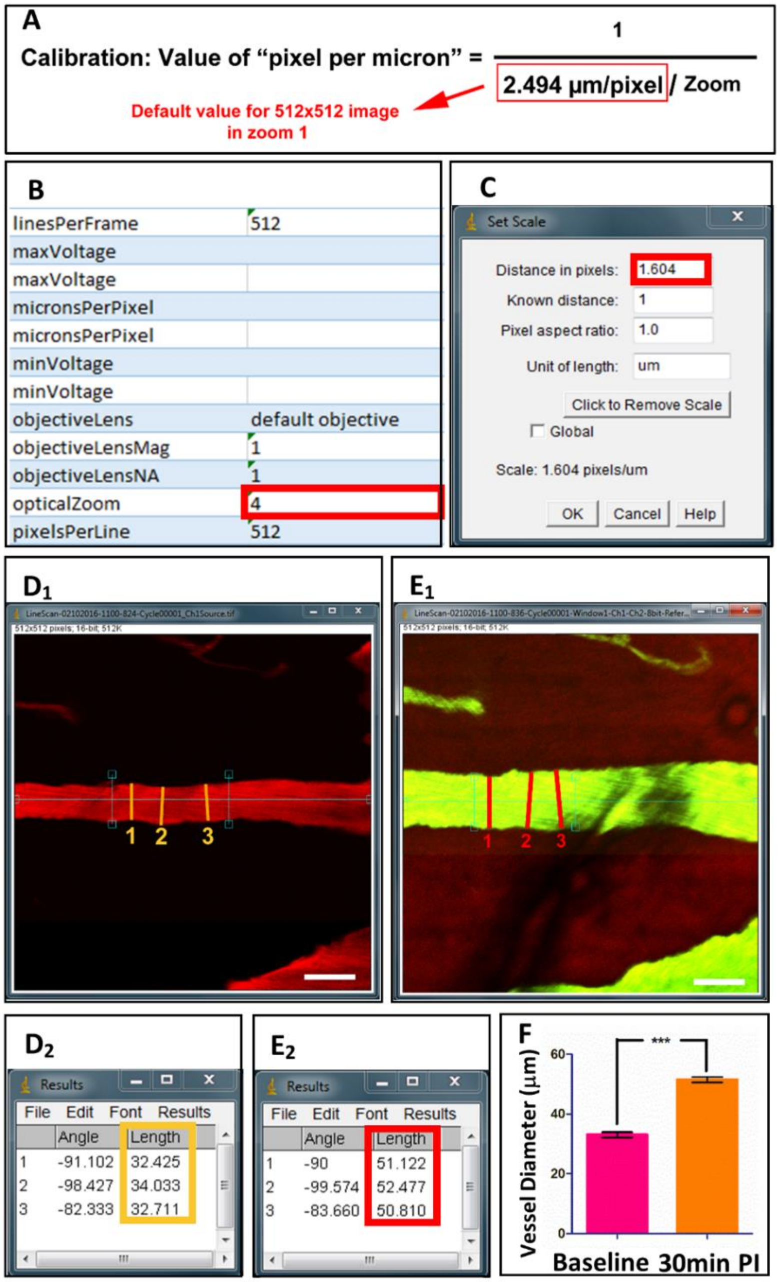

$$\text{Calibration: Value of "pixel per micron"} = \frac{1}{\boxed{2.494\ \mu m/pixel}\ /\ \text{Zoom}}$$

Default value for 512x512 image in zoom 1

linesPerFrame	512
maxVoltage	
maxVoltage	
micronsPerPixel	
micronsPerPixel	
minVoltage	
minVoltage	
objectiveLens	default objective
objectiveLensMag	1
objectiveLensNA	1
opticalZoom	4
pixelsPerLine	512

Distance in pixels: 1.604
Known distance: 1
Pixel aspect ratio: 1.0
Unit of length: um
☐ Global
Scale: 1.604 pixels/um

	Angle	Length
1	-91.102	32.425
2	-98.427	34.033
3	-82.333	32.711

	Angle	Length
1	-90	51.122
2	-99.574	52.477
3	-83.660	50.810

Figure 2.4. Acquisition and quantification of spinal vessel diameters.
Following preparation, single image files are acquired under 2P microscopy, along with XML files of calibrated values **(B)**. **(A)** The equation displays the calculation of "pixel per micron" based on optical zoom values. After calibration in ImageJ **(C)**, vessel diameters are measured at 3 points across the longitudinal axis before **(D1)** and after **(E1)** injury. **(D2)** and **(E2)** display the measured values. **(F)** Quantification of vessel diameters at baseline and 30 min post-injury. Scale bar = 50 μm. Data are shown as mean ± SD, ***p<0.0001, two-tailed paired t test.

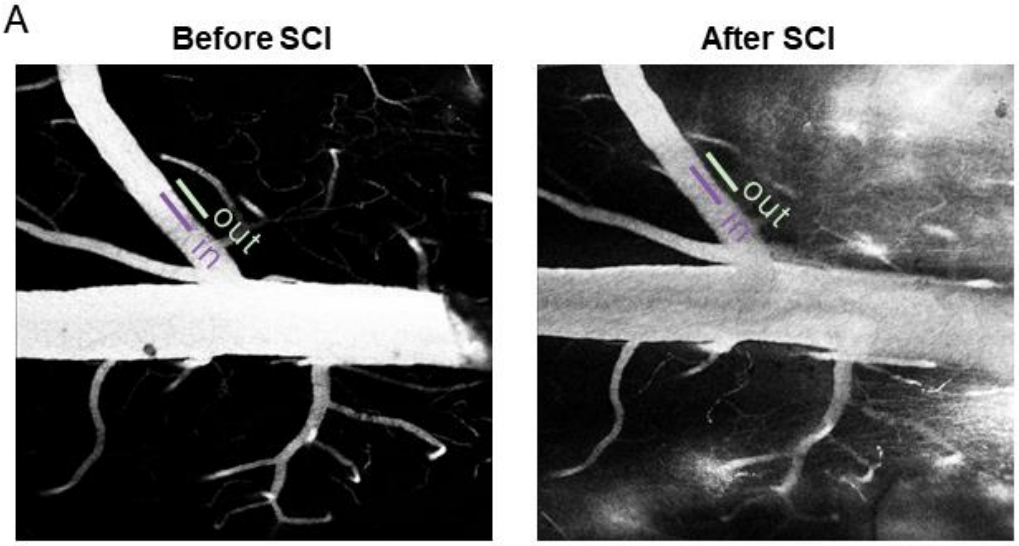

B

$$\text{Vascular leakage} = \frac{V_{out}\ \text{intensity}}{V_{in}\ \text{intensity}}$$

Figure 2.5. Measurement of vascular permeability.
(A) Before and after SCI, a probe of is drawn both inside and outside the vessel to measure the fluorescence integrated density of the first Rho-dextran dye. **(B)** The vascular permeability is calculated as the ratio of the outside value divided by the inside value.

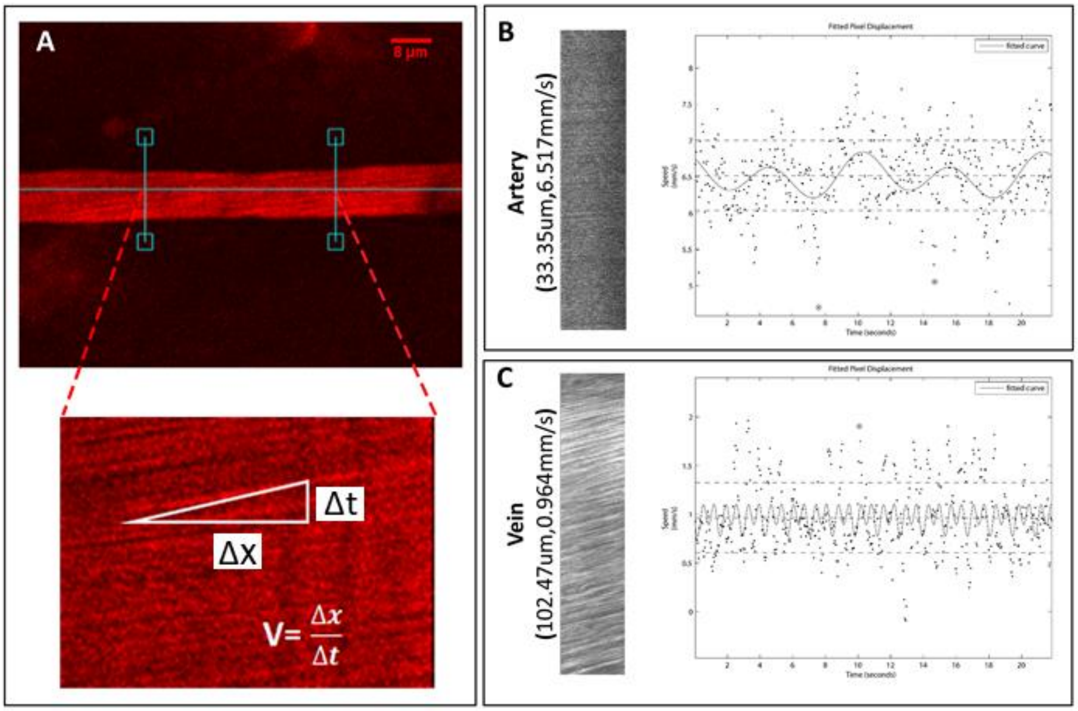

Figure 2.6. Acquisition and quantification of spinal vessel velocity.

Line-scan image files are acquired under 2P microscopy to calculate single vessel velocities. **(A)** An example of a selected vessel and method to assess blood vessel RBC velocity. **(B)** An arterial example of a line-scan image and corresponding plot file for calculation of velocity, as well as an example of a vein **(C)**. Y-axis indicates speed and x-axis shows time.

Table 2.1. Criteria for identifying vessel types

	Artery	***Vein***
Morphology	Straight, smooth, thick vessel wall	Branches, rough edges
Blood Flow Velocity	Fast	Slow but varies
Diameter	30-80 μm	100-250 μm

Table 2.2. List of materials for *in vivo* duo-color method

Name of Material/ Equipment	**Company**	**Catalog Number**	**Comments/ Description**
Purdue Products Betadine Surgical Scrub	Fisher Scientific	19-027132	Skin sterilization
Ketamine (87.7 mg/kg)/Xylazine (12.3 mg/kg)	Patterson Veterinary	07-881-9413, 07-890-5745	Anesthetic agent
Buprenorphine(0.03 mg/mL)	Patterson Veterinary	07-891-9756	Pain relief agent
Carprofen	Patterson Veterinary	07-844-7425	Non-steroidal anti-inflammatory drug
Dukal Gauze Sponges	Fisher Scientific	22-415-490	Skin sterilization
Decon Ethanol 200 Proof	Fisher Scientific	04-355-450	Skin sterilization
Artificial Tears Eye Ointment	Webster Veterinary	07-870-5261	Prevent drying eyes
Cotton Tipped Applicators	Fisher Scientific	1006015	
Heparin sodium salt from porcine intestinal mucosa	Sigma-Aldrich	H3149	187 USP per ml, prevention of blot clotting
Rhodamine B isothiocyanate–Dextran	Sigma-Aldrich	R9379	Average mol wt 70kDa
Fluorescein isothiocyanate–dextran	Sigma-Aldrich	46945	Average mol wt 70kDa
Instrument Sterilizer	Fine Science Tools	18000-50	for sterilizing surgery tool
Spine stabilizer set	Custom Manufactured from Norton Neuroscience Institute		Contact Y. Ping Zhang for details. (yipingzhang50@gmail.com)
Vetbond	3M Animal Care Products	1469SB	Tissue adhesive Glue
Gelfoam	Henry Schein	9083300	Stop bleeding
Noyes Spring Scissors	F.S.T	15013-12	
Fine Forceps- Dumont #5	F.S.T	11254-20	
Rongeur	Fine Science Tools	16021-14	laminectomy
Surgical Retractor	Fine Science Tools	17005-04	

Scalpel	Fine Science Tools	10003-12	skin cut
Scalpel Blade #15	Royal-Tek	BS2982	skin cut
micro angled scissors	World Precision Instruments	500260	Can be from any vendor
3-0 vicryl sutures	Ethicon	J393H	Can be from any vendor
1ml syringe	Henke Sass Wolf	4010.200.V0	Can be from any vendor
21 gauge needle	BD	305165	Can be from any vendor
Agar	Sigma-Aldrich	A1296	Can be from any vendor
Two-photon Laser Scanning Microscope	Bruker Fluorescence Microscopy		
LISA device	Custom Manufactured from Norton Neuroscience Institute		Contact Y. Ping Zhang for details. (yipingzhang50@gmail.com)
Paraformaldehyde	Sigma-Aldrich	158127	
HCImage Live	Hamamatsu Corporation		Imaging software
PrairieView	Prairie Technologies/ Bruker		Two-photon imaging software
ImageJ			Image analysis software
Matlab statistics toolbox	The MathWorks, Inc.	https://www.mathworks.com/products/statistics.html?s_tid=srchtitle	Image analysis software

Discussion

Lacking a stable imaging model is one major challenge to monitor vascular changes following SCI successfully. Currently available measures limit their applications on postmortem samples, which only provide a snapshot of the vascular structural changes. Using 2P-LSM, my innovative duo-color imaging method allows continuous observation of vascular changes in living animals. In the same animal, several vascular parameters can be measured simultaneously, such as RBC velocity, vessel diameter, and vascular permeability. The design of this sequential two-dye injection is unique from other intravital imaging methods. At a specific post-injury timepoint, while the immediate delivered second dye remains in the vessel and captures vascular structures, the leakage of the previous tracer can indicate the change of vascular permeability in response to the injury. Additionally, this method is flexible to generate a temporospatial profile of vascular changes at the acute phase of SCI.

There are several key steps in this method that are worth noting. First, ensuring a complete stabilization of the spinal cord is essential to guarantee every successful time-lapse imaging. Due to the location of the spinal imaging window, motion artifacts occur due to breathing and pulsation. These motion artifacts can be greatly reduced by raising the spinal vertebral slightly using the modified stabilizing spinal clamps (**Fig. 2.1D-F, 2.2B**). Inspection and readjustment of the spinal clamps are needed prior to each imaging session if stabilization fails. Second, it is critical to prevent blood seeping into the imaging window from peripheral tissues (bone, muscles, and skin). An effective measure to stop bleeding is to apply gelfoam to all the gaps between bones and muscles followed by a seal using tissue adhesive glue. Third, the choice of the fluorescein-conjugated dextran tracers is also particular for this application. As one main blood plasma protein, serum albumin does not extravasate from the endothelium under physiological conditions. The chosen tracers (70 kDa) have slightly higher molecular weight than serum albumin (66 kDa), so the endothelium is also impermeable to the dyes under normal conditions (Egawa et al., 2013). In response to SCI, the endothelium is disrupted and becomes permeable to these tracers. Their leakage in the parenchyma leads to elevated fluorescent intensity outside of the blood vessel (**Fig. 2.3F-G**, arrows). Lastly, the delivery route via external jugular vein is chosen for both flexible accessibility and a route of potential drug administration.

It is worthwhile to address some caveats regarding this novel vascular imaging method. To begin with, this technique is customized to measure vascular changes at a pair of pre- and post-injury time points in the studies mentioned in the next few chapters. Given more available fluorescent colors and imaging channels, it is feasible to investigate multiple time points. Furthermore, several previous chronic intravital imaging studies installed a glass imaging chamber, which made it difficult to align baseline and post-injury changes on the same vessels (Davalos et al., 2008, Davalos and Akassoglou, 2012, Farrar et al., 2012, Evans et al., 2014, Tang et al., 2015). My imaging window is a coverless design suitable for the demand of pre- and post-injury imaging at the acute phase of SCI. For long-term observation, the imaging window would require further optimization. A technical improvement such as detachable glass coverslip or imaging chamber may solve the problem for chronic imaging. Finally, the current approach solely relies on vascular morphology and blood flow rate to distinguish vessel types (**Table 2.1**). The method may be optimized to use a specific tracer which recognizes the arteries (Shen et al., 2012). Improvement on identifying different blood vessel types, including morphological features and functions, can help to elucidate the systemic changes of the entire vascular network. Additionally, I only used female SD rats for this study because my pilot study showed male rats have difficulty to maintain the required sedated state under the same dosage of anesthetic drug, ketamine, compared to female counterparts. This may be due to the sex differences in ketamine pharmacokinetics in rats and male rats are likely to have a greater ability to produce metabolite of ketamine (Waterman and Livingston, 1978, Saland and Kabbaj, 2018).

This imaging technique has various applications besides traumatic models. It can be also applied to studies related to neurodegenerative diseases such as amyotrophic lateral sclerosis (ALS) and multiple schlerosis (MS) to detect abnormalities in Blood-CNS barrier. In addition, the method can be combined with transgenic animal models with specific labeling of endothelial cells or astrocytes to study the neurovascular coupling. Lastly, the efficacy of potential drugs targeting vascular dysfunction could be tested using this imaging technique.

In the following chapters, this imaging tool will be applied to assess vascular dysfunction following a cervical SCI model. In the next chapter, this in vivo duo-color method provided a reliable characterization of temporospatial vascular changes following SCI. In chapter 4, this method was applied for screening a nanoparticle treatment to reduce vascular dysfunction-induced secondary damages.

CHAPTER 3

CHARACTERIZATION OF A TEMPOROSPATIAL PROFILE IN DYNAMIC VASCULAR CHANGES CORRELATING WITH DIFFERENT CELLULAR CHANGES FOLLOWING A CERVICAL SPINAL CORD INJURY

Hypotheses

1) A contusive SCI induces a rapid and large-scale vascular disruption beyond the direct impact site. 2) At acute phase, a temporospatial profile of vascular changes correlating with other cellular pathological changes defined three regions: epicenter (disruption in both vasculature and neuronal components), transitional zone (disruption only in the vasculature), and remote zone (no changes in both). 3) In the transitional zone, immediate vascular changes occur prior to the loss of neuronal components.

Introduction

The endothelial cells of spinal blood vessels appear to be the first cells to die following traumatic SCI (Griffiths et al., 1978, Casella et al., 2006). Ultrastructural studies show pathological changes in vasculature minutes after SCI (Goodman et al., 1979, Koyanagi et al., 1993a). Unlike an isolated organ, the formation of blood vessels in the spinal cord often accompany neurogenesis during early development and integrate into an intricate and homeostatic network communicated with other cells in the CNS system that are the first line of defense against outside challenges. The microvasculature within the spinal cord is composed of an integrated unit consisting of not only the endothelial cells and tight junctions, but also pericytes, astrocytes, and neurons (Benton et al., 2009a). The perturbation of the vascular network induced by SCI often triggers disruptions at multiple levels and a series of cascades simultaneously. Previous studies reported immediate vascular events following SCI, including hemorrhage (Noble and Wrathall, 1985), vasospasm (Anthes et al., 1996), edema (Sharma et al., 1991, Nesic et al., 2006, Yashon et al., 1973), and ischemia (Dolan and Tator, 1982, Sandler and Tator, 1976), as well as the breakdown of the blood-spinal cord barrier (BSCB)(Sharma, 2005, Benton et al., 2008). Angiogenesis for the reorganization of the vascular network, was also reported as a delayed vascular event (Fassbender et al., 2011, Loy et al., 2002, Casella et al., 2002, Benton et al., 2008). Numerous cases show that perturbation of the anatomical and functional integration of the microvasculature can result in neural pathology (Hawkins and Davis, 2005). Since the vascular injury is a hallmark of SCI, targeting its disruption may represent a promising strategy as the preservation of metabolic support of spinal tissue spared by the primary injury should result in the enhanced substrate for functional recovery (Benton et al., 2009a). To date, research on vascular injury and repair remains to be a largely underexplored field for clearly dissected mechanisms and effective therapeutic treatments.

To begin with, a comprehensive profile of the vascular dynamic changes following SCI is in urgent need for identifying the most important factor(s) contributing to neural pathology. In addition, correlating the changes in spinal vasculature and other cellular responses to SCI in time and space will reveal more clues of direct or indirect mechanisms of progressive neural damage. During the development of in vivo spinal vascular imaging technique, my initial study found rapid and large-scale vasodilation and blood protein extravasation in the acute phase of SCI. The range of this phenomenon was beyond the scope of primary injury brought by the mechanical impact. This finding was not mentioned in the previous understanding of the pathophysiological pattern following SCI. A conventional explanation is that the lesion starts from the direct injury site and expands rostrocaudally over time leading to the death of initially viable axons and cells resulting in a deleterious functional loss (Tator and Fehlings, 1991, Onifer et al., 2007b). Here I hypothesize that at the acute phase of SCI there is a spinal cord region at a “transitional” state where vascular disruptions occur, yet no other cellular changes. Thus, the following experiments were designed to test the alternative hypothesis.

To characterize the temporospatial changes of spinal cord vasculature following SCI, I conducted the following study using a novel *in vivo* imaging method to dynamically measure changes in vessel diameter, and vascular permeability in a moderate SCI model via two-photon laser scanning microscopy (Chen et al., 2017). Combined with histopathological analysis, the present study aims to determine whether a regional difference exists in the temporal relationship between vascular disruption and neuronal pathology, as well as other supporting cells in the CNS.

Materials and methods

Animals and spinal cord injury model

Six weeks old female Sprague-Dawley rats (180-220 g, *n* = 76, Envigo RMS, Inc., Indianapolis, IN) were housed with an air filter in an environmentally-controlled facility with a 12-hour/12-hour light/dark cycle. The animals had free access to food and water throughout the entire study. Prior to surgery, the rats were deeply anesthetized with an intraperitoneal injection of ketamine (87.7mg/kg) and xylazine (12.3mg/kg) mixture. Depending on the purpose of either *in vivo* imaging or histological analysis, a laminectomy was performed either at the cervical 5^{th}-7^{th} vertebrae (C5-C7) or C7 only, respectively. For SCI, the animals received a mild-to-moderate C7 midline contusive injury (tissue displacement = 0.800mm) using a Louisville Injury System Apparatus (LISA) device according to my previously established protocol (Zhang et al., 2008). For two-photon *in vivo* imaging, rats received a C5-C7 laminectomy (n = 32) and were grouped for imaging at different acute time points following SCI: Sham, 0.5 hour post-injury, 2 hour post-injury and 4 hour post-injury groups (n = 8 each group). These animals were terminated after imaging.

For histological analysis, another group of rats received a C7 laminectomy (total n = 44) were divided into the same 4 groups (n = 8 each group), with 2 additional groups: 1 day and 7 day post-injury groups (n = 6 each group). Following injury, the muscles and skin were closed with sutures and antibiotic ointment was applied to the wound. The rats were given a subcutaneous injection of 5 mL 0.9% saline subcutaneously for hydration and placed in temperature-controlled cages to monitor recovery with easy accessibility to water and food. The analgesic buprenorphine (0.05-2.0 mg/kg) was subcutaneously delivered every 6-12 hours post-surgery for 2 days. Bladder expression was applied three times a day. All procedures were approved by the Institutional Animal Care and Use Committee of Indiana University School of Medicine and Institutional Biosafety Committee and were strictly following the National Institutes of Health (NIH) Guide on humane care and the use of laboratory animals.

In vivo spinal vascular imaging

In vivo spinal vascular imaging was performed as previously described (Chen et al., 2017). The step-by-step procedure was also provided in chapter 2. In brief, the animals received a catheterization via an external jugular vein (EJV) for future tracer injections in the first step. The second step is to use a customized device to stabilize 5th to 7th cervical vertebrae followed by a laminectomy. After sealing the surrounding muscle-bone field with tissue adhesive, a line of 4% agar was built around the edge to form the wall for a two-photon imaging window. In the third step of pre-injury imaging, 0.5 mL of Rhodamine B isothiocyanate-dextran (Rho-dextran, 70kDa, Sigma-Aldrich, 4 mg/mL, dissolved in saline) was injected slowly via the EJV catheter. The rats were then placed under a two-photon laser-scanning microscope (2P-LSM, Prairie Technologies, Middleton, WI) focused on the exposed C5-C7 spinal segments. The same fields were identified and imaged at all different time points. At 4x magnification (NA 0.1; Olympus, Shinjuku, Tokyo, Japan), a bright-field image of the surface blood vessel pattern was acquired as a location map using a charge coupled device (CCD) camera. At 10x magnification (NA 0.30; Olympus), a series of Z-stack images with the thickness of 200-400 µm was collected through dorsal spinal tissue across the C5-C7 spinal cord segments. The fourth step is to perform SCI. In the fifth step of post-injury imaging, 0.5 mL of Fluorescein isothiocyanate-dextran (FITC-dextran, 70kDa, 4 mg/mL, dissolved in saline) was slowly injected. The imaging procedure was repeated as performed in the step of pre-injury imaging. For 2P-LSM parameter settings, excitation was provided by a tunable Maitai Ti:sapphire laser (Newport, Mountain View, CA) tuned to 860 nm.

Measurement of vessel diameter and vascular permeability in vivo

The acquired Z-stack images with a depth of 200-400 μm were analyzed via imageJ to measure changes in vessel diameter and vascular permeability. The images were first calibrated based on both the magnification of the objective and the digital enlargement factor recorded during the imaging session. For vessel diameter, a line is drawn perpendicular to the long axis of the vessel segment to measure the diameter. The diameter of the blood vessel is determined by the average of three measurements across the vessel segement. For vascular permeability, a probe of a 200 μm line is drawn both inside and outside the vessel to measure the fluorescence integrated density. The vascular permeability is calculated as the ratio of the outside value divided by the inside value.

Tissue processing for histological assessments

For the groups of animals for histological analysis, tissues were collected and processed as previously described (Liu et al., 2006). At 0.5 hour, 2 hours, 4 hours, 1 day and 7 days after injury, anesthetized animals were transcardially perfused with 100 ml 0.01M phosphate buffer saline, followed by 400 ml of ice-cold 4% paraformaldehyde fixative solution in 0.01M PBS. A 9 mm segment of cervical cord including C5 to C7 was collected and post-fixed in the same fixative overnight, and then transferred to a solution of 30% sucrose in 1x PBS for 5 days. Spinal cord segments were embedded in O.C.T compound (Fisher, Waltham, MA) for cryostat sectioning. The tissues were cut on a cryostat (LeicaCM 1950; Buffalo Grove, IL) in a series of coronal 25-μm-thick sections from 5th to 7th cervical segments mounted on slides, and stored at -20°C. The sections were then processed for immunofluorescence labeling.

Immunofluorescence labeling

After the spinal cord sections were washed in 1xPBS three times at room temperature, blocked in 10% normal goat serum (NGS) or normal donkey serum (NDS) blocking solution (with 0.1% Triton X-100 in 1xPBS) for 1 hour, then incubated with primary antibodies in 5% NGS or NDS and Triton X-100 (0.05% in 1xPBS) at 4°C overnight. After washing in 1xPBS three times, sections were incubated with host-specific secondary antibodies for 1 hour at room temperature, followed by DAPI staining for 5 min. The sections were washed in 1xPBS again three times and coverslips were mounted with Fluoromount-G (SouthernBiotech, Birmingham, AL). The primary antibodies and their final dilutions were used as follows: anti-RECA1 (blood vessels; 1:200, mouse; Bio-Rad, Hercules, CA); anti-GFAP (astrocytes; 1:1000, chicken; Abcam, Cambridge, United Kingdom); anti-APC (oligodendrocytes; 1:400, mouse; Abcam); anti-Iba1 (microglia; 1:500, goat; Abcam); anti-ED1 (macrophages; 1:200, mouse; Abcam); anti-laminin (basement membrane of blood vessels; 1:200, rabbit; Millipore); anti-NeuN (neurons; 1:1000, mouse or rabbit; Millipore); anti-SMI31 (axons; 1:1000, mouse; Biolegend, San Diego, CA); anti-MBP (myelin; 1:200, rat; Millipore). Secondary antibodies with either goat or donkey host were used in a dilution of 1:1000. All information for antibodies is provided in **Table 3.1**. For co-labeling with IgG and laminin, sections were stained with primary and secondary antibodies against laminin regularly as mentioned above; during the step of secondary antibody incubation, a fluorescence-tagged anti-rat IgG antibody (Cy3, 1:1000; Jackson ImmunoResearch Laboratories, Inc., West Grove, PA) was added for one hour in room temperature. Detailed information for antibodies is included in **Table 3.1**.

Table 3.1. Primary and secondary antibodies used in this study

Antigen	Host type	Working dilution	Manufacturer	Catalog#
Primary Antibodies				
Anti-RECA-1	Mouse IgG	1:200	Bio-Rad	MCA970R
Anti-GFAP	Chicken IgY	1:1000	Abcam	ab4674
Anti-APC (CC-1)	Mouse IgG2b	1:400	Abcam	ab16794
Anti-Iba1	Goat IgG	1:400	Abcam	ab5076
Anti-ED1 (CD68)	Mouse IgG	1:200	Abcam	ab31630
Anti-laminin	Rabbit IgG	1:100	Millipore	ab2034
Anti-NeuN	Rabbit IgG	1:1000	Millipore	ABN78
Anti-NeuN	Mouse IgG	1:1000	Millipore	MAB377
Anti-SMI-31	Mouse IgG	1:1000	Biolegend	801601
Anti-MBP	Rat IgG	1:200	Millipore	MAB386
Anti-APC (CC-1)	Mouse IgG2b	1:400	Abcam	ab16794
Anti-laminin	Rabbit IgG	1:100	Millipore	ab2034
Secondary Antibodies				
Alexa Fluor 488 (green)	Goat anti Chicken IgG	1:1000	Abcam	A11039
Alexa Fluor 488 (green)	Goat anti Mouse IgG	1:1000	Life Technologies	A-11029
Alexa Fluor 594 (red)	Goat anti Rabbit IgG	1:1000	Abcam	A11012

CY3	Goat anti Rabbit IgG	1:1000	Millipore	AP132C
CY3	Goat anti Rat IgG	1:1000	Jackson Immunolabs	112-166-143
CY5	Goat anti Mouse IgG	1:1000	Life Technologies	A10524
CY5	Goat anti Rabbit IgG	1:1000	Jackson Immunolabs	111-075-144
CY5	Donkey anti Rabbit IgG	1:1000	Jackson Immunolabs	711-175-152
Alexa Fluor 488 (green)	Donkey anti Goat	1:1000	Life Technologies	A11055
CY3	Donkey anti Mouse	1:1000	Jackson Immunolabs	715-175-150
Hoechst stain 33342		1:1000	Cell Signaling	4082S

Fluorescence microscopy

For immunofluorescence labeling, an inverted fluorescent microscopy system (Zeiss Axiovert 200 M, Jena, Germany) was used to capture images. The microscope was combined with an apotome and interfaced with a digital camera (Zeiss Axio Cam MRc5) controlled by a computer. Images were captured using the apotome with software (AxioVision v4.8) and output as a cut view image. The images were later assembled and quantified in Photoshop CC (Adobe System, San Jose, CA).

Cell counting

The immunofluorescence-labeled images were assessed to quantify various types of cells. At each time point, cells were counted in one section from each region: C5 (remote zone), C6 (transitional zone), and C7 (epicenter) (25 μm thickness, every 120th section from the epicenter, 3000 μm apart, based on the topographical information of the rat spinal cord, 3 sections for each animal). Every single positive cell (even partial positive cell at the borders of sections) was counted in multi-planes throughout the entire designated area in the 25 μm section.

Quantification of blood vessels

To quantify leaky vessels, the sections were processed with antibodies against IgG and laminin; both dorsal white matter and ventral gray matter were examined; the percentage of leaked vessels was calculated by the leaked vessel number over total vessel number in designated areas.

Quantification of neuronal density

To quantify the number of surviving neurons, the sections were processed with antibody against NeuN and ventral gray matter was examined; only cells with a clearly visible DAPI-labeled nucleus were included; neuronal density was calculated by dividing the total NeuN-positive number by the area of contoured ventral gray matter, expressed as average cell number per mm^2.

Quantification of microglial responses

To quantify microglia, the total number and the percentage of ramified and hypertrophied/amoeboid phenotypic cells were examined in ventral gray matter using antibody against Iba1; similar as above, cell density was expressed as average $Iba1^+$ number per mm^2 and the percentage of ramified and hypertrophied/amoeboid microglia were calculated by the number of specific phenotypic cells over total number.

Quantification of astrocytic response

To quantify density of astrocytes in ventral gray matter, antibody against GFAP was used and the cell density was expressed as the average number per mm^2. To quantify the average astrocyte area in mm^2 (Total GFAP area divided by cell number) and the integrated density of GFAP, a 300 μm x 300 μm area was selected in the ventral gray matter 500 μm away from the midline using the function of Analyze Particles in ImageJ software.

Quantification of axonal count and size, myelin responses

To quantify axons and myelination, antibodies against SMI-31 and MBP were used and the designated dorsal white matter area (a 200 μm x 150 μm area was selected 200 μm away from the central canal) was examined. Both axon and myelin were measured using ImageJ, expressed as total axon count, average axon size in mm^2, total myelin area, and myelin area per axon in mm^2.

Quantification of oligodendrocytes

To quantify the density of oligodendrocytes in the dorsal white matter, an antibody against APC (CC-1) was used and cell density was calculated the same as counting neuronal density.

Statistical analysis

The data of *in vivo* diameter were analyzed using a one-way ANOVA of variance test followed by a Dunnett's multiple comparison test. The quantifications of immunofluorescence-labeled cell data were presented as average ± standard deviation and analyzed using a one-way ANOVA of variance test followed by a Tukey post-hoc test. Both analyses used GraphPad Prism 7 (GraphPad Software, Inc.; La Jolla, CA). Statistical significance was set at $p < 0.05$. *In vivo* permeability data were analyzed using repeated measure two-way ANOVA followed by LSD as post-hoc test via SPSS software IBM Corporation, Armonk, NY. Significance was set at $p < 0.05$.

Results

Simultaneous vasodilation and leakage occur in the epicenter and adjacent area

I first observed the temporal and spatial changes in spinal vasculature induced by SCI *in vivo* (**Fig. 3.1A-D**). According to my previous studies, this preparation allows assessment of the changes in vessel diameter and vascular permeability (Chen et al., 2017). After sequentially delivering the tracers to the rat intravenously, I detected the responses of the spinal vessels at 0.5 hour, 2 hour, and 4 hour post-injury, compared to baseline and sham controls. To observe the regional differences, three segments of the exposed cervical spinal cord were observed for vascular changes simultaneously: epicenter (C7), adjacent (C6), and remote (C5) cord regions (**Fig. 3.1E**).

I confirmed laminectomy alone did not induce any changes in vessel diameter up to 4-hour after the procedure (**Fig. 3.1A**). As early as 0.5 hour after SCI, I found significant vasodilation (arrows) and extravasation of blood content (**) in both the injury epicenter and the adjacent cord region, whereas no significant change in the remote region (**Fig. 3.1B**). Both epicenter and the adjacent region had similar increased fold change in the vessel diameter (epicenter: 1.481±0.609, adjacent: 1.472±0.664; p=0.0001, compared to baseline; **Fig. 3.1F**). The vessels in the remote region started to significantly dilate at a later time point of 2 hour after SCI and the vasodilation across three regions was persistent up to 4 hour post-injury during observation (**Fig. 3.1C-D, F**). To further identify the differential responses in vessel types, I categorized all the spinal vessels into arteries and veins based on the criteria of their morphology and red blood cell velocity (Chen et al., 2017). The response of the veins was similar to the diameter changes in all vessels, whereas the arteries showed a slightly delayed response (**Fig. 3.1G-H**). Therefore, the detected

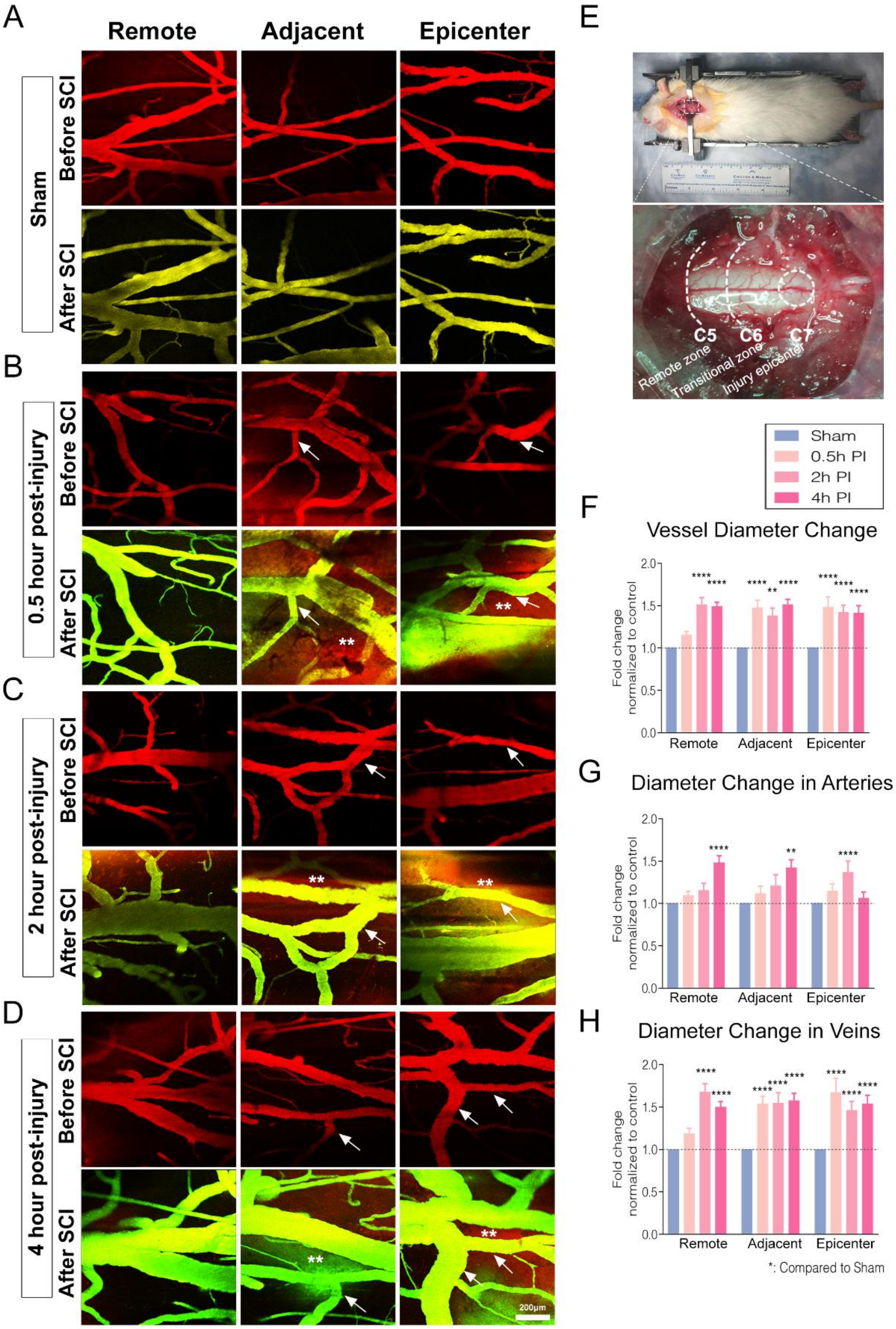
A
Remote
Adjacent
Epicenter
Sham
Before SCI
After SCI
B
0.5 hour post-injury
Before SCI
After SCI
**
C
2 hour post-injury
Before SCI
After SCI
**
D
4 hour post-injury
Before SCI
After SCI
**
200μm
E
C5
C6
C7
Remote zone
Transitional zone
Injury epicenter
Sham
0.5h PI
2h PI
4h PI
F
Vessel Diameter Change
Fold change normalized to control
2.0
1.5
1.0
0.5
0.0
Remote
Adjacent
Epicenter
****
**
G
Diameter Change in Arteries
Fold change normalized to control
2.0
1.5
1.0
0.5
0.0
Remote
Adjacent
Epicenter
****
**
H
Diameter Change in Veins
Fold change normalized to control
2.0
1.5
1.0
0.5
0.0
Remote
Adjacent
Epicenter
****
*: Compared to Sham

Figure 3.1. Immediate vascular dilation occurs simultaneously in the epicenter and the adjacent zone after SCI.

Before and after SCI, *in vivo* imaging of the same spinal vessels from 3 different regions, epicenter, adjacent zone, and remote zone, using 2-photon laser-scanning microscopy in (**A**) Sham, (**B**) 0.5 hour, (**C**) 2 hour, and (**D**) 4 hour post-injury. (**E**) Display of the observed regions from 5th to 7th cervical segments during *in vivo* imaging. Quantification of the temporospatial changes of diameters in (**F**) overall vessels, (**G**) arteries, and (**H**) veins. Error bars represent ± s.e.m. Groups: 0.5 hour (n=8), 2 hour (n=6), 4 hour (n=12), Sham (n=3). $^*P<0.05$, $^{**}P<0.01$, $^{***}P<0.001$, **** $P<0.0001$ ns, not significant. Scale bar = 200 µm.

vascular responses in both epicenter and the adjacent area were mainly venous dilation.

The observed blood content extravasation in the parenchyma indicated that vascular permeability has changed in response to SCI. Thus, I measured the fluorescent intensity of the first Rho-Dextran tracer (red) outside versus inside the vessel to calculate vascular permeability (**Fig. 3.2A-D**). The higher the ratio of outside versus inside, the greater the vessel permeability. I found vessels in the epicenter started to leak at 0.5 hour after injury and the level of leakage increased within time, as shown in the quantification results (**Fig. 3.2B and E**, Epicenter). The adjacent area had elevated vascular permeability simultaneously with epicenter, but at a less degree of leakage (**Fig. 3.2B and E**, Adjacent). Compared to these two regions, the remote zone has not shown any significant changes up to 4-hour post-injury yet (**Fig. 3.2B and E**, Remote).

Based on the observation of immediate vascular responses beyond the initial mechanical injury area, I now termed the adjacent area “transitional zone”.

Histological evidence validates vessel leakage in both gray and white matter

To verify whether the *in vivo* detected vascular disruption occurs in a deeper and longer temporospatial profile, I used immunofluorescence staining against immunoglobin G (IgG) and laminin (see Table. 3.1) to identify and quantify disrupted blood vessels in both white and gray matter of the spinal cord up to 7 day post-injury (**Fig. 3.3 A-F and Fig. 3.4 A-F**).

For white matter, I have chosen the dorsal white matter area close to the central canal because this area is located in the direct injury site (**Fig. 3.3 G**). IgG is considered as a marker of disruption in the blood-CNS barrier. In an intact blood vessel, plasma protein IgG cannot cross the barrier so there is no leakage of IgG in the spinal cord parenchyma;

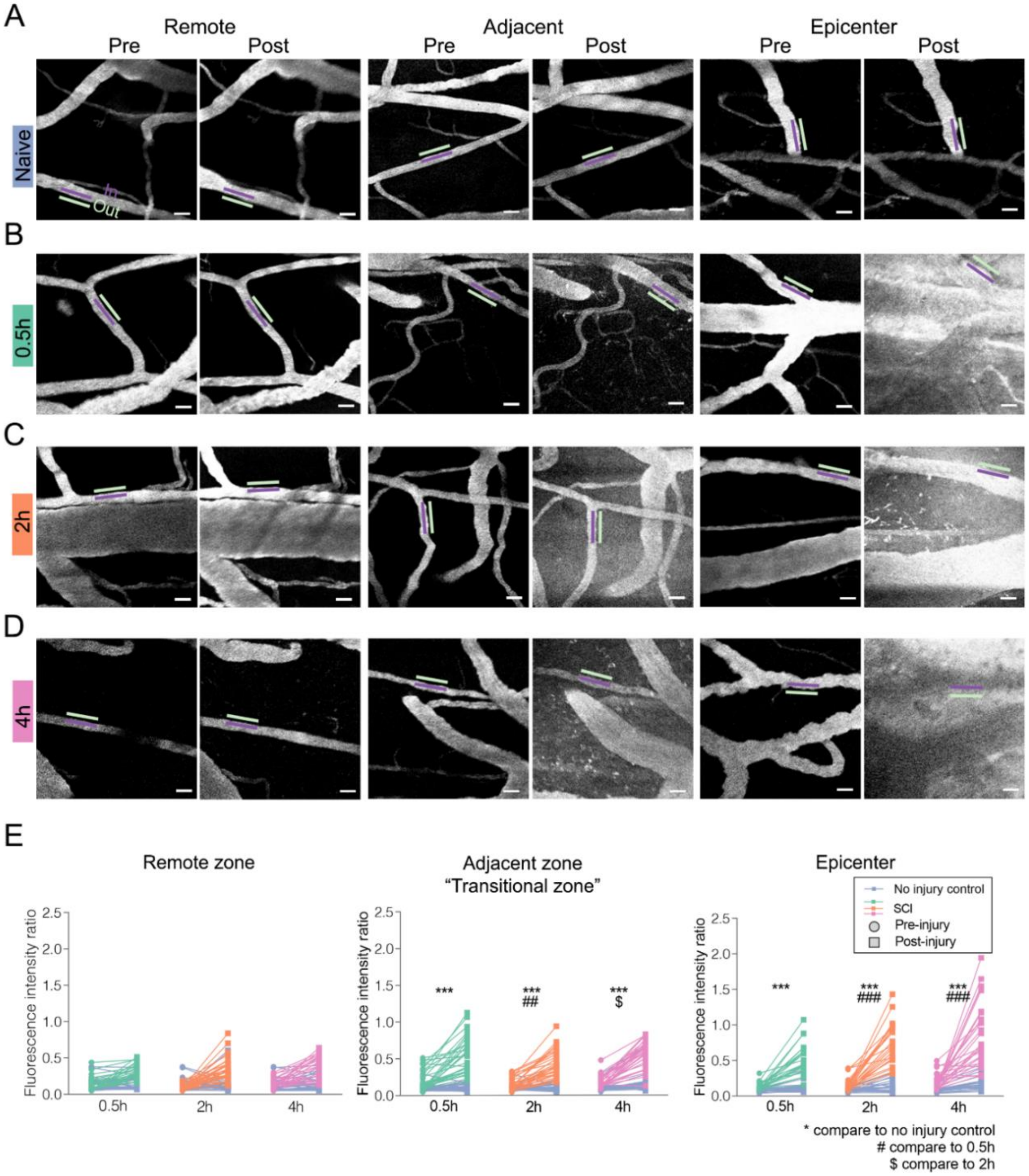

Figure 3.2. Simultaneous increase of the vascular permeability in the epicenter and the transitional zone after SCI.

In 3 different regions, epicenter, transitional zone, and remote zone, the vessel permeability measurement of the same spinal vessels before and after SCI in (**A**) Naïve, (**B**) 0.5 hour, (**C**) 2 hour, and (**D**) 4 hour post-injury. The purple bar measures the fluorescent intensity of the rhodamine-dextran dye inside the vessel whereas the white bar measures outside the vessel. (**E**) Quantification of the temporospatial changes of vessel permeability in remote, transitional, and epicenter. * compared to no injury control, # compared to 0.5 hour post-injury, $ compared to 2 hour post-injury. * or # or $ $P<0.05$, ** or ## or $$ $P<0.01$, *** or ### or $$$ $P<0.001$. Groups: 0.5 hour (n=8), 2 hour (n=6), 4 hour (n=12), Sham (n=3). Scale bar = 50 µm.

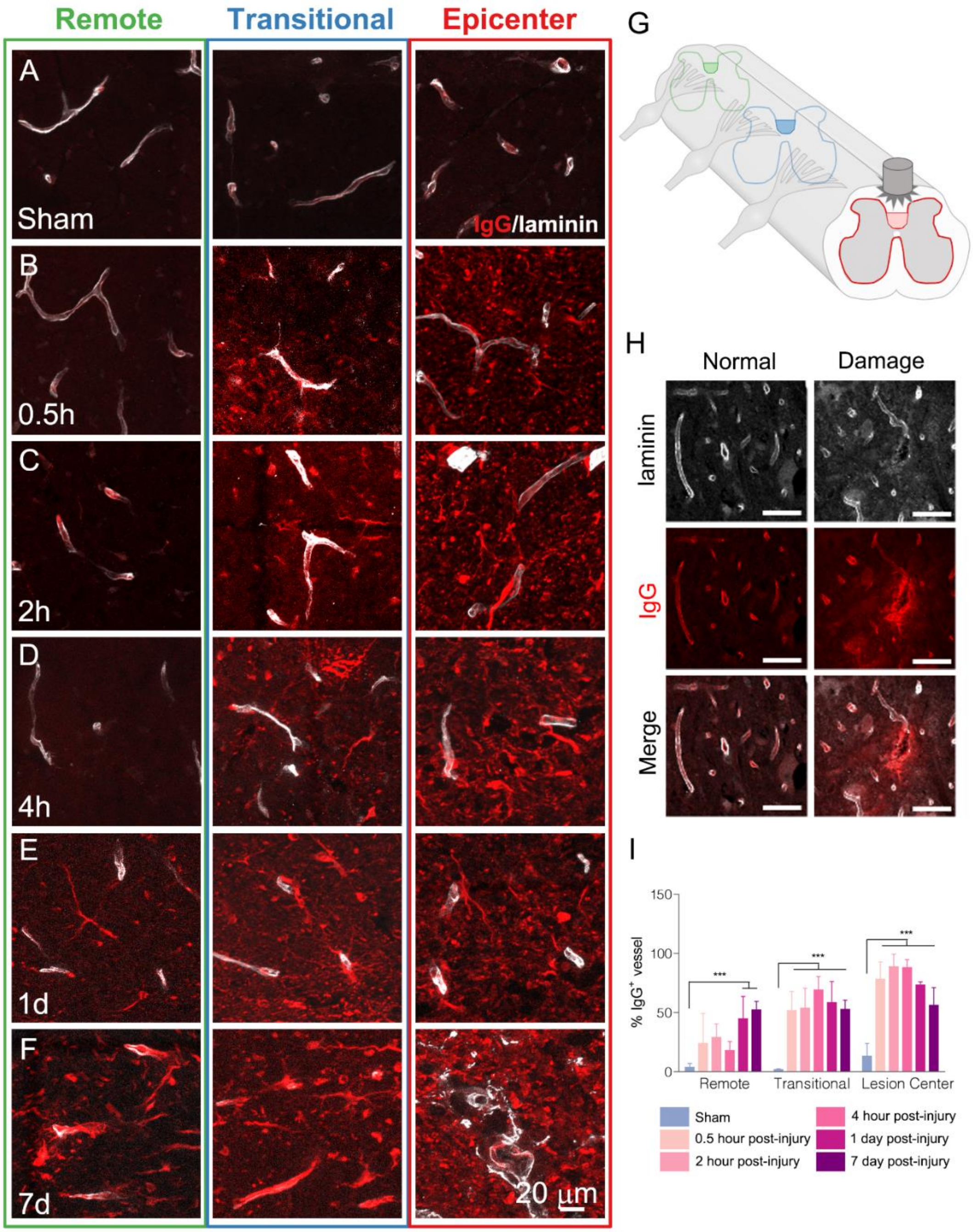

Figure 3.3. Histological evidence of simultaneous leaky vessels in the epicenter and the transitional zone in the white matter.

In the white matter, (**A**) normal vessels become leaky, labeled by IgG and laminin, in both epicenter and the transitional zone starting (**B**) 0.5 hour post-injury. The vessels were later monitored at various time points: (**C**) 2 hour, (**D**) 4 hour, (**E**) 1 day, and (**F**) 7 day post-injury. (**G**) A schematic diagram showing the observed regions in the white matter. (**H**) An example of the normal and damaged vessel double-labeled by IgG and laminin. (**I**) Quantification of the percentage of IgG+ vessels over total laminin+ vessels. Error bars represent ± SD. n=7 for sham, 0.5h, 2h, and 4h post-injury group, n=6 for 1 day and 7 day post-injury group. $^{*}P<0.05$, $^{**}P<0.01$, $^{***}P<0.001$. Scale bar = 20 µm in (**A-F**); Scale bar = 50 µm in (**H**).

In contrast, damaged blood vessels display IgG leaks outside into the parenchyma (**Fig. 3.3H**). Similar to the *in vivo* imaging results, I found a significant IgG-labeled vessel disruption simultaneously in both the epicenter and the transitional zone as early as 0.5 hour post-injury (**Fig. 3.3B and I**, Epicenter: 78.23±14.54%, Transitional: 51.76±16.06%; p=0.0001, compared to sham controls); the remote zone did not show any drastic leakage at the same time point (**Fig. 3.3B and I**, Remote: 24.01±25.13%; p=0.2305, compared to sham controls). This phenomenon remained at 2 hour and 4 hour post-injury (**Fig. 3.3C-D**). At 1 day post-injury, IgG leakage became significantly increased in the remote zone (**Fig. 3.3E and I**, Remote: 44.63±18.91%; p=0.0034, compared to sham controls). Then my observation found the level of leakage across three regions was persistent up to 7 day post-injury (**Fig. 3.3F and I**, Remote: 52.2±7.279%, p=0.0006; Transitional: 52.86±7.608%, p=0.0002; Epicenter: 56.33±14.74%, p=0.0001).

For gray matter, I assessed the area of ventral horn due to its high vulnerability in response to SCI (**Fig. 3.4G**). Similar to dorsal white matter, the epicenter region displayed significant IgG leakage starting at 0.5 hour post-injury (**Fig. 3.4B and H**). Both the lesion epicenter and the transitional zone responded within 2 hour after injury, whereas the remote zone has no significant increase in vessel leakage (**Fig. 3.4A-F and H**). These results collectively validate that vessel leakage occur in both white and gray matter but in a differential spreading pattern along the dorsal-ventral axis and rostral-caudal axis.

Vascular disruption occurs prior to neuronal loss in the transitional zone

To examine the injury-induced neuronal loss, I immunofluorescent-labeled NeuN and DAPI to assess the neuronal density in the same area of ventral horn across three regions

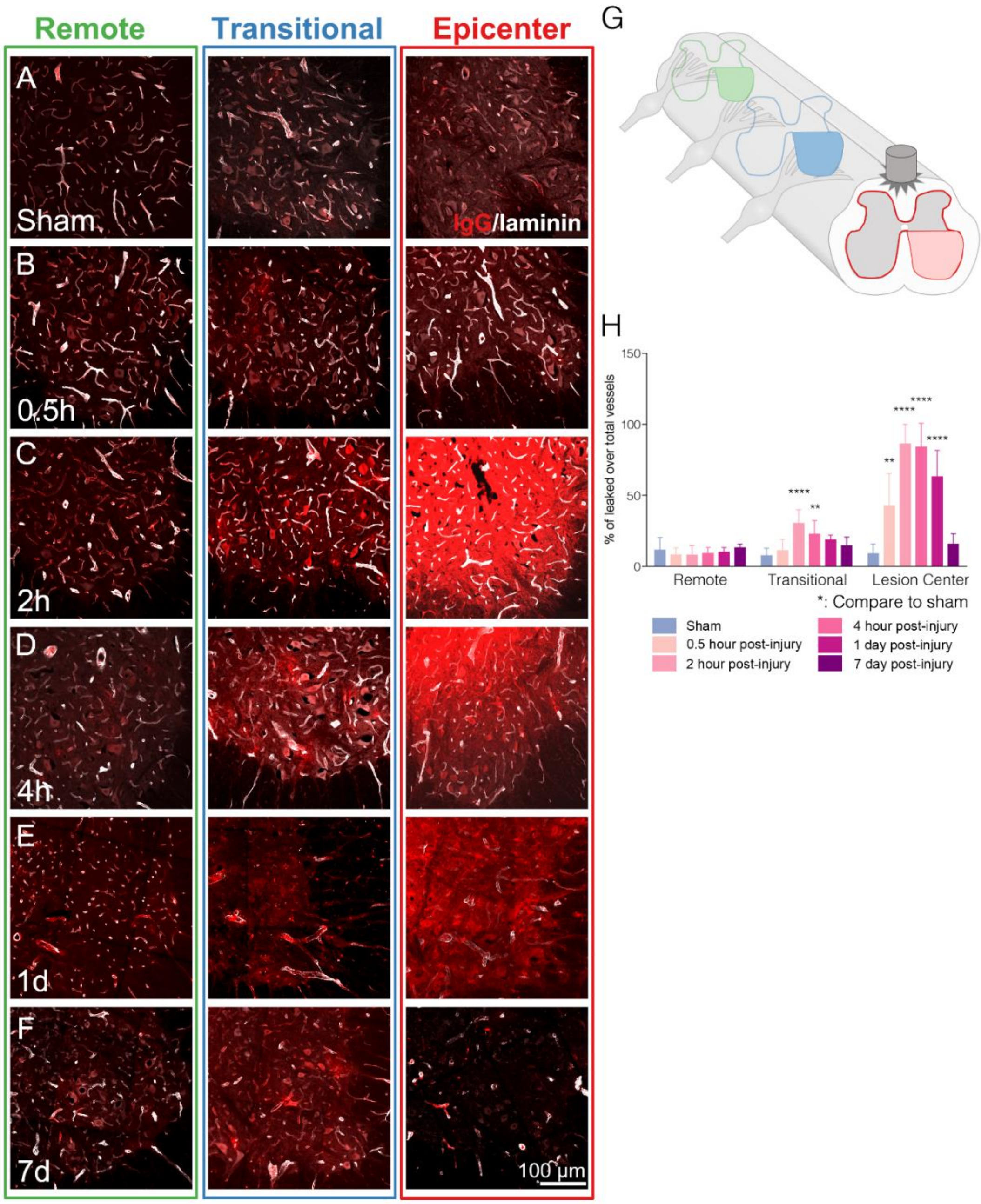

Figure 3.4. Histology also validates the vessel leakage in the gray matter.

In the gray matter, (**A**) normal vessels also become leaky in the epicenter starting (**B**) 0.5 hour post-injury and the transitional zone starting (**C**) 2 hour post-injury. The vessels were later monitored at other various time points: (**D**) 4 hour, (**E**) 1 day, and (**F**) 7 day post-injury. (**G**) A schematic diagram showing the observed regions in the gray matter. (**H**) Quantification of the percentage of IgG+ vessels over total laminin+ vessels. Error bars represent ± SD. n=7 for sham, 0.5h, 2h, and 4h post-injury group, n=6 for 1 day and 7 day post-injury group. *P<0.05, **P<0.01, ***P<0.001. Scale bar = 100 μm in (**A-F**).

(**Fig. 3.5G**). In the sham controls, the neuronal density is approximately 200 per mm^2 across three regions (**Fig. 3.5A and H**, Remote: 221.9±33.89; Transitional: 189.4±32.63; Epicenter: 212.1±51.28, $p>0.05$). At 0.5 hour and 2 hour post-injury, the neuronal density remained statistically unchanged (**Fig. 3.5B-C**). The epicenter showed a significant decline in the neuronal density of the ventral horn at 4 hour after SCI (**Fig. 3.5D**, 143.50±39.61 per mm^2) and continued to decrease up to 7 day post-injury (**Fig. 3.5F,** 70.58±21.55 per mm^2). The transitional zone showed a delayed decrease at 1 day post-injury (120.30±33.46 per mm^2) and persisted up to 7 day after injury (114.10±11.62 per mm^2). No statistically significant decrease was shown in the remote zone. Note that in the transitional zone the neuronal loss (1 day post-injury) lagged the vascular disruption (2 hour post-injury). Therefore, this result identified a time window between vascular leakage and neuronal loss in the transitional zone.

Microglial activation also occurs after vascular changes in the transitional zone

To determine whether inflammatory responses associated with the detected vascular and neuronal changes, I investigated the microglial response in the ventral horn, double-labeled by Iba1 and DAPI (**Fig. 3.6A-B**). Besides evaluating the changes in cell density, I also categorized the microglia into two subtypes based on morphology. Microglia in the CNS is known for transforming from a ramified/quiescent state into a hypertrophied or amoeboid state in response to a traumatic insult or stress (**Fig. 3.6C**) (Xu et al., 2016, Davalos et al., 2005, Nimmerjahn et al., 2005, Davis et al., 1994). In the sham controls, the resident microglia present its ramified morphology across all three regions (**Fig. 3.6D**). At 0.5 hour post-injury, microglia has not shown any changes in all three regions, including

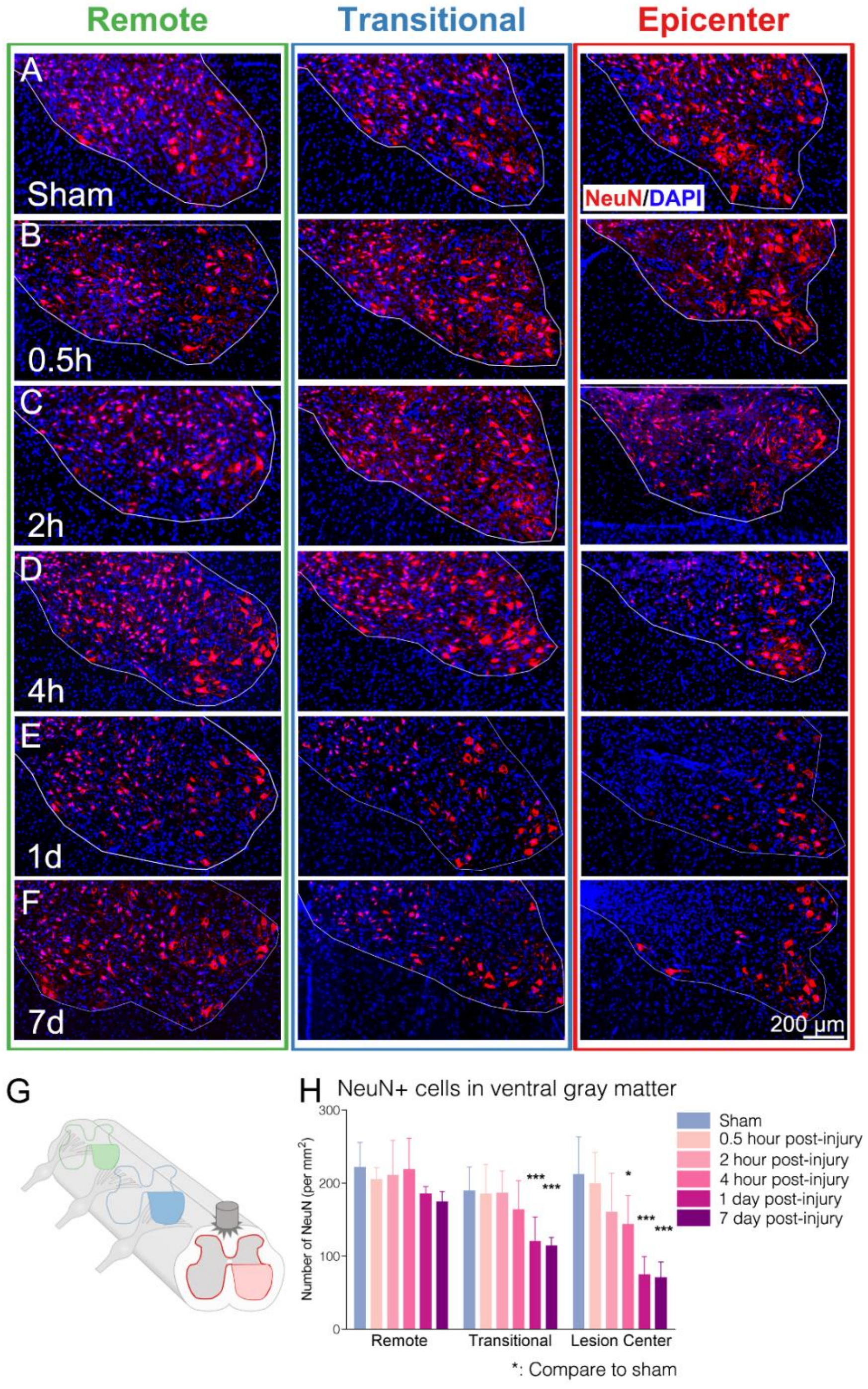

Figure 3.5. Neuronal loss lags vessel leakages in the transitional zone.

In 3 different regions (epicenter, transitional zone, and remote zone), the number of neurons (double-labeled by NeuN and DAPI) was counted in (**A**) Sham, (**B**) 0.5 hour, (**C**) 2 hour, (**D**) 4 hour, (**E**) 1 day, and (**F**) 7 day post-injury. In the epicenter, the neuronal loss started at 4 hour post-injury; in the transitional zone, the neuronal loss started at 1 day post-injury and this lags behind vessel leakages. (**G**) A schematic diagram showing the observed regions in the gray matter. (**H**) Quantification of neuron density (NeuN$^+$/DAPI$^+$). Error bars represent ± SD. n=7 for sham, n=8 for 0.5h, 2h, and 4h post-injury group, n=6 for 1 day and 7 day post-injury group. *$P<0.05$, **$P<0.01$, ***$P<0.001$. Scale bar = 200 μm.

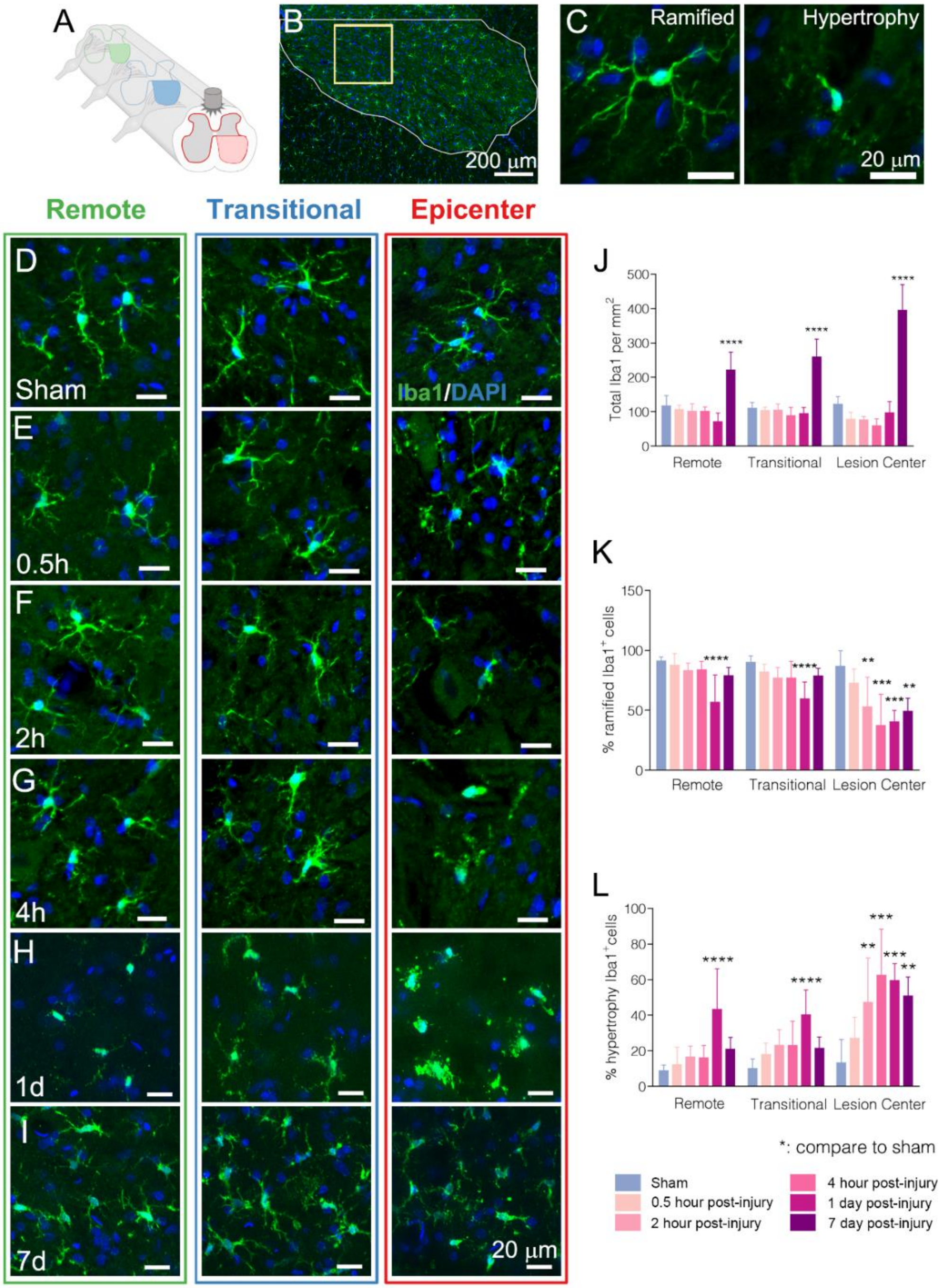

Figure 3.6. Microglial activation also lags vascular changes in the transitional zone.

(**A**) A schematic diagram showing the observed regions in the gray matter. (**B**) Representation of the location for quantification of the microglial process area. (**C**) An example of the ramified and hypertrophied/amoeboid microglia double-labeled by Iba1 and DAPI. In 3 different regions (epicenter, transitional zone, and remote zone), (**J**) the total number, (**K**) ramified microglia cell number, (**L**) percentage of the hypotrophy cell number, and (**M**) the area of microglial process were measured in (**D**) Sham, (**E**) 0.5 hour, (**F**) 2 hour, (**G**) 4 hour, (**H**) 1 day, and (**I**) 7 day post-injury. Error bars represent ± SD. n=6 for sham, 0.5h, 2h, 4h, 1 day and 7 day post-injury group. *P<0.05, **P<0.01,

****P*<0.001. Scale bar in (**B**) is 200 μm; Scale bar = 20 μm in (**C**); Scale bars = 20 μm in (**D-I**).

the total microglial density, the percentage of ramified or hypotrophy microglial cells, and the area of microglial processes (**Fig. 3.6E, J-M**). Starting at 2 hour post-injury, the epicenter showed a pattern of decreased ramified/ increased hypotrophy microglia with no change in total cell density, whereas the other two zones remained no significant changes (**Fig. 3.6F**). This trend was persistent at 4 hour post-injury, except for the decrease in the area of processes in both epicenter and transitional zone (**Fig. 3.6G and M**). At 1 day post-injury, both the reduced ramified microglia and increased hypotrophy microglia ratio were markedly changed across three regions while the total number maintained (**Fig. 3.6H**). At 7 day post-injury, the total number of microglia was drastically increased across all three regions, indicating possible microglial proliferation or cell migration from other areas; the ratio of ramified and hypotrophy microglia returned to level of sham controls in both remote and transitional zone, whereas the significant difference remained in the epicenter; the area of microglial processes also increased in the epicenter (**Fig. 3.6I**). Thus, I determined that microglial responses also fall behind the vascular disruption in the transitional zone.

Reactivation of astrocytes also lags vascular changes

Astrocytes are reportedly contributing to the barrier properties by extending end feet of processes towards the basal lamina layer outside ECs, indicating an important role associated with changes in the vascular permeability (Abbott et al., 2010). I first assessed the density of GFAP$^+$/DAPI$^+$ cells, followed by the cell size and the level of GFAP expression in the ventral gray matter (**Fig. 3.7**). The spinal cord astrocytes display a typical protoplasmic morphology with the stellate shape in sham controls (**Fig. 3.7A**). At 0.5 hour

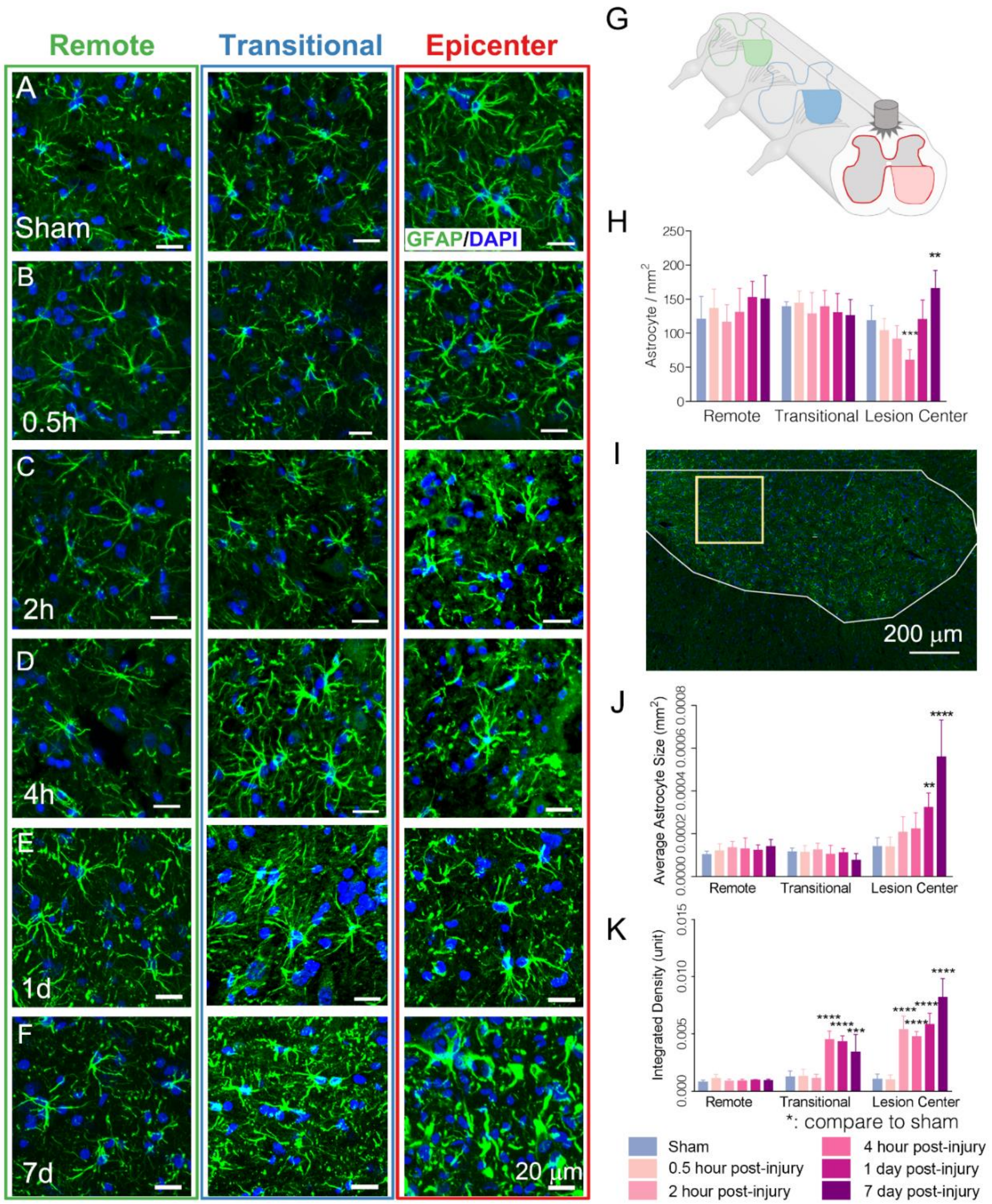

Figure 3.7. Reactivation of astrocytes lags vascular changes in the gray matter.
In 3 different regions (epicenter, transitional zone, and remote zone), the number of astrocytes (double-labeled by GFAP and DAPI) was counted in (**A**) Sham, (**B**) 0.5 hour, (**C**) 2 hour, (**D**) 4 hour, (**E**) 1 day, and (**F**) 7 day post-injury. (**G**) A schematic diagram showing the observed regions in the gray matter. (**H**) Quantification of astrocyte density (GFAP$^+$/DAPI$^+$). (**I**) Representation of the location for quantification of average astrocyte size and integrated density. (**J**) Quantification of average astrocyte size in mm^2. (**K**) Quantification of the astrocyte integrated density in the unit. Error bars represent ± SD. n=7 for sham, n=8 for 0.5h, 2h, and 4h post-injury group, n=6 for 1 day and 7 day post-

injury group. *$P<0.05$, **$P<0.01$, ***$P<0.001$, **** $P<0.0001$. Scale bars = 20 μm in (**A-F**). Scale bar = 200 μm in (**I**).

after SCI, no changes occurred in all astrocytic responses (**Fig. 3.7B, H, J and K**). Starting at 2 hour post-injury, the astrocytes in the epicenter showed increased GFAP expression (**Fig. 3.7C**). The continuous GFAP elevation in the epicenter led to a marked reduction in cell density of astrocytes at 4 hour post-injury; meanwhile, the GFAP expression elevated significantly in the transitional zone but no changes in cell density (**Fig. 3.7D**). At 1 day post-injury, the epicenter restored to a similar level of cell density as sham controls; however, the average size of cell body slightly increased and the GFAP expression remains high; Besides the transitional zone possessed a high level of GFAP expression, no other significant changes were found in both remote and transitional zone (**Fig. 3.7E**). At 7 days post-injury, the epicenter showed a marked increase of cell density, as well as average cell size and GFAP expression; the transitional zone continued to show elevated GFAP expression but no changes in density and cell size (**Fig. 3.7F**). My data demonstrated that GFAP signal started to elevate in the transitional zone at 4 hour post-injury, slightly lagging the vascular leakage demonstrated earlier.

The changes in another neuronal component: axonal loss and myelin response

To determine the temporal relationship between vascular disruption and other neuronal components, I assessed the axons and myelination (co-labeled by SMI-31 and MBP) in the dorsal white matter area above the central canal (**Fig. 3.8B**). It is the same area where I quantified vascular leakage (**Fig. 3.3**). I first counted the axon number and average axon size using imageJ. Compared to sham controls, SCI has not led to any significant changes at 0.5 hour after injury; starting at 2 hour post-injury, the epicenter showed reduced number of axons and the phenomenon remained at 4 hour post-injury; at 1 day post-injury, the

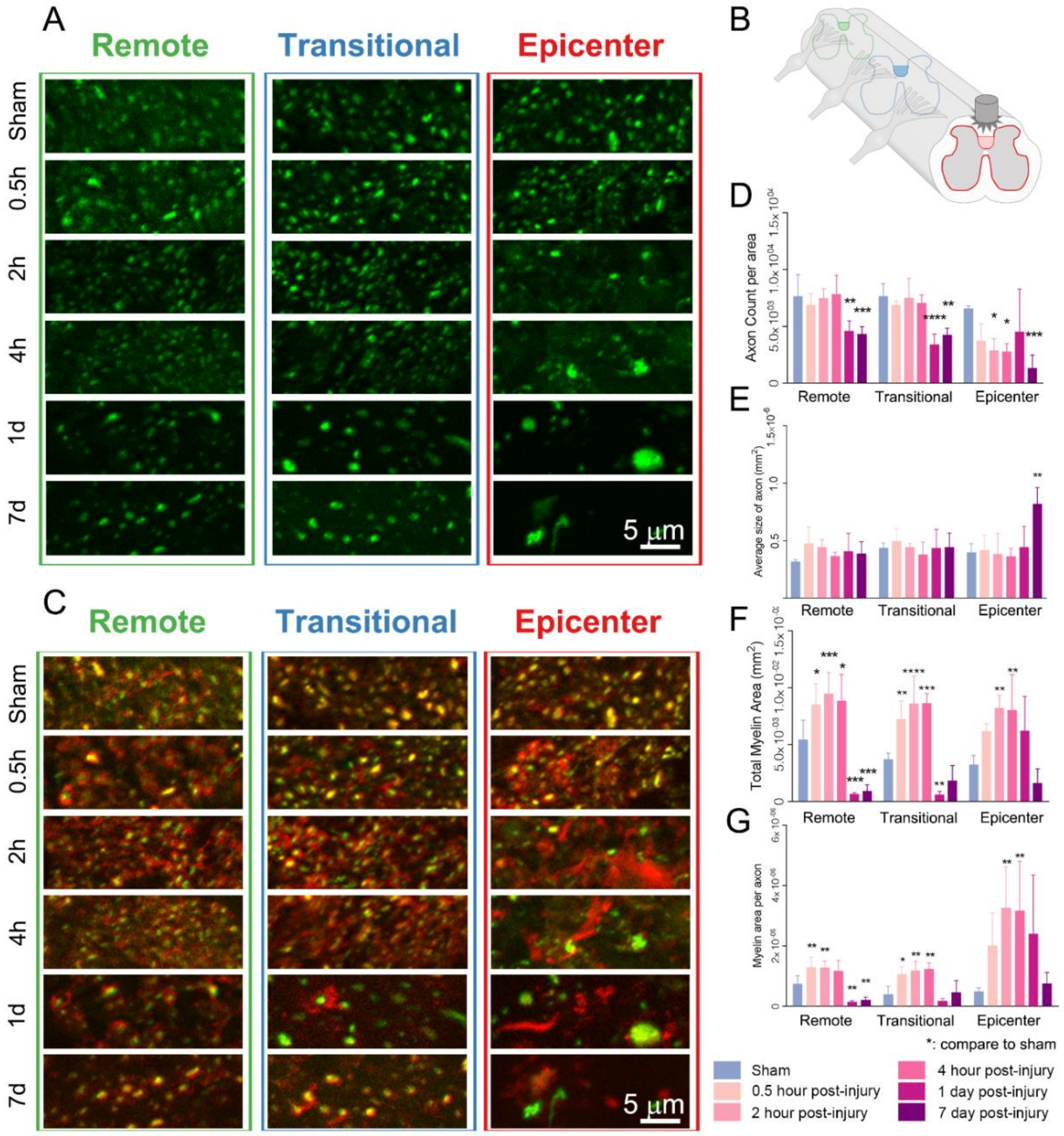

Figure 3.8. Axonal loss and myelin responses.

(**A**) In 3 different regions (epicenter, transitional zone, and remote zone), the axon labeled by SMI-31 was stained in Sham, 0.5 hour, 2 hour, 4 hour, 1 day, and 7 day post-injury. (**B**) A schematic diagram showing the observed regions in the white matter. (**C**) In 3 different regions (epicenter, transitional zone, and remote zone), the axon and myelin double-labeled by SMI-31 and MBP were stained in Sham, 0.5 hour, 2 hour, 4 hour, 1 day, and 7 day post-injury. (**D**) Quantification of axon number density in mm^2. (**E**) Quantification of average axon size in mm^2. (**F**) Quantification of total myelin area in mm^2. (**G**) Quantification of myelin area per axon in mm^2. Error bars represent ± SD. n=7 for sham, n=8 for 0.5h, 2h, and 4h post-injury group, n=6 for 1 day and 7 day post-injury group. * compared to sham control, # compared to 7 day post-injury. * or # $P<0.05$, ** *or ##* $P<0.01$, *** or ### $P<0.001$, **** or #### $P<0.0001$. Scale bars = 5 µm in (**A**) and (**C**).

axonal number was reduced across all three regions while no changes were observed for average size of axons; at 7 day post-injury, the axonal number was further reduced and the axonal size increased in the epicenter (**Fig. 3.8A, D-E**).

To assess the myelin response to the injury, I also calculated total MBP^+ area and MBP^+ area per axon (**Fig. 3.8C, F-G**). Interestingly, myelin immediately responded to the injury at 0.5 hour post-injury in all three regions; the elevation in both total area and myelin area per axon were persistent up to 4 hour post-injury. The elevation indicated the myelin became less compact and no longer wrapping around the axons; At 1 day and 7 day post-injury, the myelin structures had a sharp decrease in all three regions. In the transitional zone, the myelin responded to the injury simultaneously with the vascular damage in the same area. These changes in myelin structures may be further confirmed by electron microscopy (EM).

The loss of oligodendrocytes

To assess the changes in oligodendrocytes in the same dorsal white matter area, I counted the cell density of CC1^+ (APC) oligodendrocytes across the three regions (**Fig. 3.9**). In the epicenter, the oligodendrocytes immediately died at 0.5 hour post-injury and remained the same up to 7 day post-injury; in both the remote and transitional zone, the number of oligodendrocytes remained stable for the first 4 hours after injury, and then exhibited a drastic drop at 1 day which was maintained up to 7 day post-injury (**Fig. 3.9B-F, H**). The loss of oligodendrocytes also lags vascular disruption in the transitional zone.

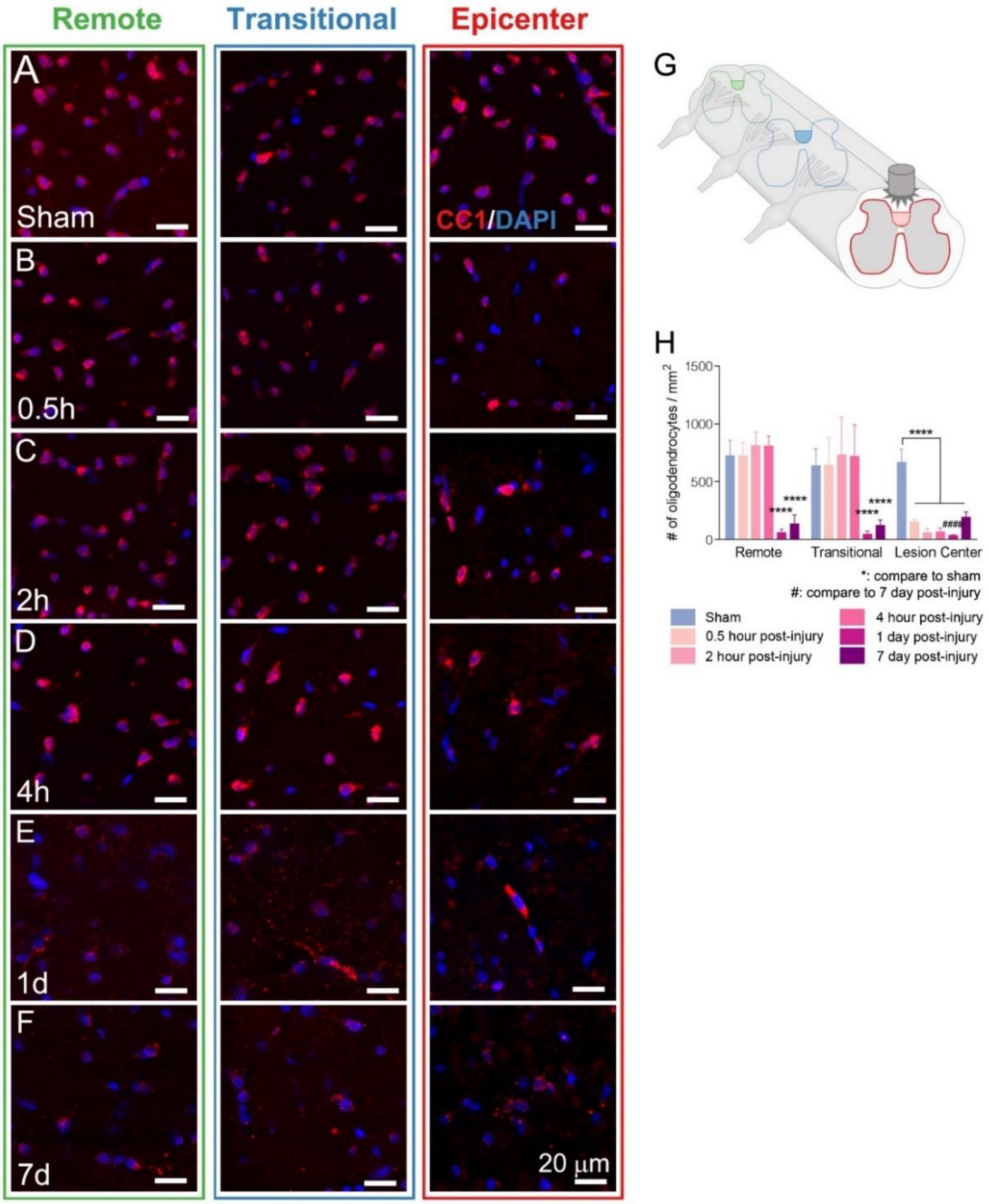

Figure 3.9. The loss of oligodendrocytes parallels the timescale for myelin response. (**A**) In 3 different regions (epicenter, transitional zone, and remote zone), quantification of oligodendrocyte density (double-labeled by CC-1 and DAPI) was counted in (**A**) Sham, (**B**) 0.5 hour, (**C**) 2 hour, (**D**) 4 hour, (**E**) 1 day, and (**F**) 7 day post-injury. (**G**) A schematic diagram showing the observed regions in the white matter. (**H**) Quantification of oligodendrocyte density per mm^2. Error bars represent ± SD. n=7 for sham, n=8 for 0.5h, 2h, and 4h post-injury group, n=6 for 1 day and 7 day post-injury group. * compared to sham control, # compared to 7 day post-injury. * or # $P<0.05$, ** *or* ## $P<0.01$, *** or ### $P<0.001$, **** or #### $P<0.0001$. Scale bars = 20 μm in (**A**-**F**).

Discussion

The goal of this study was to characterize a temporospatial map of the acute vascular responses correlated with neuronal changes and other cellular changes in three consecutive cord segments, rostral to the epicenter, following a contusive spinal cord injury. To date, few studies have examined the temporospatial profiles of contusive SCI at such acute time points, and to my knowledge, this is the first study to investigate the temporal relationship between vascular responses and neuronal damage.

Using a novel *in vivo* imaging method, I revealed the immediate appearance of injury-induced vasodilation and increased vascular permeability beyond the injury epicenter in living animals. Several vascular responses post-SCI were reported, including hemorrhage and loss of microvessels. An ultrastructural study reported arteriolar vasospasm at 24 hours after SCI (Anthes et al., 1996). However, my study provides the first direct evidence of SCI-induced vasodilation to date. Little information is available to understand its underlying mechanisms. According to the studies in autonomic dysreflexia, the one proposed mechanism is that SCI leads to the sudden loss of sympathetic regulation on the smooth muscle cells surrounding the blood vessel walls leading to the dilation of the vessels (Hagen et al., 2012). Vasodilation has been linked to nitric oxide (NO), which has a vascular relaxation effect on the smooth muscle cells (Waldman and Murad, 1988, Moncada and Higgs, 1993). Further investigations are required before vasodilation can be targeted for therapeutic interventions in an SCI model. One key question needs to be addressed first is whether post-injury vasodilation is detrimental or beneficial for the recovery of SCI. My finding of increased vascular permeability is consistent with the HRP tracing studies of Noble and Wrathall (Noble and Wrathall, 1988, Noble and Wrathall, 1989b). In addition, the range of immediate vascular leakage went beyond the injury site. Increased vascular permeability indicates the altered structure of the blood-spinal cord barrier (BSCB), leading to intraparenchymal hemorrhage and extravasation of the plasma protein. These early events of vascular disruption often coincide with tissue damage or cavity at a later time point. Targeting vascular disruption can serve for two purposes: a proof of concept that vascular damage contributes to tissue damage and the pursuit for neuroprotective treatments. The mechanisms underlying increased vascular permeability remain debatable. There are two pathways for substances to travel across the endothelial cell layer: paracellular and transcellular transport. The increased vascular permeability may be due to changes in either or both pathways. Targeting both pathways to repair the damaged vascular membrane and reestablish the normal BSCB can be a potential strategy.

Based on the temporal difference between the onset of the IgG leakage (30 min) and neuronal loss (1 day), I proposed a time window in the transitional zone that could be therapeutically relevant. At 2 hour post injury, I found these IgG$^+$ cells near the leaky vessels, which the morphology resembles neurons. Previous studies have indicated that the uptake of leaked IgG by neurons contributes to neuronal dysfunction following disruption of BBB (Michalak et al., 2012, Goasdoue et al., 2019, Johnson et al., 2018, Giris et al., 2017). Thus, this may further support the role of vascular damages in neuronal damage following SCI. A slight but not significant decrease of neuronal density in the remote zone at 1 day post-injury reflects there might be additional mechanisms responsible for the neuronal damages.

I detected microglial activation as early as 2 hour post-injury in the epicenter, shown as a morphological change from ramified to hypertrophied, up to 7 day post-injury.

The morphological changes of microglia, including retraction of processes and increased amoeboid morphology, often indicate inflammatory responses and/or phagocytotic features. The emergence of microglial response in the epicenter suggests a potential role of compromised BBB contributing to the activation of resident microglia, as demonstrated by *in vivo* two-photon microscopic studies (Nimmerjahn et al., 2005, Huber et al., 2016, Ju et al., 2018, Kozai et al., 2012). At 7 day post-injury, I also detected increased cell density. It can be attributed to the recruitment of monocyte-derived macrophages and/or proliferation. In both remote and transitional zones, I found a delayed activation starting at 1 day post-injury and increased cell density at 7 day post-injury. This different pattern of changes may be due to the injury severities received in these zones. Again, my results showed the microglial activation lags vascular leakage in the transitional zone, suggesting the role of vascular disruption in microglial activation of the non-direct injury area. Additionally, a previous study also suggested a potential molecular mechanism linking vascular disruption to microglial activation: BBB disruption exposed the parenchyma tissue to many blood-derived plasma proteins; One protein called fibrinogen binds to CD11b receptor of microglia, triggers increased expression of TNF-alpha, which switch resident microglia into a pro-inflammatory phenotype. The microglia-released TNF-alpha further showed neurotoxicity via ER stress signaling (Piers et al., 2018).

Similar to microglial activation, I also found reactive astrocytes starting at 2 hour post-injury in the epicenter, shown as elevated intensity of GFAP expression, up to 7 day post-injury. Again, this phenomenon occurred after vascular disruption. As one component of the neurovascular unit, it makes sense that astrocytes become quickly activated after the disruption of blood-CNS barrier. I also observed the enlarged size of astrocytes at 1 day post-injury and this continues to increase up to 7 day post-injury, suggesting further morphological changes which may contribute to the formation of the glial scar. The cell density of astrocytes first decreased at 4 hour post-injury, indicating cell loss in response to the injury. Then the cell density increased at 7 day post-injury, which is likely due to proliferation and/or cell migration from the uninjured area. In the transitional zone, the increased GFAP expression was at 4 hour post-injury and lasted up to 7 day post-injury. No sign of enlarged size or cell density was seen in this region. Although a much attenuated response, the activation of astrocytes still lags vascular disruption in the transitional zone. Unlike microglial response, no detection of reactive astrocytes was seen in the remote zone. The microglia likely have more motile responses compared to astrocytes.

For quantification of axons and myelin, I chose to evaluate the dorsal white matter area because it is where the axonal tracts reside (both ascending and descending) and receive a direct impact from the contusive injury. In the epicenter, the number of axons starting to decrease at 2 hour post-injury and the trend continued up to 7 day post-injury. The axonal loss here is most likely due to the direct mechanical injury. Meanwhile, the area of myelin and myelin area per axon showed an increase at 2 hour and 4 hour post-injury, followed by reducing back to sham level. An explanation of this data is that the myelin becomes swollen and disorganized loose structure as shown in enlarged area, and it may be fragmented and phagocytized by infiltrated macrophages resulted in the reduced area at 7 day post-injury. The axons also showed signs of swelling due to the significant increase in size at 7 day post-injury, which is consistent with previous reports on swollen axonal endings following SCI (Hill, 2017). In both transitional and remote zones, the number of axons started to decrease at 1 day post-injury and continued at 7 day post-injury.

The observed axons include both ascending and descending tracts. Previous studies in thoracic SCI transection models using tracer labeling show specific prolonged dieback of CST descending axons ranging from 2-3 mm (Hill et al., 2001, Seif et al., 2007). My results show a longer distance of axonal dieback ranging from 6-7.5 mm. This may be due to differences in three factors, including injury models, regional-specific axon vulnerability, and the combinational observation of both ascending and descending tracts in the lesioned region.

Previous studies found oligodendrocytes are extremely vulnerable to the toxic environment of acute SCI. Multiple factors could lead to oligodendrocyte loss, including excitotoxicity, oxidative stress, blood component, infiltrating neutrophils and activated microglia release product, etc (Almad et al., 2011). I observed an acute loss of oligodendrocytes as early as 0.5 hour post-injury in the epicenter, and this supports the conclusion from previous findings. And this loss persisted up to 7 day post-injury, showing no sign of replenishment of the oligodendrocytes either from proliferation or recruitment from elsewhere during the first week after injury. The early vascular disruption in the transitional zone may exert oxidative stress, which could contribute to the delayed loss of oligodendrocytes occurring at 7 day after injury. The microglial activation that occurred at 1 day post-injury may trigger the oligodendrocyte loss in the remote zone at 7 day post-injury, which may be mediated by nitric oxide (Merrill et al., 1993, Shuman et al., 1997, McTigue and Tripathi, 2008).

Taken together, my results indicate that vascular disruption occurs prior to neuronal loss in the transitional zone, suggesting a time window between these two phenomena. The findings bring up the possibility that vascular events could be a potential target to reduce the regional neuronal loss. To further address this hypothesis, additional studies need to be done to target acute vascular events, including intraparenchymal hemorrhage, blood-spinal cord barrier disruption, and blood protein extravasation. Not only could targeting these acute vascular events test the alternative underlying mechanism for secondary injury progression, but also it could provide potential targets for neuroprotection after SCI.

CHAPTER 4

TARGETING VASCULAR LEAKAGE WITH INTRAVENOUS DELIVERY OF FERULIC ACID (FA) - GLYCOL CHITOSAN (GC) NANOPARTICLES FOLLOWING SPINAL CORD INJURY

Hypothesis

The intravenous delivery of FA-GC, a nanoparticle encapsulated membrane sealant, can prevent or reduce progressive disrupted vascular changes, resulting in acute neuroprotection and long-term functional recovery after an acute SCI.

Introduction

My previous work demonstrated a time window between vascular dysfunction and neuronal damage in the transitional zone. To further investigate whether these early vascular damages contribute to the following neuronal damage, I need to identify feasible vascular targets. Previously detected acute vascular dysfunctions include vasodilation and increased vascular permeability. The physiological role of vasodilation following SCI remains elusive. Less effort has been spent on its involvement in neuronal damage. On the other hand, increased vascular permeability indicates the disruption of the blood-spinal cord barrier and the extravasation of all types of plasma proteins into the parenchymal tissue. Leaked plasma proteins include albumin, fibrinogen, fibronectin and immunoglobulin G, etc. Among them, a few studies reported the neurotoxicity of fibrinogen (Piers et al., 2018, Schachtrup et al., 2007, Ill-Raga et al., 2015). Thus, targeting vascular leakage is more likely to provide a neuroprotective effect following SCI. An attractive strategy to target vascular leakage is to reestablish the normal BSCB.

Previously, a colleague of mine reported a neuroprotective nanoparticle composed of ferulic acid (FA)-modified glycol chitosan (GC), represented by the acronym FA-GC, that accumulated at the lesion site and restored locomotor function following SCI (Wu et al., 2014) (**Fig. 4.1**). FA is a compound in the family of phenolic acids and is abundant in plant cell wall components (Mancuso and Santangelo, 2014). Chitosan, produced mainly from the exoskeleton of crustaceans, has been shown to achieve vascular hemostasis (Koksal et al., 2011, Gustafson et al., 2007, Brandenberg et al., 1984), decrease blood loss (Kunio et al., 2013), enhance angiogenesis (Zhou et al., 2013), promote endothelial repair (Zhao et al., 2013, Okamoto et al., 2002, Hoekstra et al., 1998, Esposito et al., 2013) in various animal models. Because chitosan is dissolved poorly in an aqueous solution with neutral pH, I employed a water-soluble GC derived from the primary amines in original chitosan (Na et al., 2012, Wu et al., 2014). Wu and his team found that FA-GC nanoparticles displayed a half-time of 20 hours retained in blood circulation and were only detected in the lesion site of the injured spinal cord (**Fig. 4.1C-D**). The packed red blood cells and blood clots were observed in the gray matter, demonstrating disruption of the blood vessels induced by the physical impact (**Fig. 4.1E**). To date, few studies reported chitosan-based therapy in the CNS (Brandenberg et al., 1984) and few, if any, delivered as a nanoparticle through iv. In my study, I decided to use the membrane sealant feature of FA-GC nanoparticles to seal the damaged vascular membrane. FA can also act as a strong antioxidative agent (Srinivasan et al., 2007) to protect vessels and neural tissue.

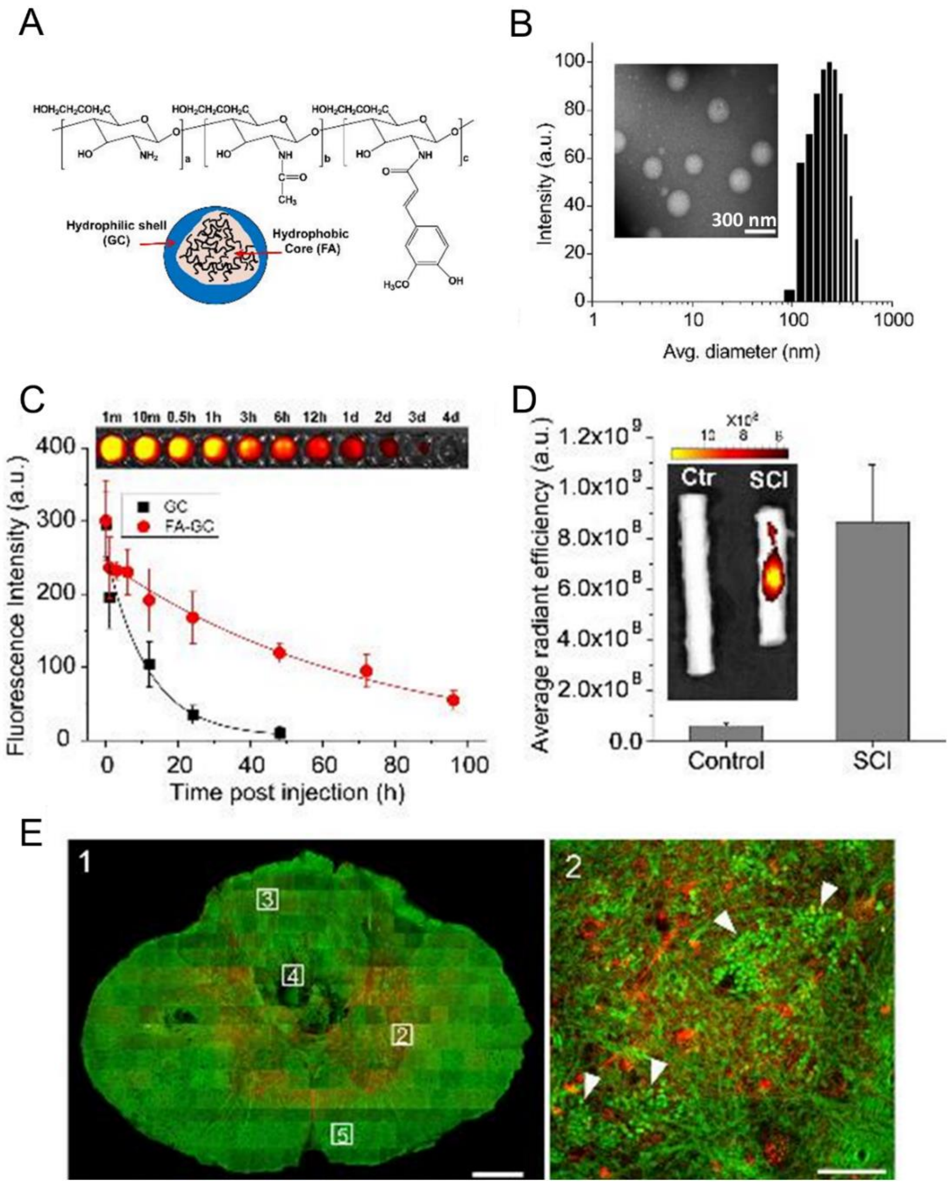

Figure 4.1. FA-GC nanoparticles exhibited long blood retention time and targeted delivery to injured spinal cord.

(A) Properties of FA-GC nanoparticles. **(B)** Size distribution and TEM image (scale bar: 300 nm). **(C)** Blood retention kinetics of FA-GC(-Cy5.5) and GC(-Cy5.5) in SCI rats. The fluorescence of FA-GC(-Cy5.5) in blood samples, drawn at different time points, were visualized (top). **(D)** Fluorescence imaging and quantification of FA-GC(-Cy5.5) in normal and injured spinal cords. **(E)** Distribution of FA-GC(-Cy5.5) in the injured spinal cord. A cross section through the injury epicenter shows the distribution of FA-GC (E1). Dotted squares represent high magnified images of the distribution of FA-GC (red) in the gray matter (E2). White arrowheads in E2 indicate packed red blood cells (Scale bar = 100 μm for E1 and 5 μm for E2). Adapted from (Wu et al., 2014).

My studies showed that an innovative nanoparticle, FA-GC, reduced the injury-induced vascular leakage, promoted region-specific neuroprotection and partial forelimb functional recovery when given within the 15 minutes following cervical contusion SCI in rats. Meanwhile, the effect of FA-GC provided a proof of concept that early vascular damages occurred in the transitional zone may contribute to later neuronal loss. The results of this study elucidate the potential benefits and shortcomings of targeting early vascular leakage using a nanoparticle with a membrane sealant effect in a clinically-relevant cervical contusive SCI model in rats.

Materials and methods

Animals

Six weeks old female Sprague-Dawley rats (180-220 g, Envigo RMS, Inc., Indianapolis, IN) were housed with an air filter in an environmentally-controlled facility with a 12-hour/12-hour light/dark cycle, and accessible to food and water freely throughout the entire study. In this study, a total of 42 rats were used and randomly assigned into 3 groups of experiments: *in vivo* spinal vascular imaging (n = 8), immunofluorescence labeling (n = 16), and forelimb functional assessments (n = 18). All procedures were approved by the Institutional Animal Care and Use Committee of Indiana University School of Medicine and Institutional Biosafety Committee and were strictly following the National Institutes of Health (NIH) Guide on humane care and the use of laboratory animals.

Spinal cord injury model

In preparation for surgery, the rats were injected with ketamine (87.7mg/kg) and xylazine (12.3mg/kg) mixture intraperitoneally to enter deep anesthesia. For all SCI performed in this study, the animals received a mild-to-moderate contusive injury at the midline of 7th cervical spinal cord segment (tissue displacement = 0.800mm) after laminectomy. The SCI was performed using a Louisville Injury System Apparatus (LISA) device according to a previously established protocol from Xu lab (Zhang et al., 2008).

In vivo spinal vascular imaging

This procedure was performed following the exact steps in the previous chapters. Also, the procedure was performed as previously described (Chen et al., 2017). In brief, two different fluorescein-conjugated dextran tracers (Rhodamine B isothiocyanate-dextran (Rho-dextran); Fluorescein isothiocyanate-dextran (FITC-dextran), 70kDa, Sigma-Aldrich, 4 mg/mL in saline) were intravenously given to anesthetized rats via EJV before and at 2 hours after SCI. Under 2P-LSM, Z-stack images across C5-C7 region (epicenter, transitional zone, remote zone) were taken to track dynamic changes in spinal blood vessels, including vessel diameter and vascular permeability. There were two groups in this experiment: FA-GC treatment (*n* =4; 5 mg/ml, 1ml) and saline control group (*n* =4). The parameters for the two-photon microscope followed the same settings in chapter 2 and 3.

Measurement of vessel diameter and vascular permeability

The acquired Z-stack images were analyzed via imageJ to measure changes in vessel diameter and vascular permeability. The images were first calibrated true to scale. For vessel diameter, a line is drawn perpendicular to the long axis of the vessel segment to measure the diameter. The diameter of the blood vessel is determined by the average of three measurements across the vessel segment. For vascular permeability, a probe of a 200 μm line is drawn both inside and outside the vessel to measure the fluorescence integrated density. The vascular permeability is calculated as the ratio of the outside value divided by the inside value.

Preparation and delivery of FA-GC nanoparticles in vivo

According to the work of Wu and colleagues, ferulic acid–glycol chitosan nanoparticles (FA-GC) were dissolved in 0.9% sodium chloride solution by sufficient sonication to produce a homogeneous solution of FA-GC nanoparticles (Wu et al., 2014). Each aliquot was 1 ml and prepared at the day of surgery. FA-GC (22.7mg/kg, 1ml in saline) were intravenously administrated to the SCI rats via the same EJV catheter previously used for tracer injection within 15 minutes post contusive injury.

Tissue processing for histological assessments

For the groups of animals for histological analysis, tissues were collected and processed adapting from a previous publication (Liu et al., 2006). At 0.5 hour, 2 hours, 4 hours, 1 day and 7 days after injury, anesthetized animals were transcardially perfused with 100 ml 0.01M phosphate buffer saline, followed by 400 ml of ice-cold 4% paraformaldehyde fixative solution in 0.01M PBS. A 9 mm segment of cervical cord including C5 to C7 was collected and post-fixed in the same fixative overnight, and then transferred to a solution of 30% sucrose in 1x PBS for 5 days. Spinal cord segments were embedded in O.C.T compound (Fisher, Waltham, MA) for cryostat sectioning. The tissues were cut on a cryostat (LeicaCM 1950; Buffalo Grove, IL) in a series of coronal 25-μm-thick sections from 5th to 7th cervical segments mounted on slides, and stored at -20°C. The sections were then processed for immunofluorescence labeling.

Immunofluorescence labeling

After the spinal cord sections were washed in 1xPBS three times at room temperature, blocked in 10% normal goat serum (NGS) or normal donkey serum (NDS) blocking solution (with 0.1% Triton X-100 in 1xPBS) for 1 hour, then incubated with primary antibodies in 5% NGS or NDS and Triton X-100 (0.05% in 1xPBS) at 4°C overnight. After washing in 1xPBS three times, sections were incubated with host-specific secondary antibodies for 1 hour at room temperature, followed by DAPI staining for 5 min. The sections were washed in 1xPBS again three times and coverslips were mounted with Fluoromount-G (SouthernBiotech, Birmingham, AL). The primary antibodies and their final dilutions were used as follows: anti-RECA1 (blood vessels; 1:200, mouse; Bio-Rad, Hercules, CA); anti-GFAP (astrocytes; 1:1000, chicken; Abcam, Cambridge, United Kingdom); anti-APC (oligodendrocytes; 1:400, mouse; Abcam); anti-Iba1 (microglia; 1:500, goat; Abcam); anti-ED1 (macrophages; 1:200, mouse; Abcam); anti-laminin (basement membrane of blood vessels; 1:200, rabbit; Millipore); anti-NeuN (neurons; 1:1000, mouse or rabbit; Millipore); anti-SMI31 (axons; 1:1000, mouse; Biolegend, San

Diego, CA); anti-MBP (myelin; 1:200, rat; Millipore). Secondary antibodies with either goat or donkey host were used in a dilution of 1:1000.

Fluorescence microscopy

For immunofluorescence labeling, an inverted fluorescent microscopy system (Zeiss Axiovert 200 M, Jena, Germany) was used to capture images. The microscope was combined with an apotome and interfaced with a digital camera (Zeiss Axio Cam MRc5) controlled by a computer. Images were captured using the apotome with software (AxioVision v4.8) and output as a cut view image. The images were later assembled and quantified in Photoshop CC (Adobe System, San Jose, CA).

Quantification of neuron

To quantify the number of surviving neurons, the spinal cord sections at 7 days post-injury (n = 8 for both groups; FA-GC treatment and saline control groups) were double labeled with primary antibody against NeuN and DAPI, followed by secondary antibodies. One side of the gray matter in the spinal cord was examined; cell density was calculated by dividing the total NeuN-positive number by the area of gray matter, and the average cell number per mm^2 was reported as total neuronal density. The gray matter area was further divided into three sub-regions based on the ten-layer Rexed laminae system: dorsal horn (lam I-VI), intermediate zone (lam VII), and ventral horn (lam VIII-IX) (Watson, 2009)(**Fig. 4.3B**). The neuron density in each sub-region was calculated the same as total neuronal density.

Forelimb behavioral assessments

Prior to all the following behavioral tests, the animals were habituated in the testing room for 30 minutes under consistent dimmed lighting conditions. During the first week following SCI, each test was evaluated every other day. From the second week to the sixth weeks following SCI, each test was assessed once a week.

Part I: adhesive removal

The somatosensory function of forelimbs was assessed according to a modified adhesive removal test for rats (Komotar et al., 2007). After the animal was placed in the testing cage, a piece of green paper tape (3.0 cm in length and 1.0 cm in width, standard laboratory tape) was wrapped around the forepaw with a consistent placement. The ends of the tape meet at the palm side, and the finger tips are slightly exposed from the tape-formed sleeves. Once the tape was attached successfully, the animal was placed back to the testing cage and two timers were started. The first timer recorded the time when the animals start attempts to remove the tape sleeves with either mouth or the other forelimb (contact time). The second timer recorded the time it takes for the rat to remove the entire tape (removal time). Both contact time and removal time were recorded as a single trial. The maximum duration for each trial lasts for 2 minutes. The left and right forelimb were alternatively tested, and five trials were performed for each limb. For each time point, both contact time and removal time were determined from averaging the best trial from the right and left limbs.

Part II: grid walking

Forelimb skilled motor coordination was evaluated using a grid walking test. The animals were tested on an elevated grid (124 x 120 cm^2, each grid size is 3.5 x 5.0 cm^2; height: 93 cm). Prior to every session, 70% ethanol and 10% bleach were used to clean the apparatus. Two cameras were set up to record travelled distance (activity camera) and footsteps (step camera), respectively. The activity camera was located directly above the grid to cover the entire grid frame. The step camera was posed at an angle of 20 – 40 degrees diagonally upwards. The tests were run by two examiners. To begin the test, one examiner placed the animal in the center of the grid, while the other examiner started both cameras and timer simultaneously. During a total testing period of 5 min, one examiner counted the total steps of each forelimb explored on the grid while the other examiner counted the number of foot drops for each forelimb. The percentage of foot fall (% Foot Fall) was calculated as the number of error steps divided by the number of total steps. Average of the two forelimbs were used as the final value. For travelled distance, the video recorded by the activity camera was analyzed using a behavioral tracking software named ANY-MAZE (Stoelting Co., Wood Dale, IL).

Part III: modified grip strength

A modified forelimb grip strength test was applied on a grip strength meter (TSE Systems, Inc., Chesterfield, MO) to assess skeletal muscle function according to a previous publication (Takeshita et al., 2017). A square metal frame with horizontal metal bars was connected to a high-precision force sensor. The metal frame was stably fixed on the metal stand vertically and the parallel metal bars were horizontally placed above the ground with a fixed height. Before each trial, the gauge was reset to 0. After placing the animal to grasp the same horizontal bar, the rat's tail was pulled by an examiner in a downward direction. As the rat pulls and releases the bar, the maximum force exerted was shown on the digital display of the force sensor as unit of pond (1 pond (P) = 0.0098 newton (N)). The criteria to validate a trial is that trials were excluded if only one forepaw, or the hindlimbs were involved; or the rat turned or left the bar without resistance during the test. At one-minute intervals, 10 consecutive measurements were performed on individuals and the average was reported as the grip strength. Given that the measurement can be influenced by the speed of the tail pull, the procedure was performed at a constant speed sufficiently slow to allow the rat to build up a resistance against it. The rat's body weight was measured after the test. To check if changes in body weight have a major effect on grip strength results, a Pearson correlation coefficient was analyzed between the body weight and the grip strength.

Part IV: rotarod

Motor performance of forelimbs was tested on rotarod with an accelerating mode (IITC Life Science Inc., Woodland Hills, CA; 4-40 rpm, 120 seconds cutoff time, top speed peaked at 90 seconds). The rotarod test was adapted to test on rats. The rats were placed on the rotarod to freely explore and both the latency and speed at fall were recorded. The animals were given five trials with an interval of 10 minutes between trials. Both latency and speed were reported as the average of three trials after eliminating the best and worst trials.

Statistical analysis

The data of *in vivo* diameter were analyzed using a one-way ANOVA of variance test followed by a Dunnett's multiple comparison test. The quantification of the neuron was presented as average ± standard deviation and analyzed using a one-way ANOVA of variance test followed by a Tukey post-hoc test. Behavior data were presented as average ± standard deviation and analyzed using unpaired t test at different time points. All analyses above are using GraphPad Prism 7 (GraphPad Software, Inc.; La Jolla, CA). *In vivo* permeability data were analyzed using repeated measure two-way ANOVA followed by LSD as post-hoc test via SPSS software IBM Corporation, Armonk, NY. All significance was set at $p < 0.05$.

Results

FA-GC reduced vascular leakage but did not affect changes in vessel diameter

I first injected FA-GC (22.7mg/kg, 1ml in saline) i.v. within 15 minutes after SCI, saline treatment as vehicle control. Two hours post-injury, *in vivo* spinal vascular imaging revealed changes in vessel diameter and vascular permeability compared to baseline (**Fig. 4.2A**). Similar to chapter 3, I observed the vascular changes across all three regions (**Fig. 4.2B,** epicenter, transitional zone, and remote zone). FA-GC treated animals had no significant changes of vessel diameter in any region compared to the saline-vehicle controls (**Fig. 4.2C-D**). On the other hand, the vascular leakage was significantly reduced in FA-GC treated animals across all three regions compared to saline controls (**Fig. 4.2C, E**). Here, I demonstrated the positive effect of FA-GC treatment on injury-induced vascular leakage *in vivo*.

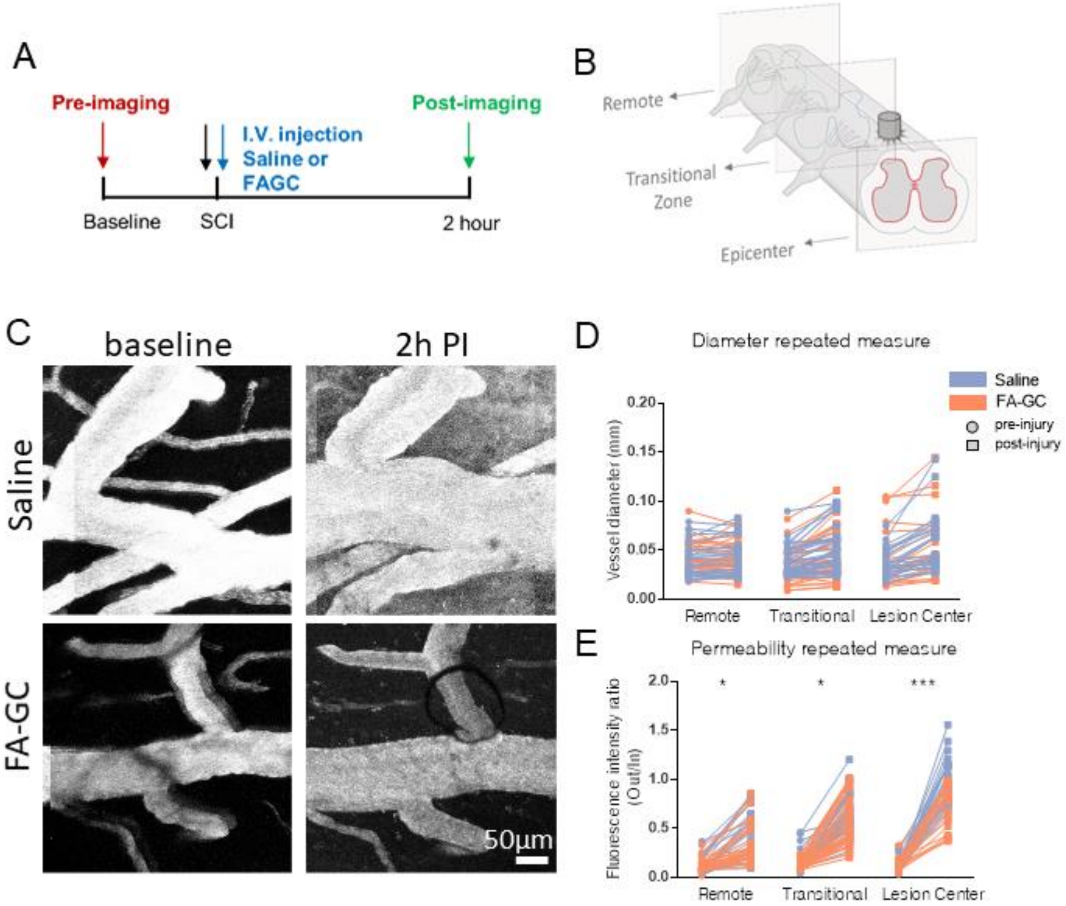

Figure 4.2. FA-GC reduces vascular leakage but has no effect on the vessel diameter following C7 contusion SCI.

(A) Experimental design and timeline. **(B)** Schematic drawing. **(C)** In vivo images at the transitional zone at baseline and 2 hour post-injury. The measurements of **(D)** vessel diameter and **(E)** vascular permeability. n=4 for both SCI + saline and SCI + FA-GC groups. * *P*<0.05, ** *P*<0.01, *** *P*<0.001.

FA-GC prevented neuronal loss of the ventral horn in the transitional zone

To assess whether FA-GC treatment prevented neuronal loss in the transitional zone following injury, immunofluorescence labeling of NeuN and DAPI was utilized. Since the previous chapter reported the neuronal loss in the transitional zone was seen at 1 day and 7 day post-injury, I observed the neuronal density in FA-GC treated or saline-treated animals at 7 day post-injury in all three regions (**Fig. 4.3A**). I first assessed the total neuronal density on one side of the gray matter. Considering the nonuniform distribution of the neurons in the gray matter, I also presented the neuronal density when divided into three subzones based on the laminae of Rexed: dorsal horn (lam I-VI), intermediate zone (lam VII), and ventral horn (lam VIII-IX) (Watson and Kayalioglu, 2009) (**Fig. 4.3B**). In all three regions, no difference was found in total neuronal density compared to saline controls (**Fig. 4.3C**). However, FA-GC treated animals had a significant increase of neuronal density in the ventral horn of transitional zone compared to its saline controls, while no significant differences were seen within the subzone of ventral horn in either epicenter or remote zone (**Fig. 4.3D**). In all three regions, no difference in neuronal density was observed in either the dorsal horn or intermediate zone (**Fig. 4.3E-F**). Although no rescue of neurons was seen in the lesion center, FA-GC treatment reduced neuronal loss from the ventral horn in the transitional zone.

The FA-GC treatment promoted partially improved forelimb motor function

To determine the functional efficacy of intravenously delivered FA-GC treatment, four different forelimb behavior assessments were evaluated: adhesive removal, grid walking, grip strength, and rotarod. The assessments were performed every other day for the first

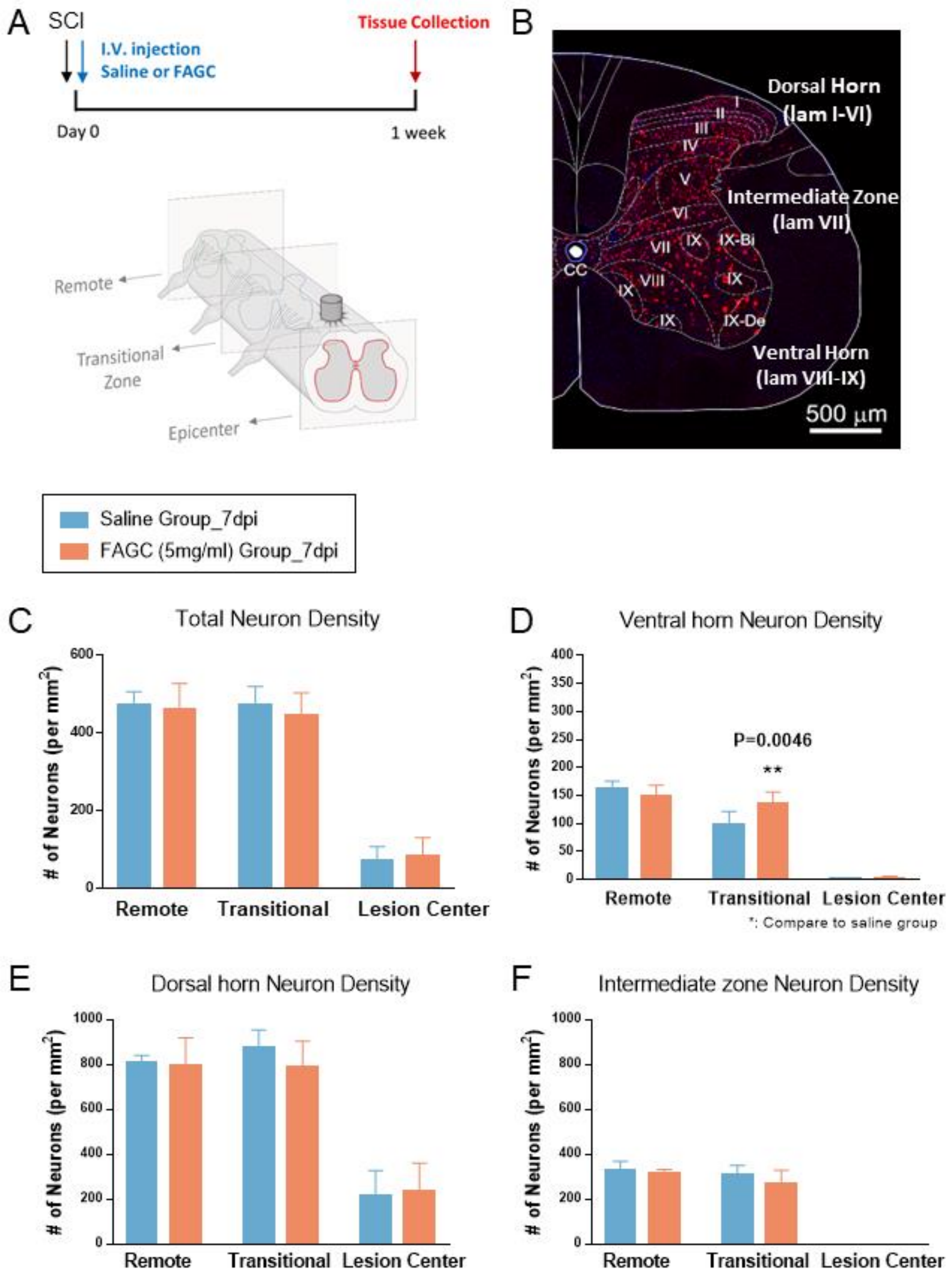

Figure 4.3. FA-GC prevented neuronal loss of the ventral horn in the transitional zone. **(A)** Experimental timeline and schematic drawing. **(B)** For quantification of neuronal density, the gray matter of spinal cord is divided into three sub-regions based on laminae: dorsal horn (lam I-VI), intermediate zone (lam VII), and ventral horn (lam VIII-IX). Quantification of neuronal density across three regions (remote, transitional, and lesion center) in **(C)** total, **(D)** ventral horn, **(E)** dorsal horn, and **(F)** intermediate zone. Error bars represent ± SD. n=8 for both SCI + saline and SCI + FA-GC groups. * $P<0.05$, ** $P<0.01$, *** $P<0.001$.

week post-injury, and once a week from the second week to the sixth weeks following SCI. As a new injury model, the C7 midline contusion SCI model was first evaluated using the abovementioned forelimb tests to demonstrate the sensitivity of the behavior tests, compared to sham controls. Then two other groups of animals were used to assess the functional differences between FA-GC treated animals and saline-vehicle controls (**Fig. 4.4**). Overall, FA-GC treatment promoted partial recovery of forelimb motor function, specifically shown in the grip strength test.

Part I: adhesive removal

Two parameters were assessed in this test: the latencies for contact or removal of the green tape. For contact latency, a slight but not significant deficit (p=0.062) was observed in SCI group at 1 day post-injury when compared to sham controls. Then the SCI animals showed a significant increase at 2 weeks post-injury when compared to sham controls (p=0.005). No other significant difference was seen in any other timepoint (**Fig. 4.5A**). For removal time, the test did not show any significant differences between SCI and sham controls until 4 weeks post-injury (p=0.002). No significant difference was seen at 5 weeks and 6 weeks post-injury (**Fig. 4.5B**).

In FA-GC treated animals, there was a slight but not significant increase of contact time at 3 days post-injury when compared to saline-treated animals (p=0.055). FA-GC treated animals did not show any significant improvement compared to saline-treated controls until 3 weeks post-injury (p=0.031). At 4 weeks post-injury, the trend of improvement was seen in the FA-GC treated animals but with no statistical significance.

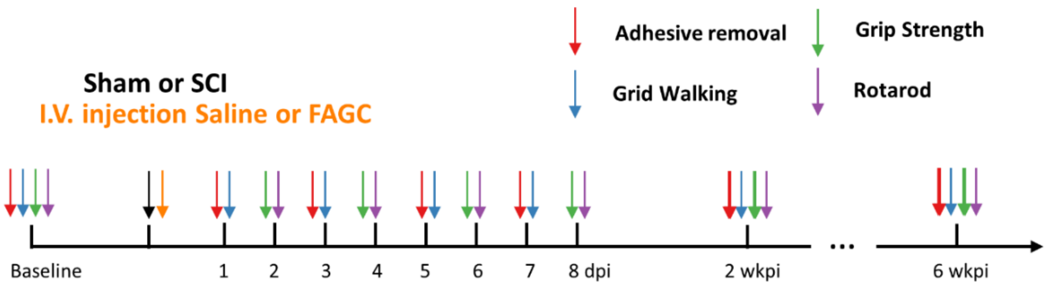

Figure 4.4. Experimental design and timeline for behavior assessments.

Four behavioral tests were used to assess forelimb functions: adhesive removal, grid walking, grip strength and rotarod. Four animal groups were included: Sham, SCI, SCI with i.v. injection of saline, and SCI with i.v. injection of FA-GC. Each test was evaluated every other day for the first week, and once a week from the second week to the sixth weeks following SCI.

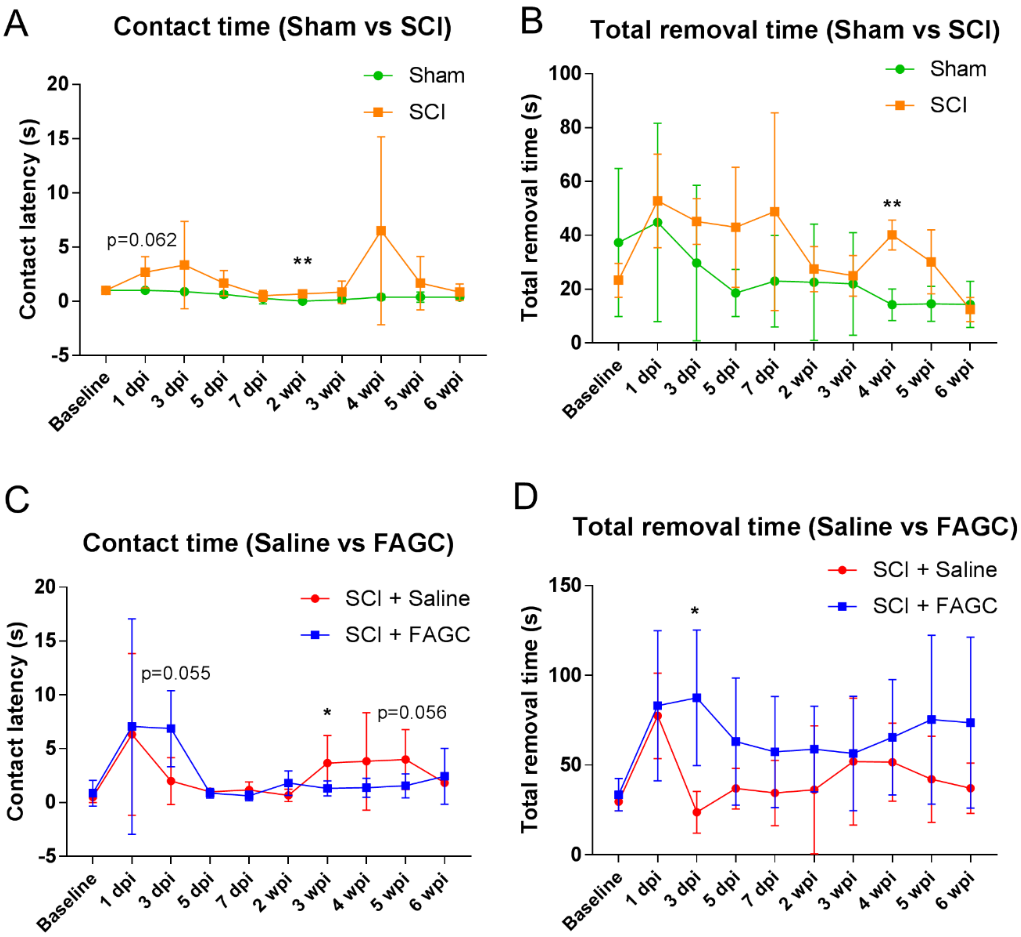

Figure 4.5. Adhesive removal test.
(A-B) Between Sham and SCI groups, both contact time and total removal time were recorded up to 6 weeks. **(C-D)** Between SCI + Saline and SCI + FA-GC groups, both contact time and total removal time were recorded up to 6 weeks. Error bars represent ± SD. n=4 for the sham group, n=3 for SCI and SCI + saline groups, and n=8 for SCI + FA-GC group. * *P*<0.05, ** *P*<0.01, *** *P*<0.001.

At 5 weeks post-injury, the trend maintained at a slight yet not significant level (p=0.056). At 6 weeks post-injury, no difference was seen between FA-GC-treated and saline-treated animals (**Fig. 4.5C**). For removal time, FA-GC treatment showed significant early deficit at 3 day post-injury (p=0.021), which matched with the difference in contact time at the same timepoint. However, no significant difference was seen at any other timepoint (**Fig. 4.5D**).

Part II: grid walking

Grid walking provided two parameters: percentage of foot fall (% foot fall) and total traveled distance (total distance). The % foot fall evaluates the accuracy of foot placement on the grid while walking, whereas the total distance represents the activity of the animals. For % foot fall, SCI animals showed significantly increased error starting at 1 day post-injury when compared to sham controls (SCI: 57.88% ± 15.67%, sham: 5.63% ± 1.21%, mean ± sem, p=0.011); this significant difference continued up to 7 day post-injury. At 2 weeks post-injury, no significant difference was observed. At 3 weeks post-injury, an attenuated trend was seen again (p=0.052). No significant difference was seen between SCI and sham groups from 4 weeks to 6 weeks post-injury (**Fig. 4.6A**). For total traveled distance, SCI animals showed a trend of decreased total distance at 3 days post-injury (p=0.064), followed by a significant difference at 5 days post-injury (p=0.003). From 7 days to 6 weeks post-injury, there was no significant difference between SCI and sham in the total traveled distance (**Fig. 4.6B**). These data indicated grid walking test could detect some early functional deficits induced by the C7 midline contusion SCI model.

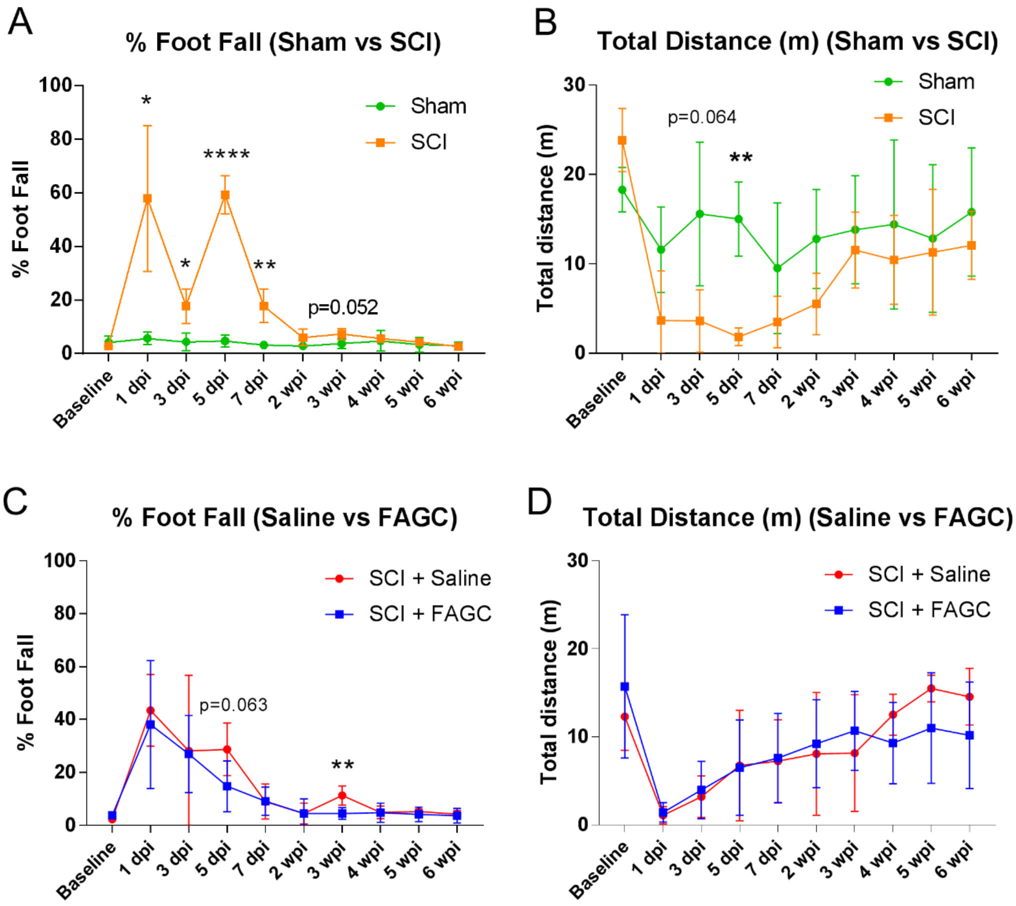

Figure 4.6. Grid walking.

(A-B) Between Sham and SCI groups, both percentages of foot fall and total distance travelled during grid walking were recorded up to 6 weeks. **(C-D)** Between SCI + Saline and SCI + FA-GC groups, both percentages of foot fall and total distance travelled during grid walking were recorded up to 6 weeks. Error bars represent ± SD. n=4 for the sham group, n=3 for SCI and SCI + saline groups, and n=8 for SCI + FA-GC group. * *P*<0.05, ** *P*<0.01, *** *P*<0.001.

No significant difference was found between FA-GC treated and saline-treated animals for the first three days post-injury. A slight but not significant improvement was seen in FA-GC treated animals at 5 days post-injury when compared to saline-treated controls ($p=0.063$). From 7 days to 6 weeks post-injury, no significant difference has been observed except at 3 weeks post-injury ($p=0.004$) (**Fig. 4.6C**). For total traveled distance, no significant difference was found at any particular timepoint (**Fig. 4.6D**). FA-GC treatment appeared to have no positive influence on the early functional deficits shown in the grid walking test.

Part III: modified grip strength

To test the muscular strength of forelimbs, the force of grip strength was evaluated. At 2 days post-injury, SCI induced a significant reduction in grip strength compared to sham controls ($p=0.0023$). This phenomenon was persistent up to 6 weeks post-injury (**Fig. 4.7A**). This result indicated grip strength was sensitive to distinguish the difference between SCI and sham controls.

At 2 days post-injury, both FA-GC and saline-treated SCI animals displayed SCI-induced reduction of grip strength compared to baseline (FA-GC: $p=<0.0001$; saline: $p=0.001$). FA-GC treated animals did not show any significant improvement in grip strength until 2 weeks post-injury when compared to saline controls ($p=0.0003$). At 3 weeks post-injury, FA-GC treated animals continuously showed significantly improved grip strength ($p=0.0008$). At 4 weeks post-injury, there was a continued trend of improvement in FA-GC treated group compared to saline controls ($p=0.08$). At 5 weeks post-injury, FA-GC treated animals again showed significantly improved grip strength ($p<$

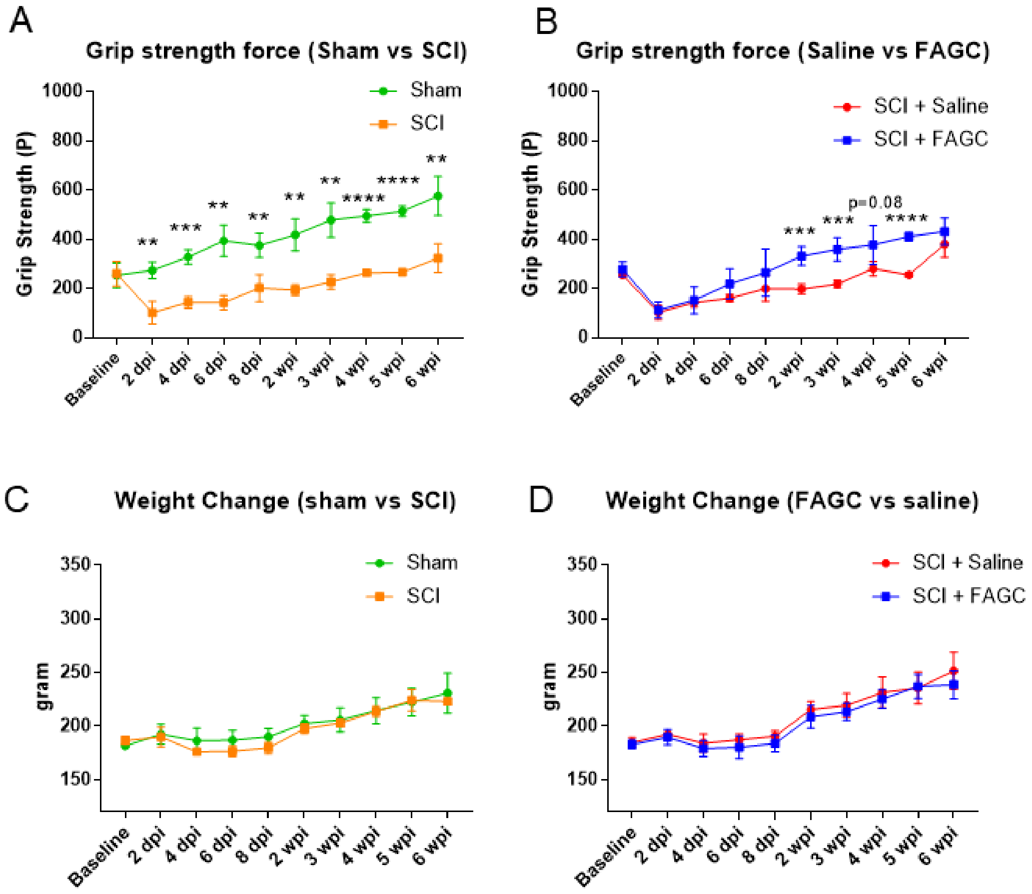

Figure 4.7. Modified grip strength.

The measurements of grip strength force were recorded up to 6 weeks **(A)** between Sham and SCI groups, and **(B)** between SCI + Saline and SCI + FA-GC groups. The changes of body weight were also recorded up to 6 weeks **(C)** between Sham and SCI groups, and **(D)** between SCI + Saline and SCI + FA-GC groups. Error bars represent ± SD. n=4 for the sham group, n=3 for SCI and SCI + saline groups, and n=8 for SCI + FA-GC group. * *P*<0.05, ** *P*<0.01, *** *P*<0.001, **** P<0.0001.

0.0001). No significant difference was observed at 6 weeks post-injury (**Fig. 4.7B**).

Interestingly, all four groups showed an ascending trend of grip strength over time. This phenomenon may be caused by two reasons: changes in body weight and the exercise effect brought by the repeated tests. Indeed, I found the body weight increased significantly over time (p<0.0001), but there was no significant difference in the ascending trend of neither sham vs. SCI groups (**Fig. 4.7C**, p=0.4568, p>0.05), nor FA-GC vs. saline-treated groups (**Fig. 4.7D**, p=0.2565, p>0.05).

Part IV: rotarod

Two parameters were assessed in the rotarod test: latency and speed when falling off the rod. For latency, both SCI animals and sham controls showed no significant difference at baseline (sham: 74.0 ± 6.3 sec, SCI: 75.7 ± 7.0 sec, mean ± sem, p=0.867). At 2 days post-injury, both SCI and sham groups had short latencies on the rod (Sham: 41.0 ± 14.1 sec, SCI: 3.7 ± 7.0 sec, mean ± sem, p=0.077). At 4 days post-injury, SCI animals spent significantly less time on the rod compared to sham controls (Sham: 47.5 ± 9.1 sec, SCI: 14.0 ± 5.0 sec, p=0.034). From 6 days to 6 weeks post-injury, no significant difference was observed between sham and SCI groups (**Fig. 4.8A**). The speed comparison between sham and SCI groups was very similar to the latency. At 2 days post-injury, a slight but not significant trend was shown (p=0.056). At 4 days post-injury, SCI animals showed significantly slower speed compared to sham controls (p=0.035). No significant difference was observed from 6 days to 6 weeks post-injury (**Fig. 4.8B**). Neither latency nor speed, FA-GC treated animals did not show any significant difference across all testing timepoints when compared to saline-vehicle (**Fig. 4.8C-D**).

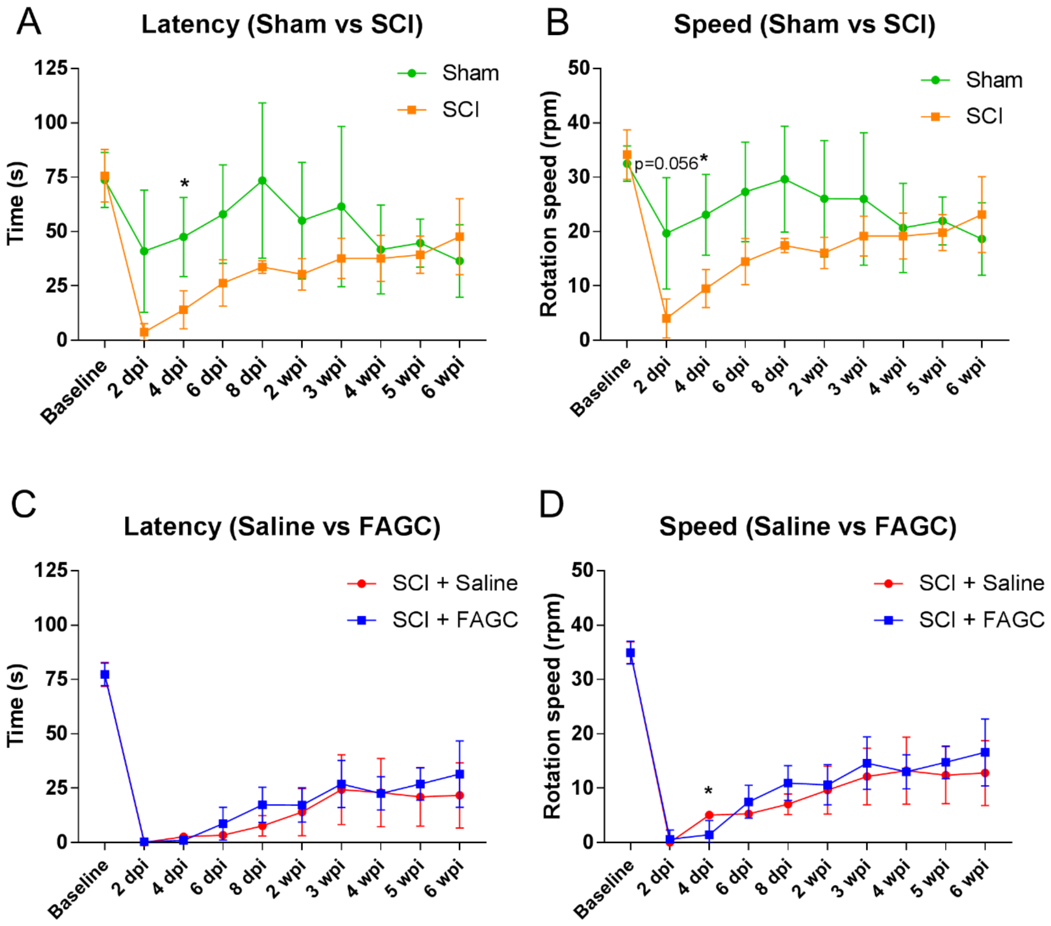

Figure 4.8. Rotarod.
(A-B) Between Sham and SCI groups, both latency and speed during rotarod were recorded up to 6 weeks. **(C-D)** Between SCI + Saline and SCI + FA-GC groups, both latency and speed during rotarod were recorded up to 6 weeks. Error bars represent ± SD. n=4 for the sham group, n=3 for SCI and SCI + saline groups, and n=8 for SCI + FA-GC group. * *P*<0.05.

Discussion

The intent of this study was to assess whether FA-GC can seal the damaged blood vessels following SCI. My results showed that intravenous delivery of FA-GC could effectively reduce the vascular leakage in the transitional zone, contributing to acute neuroprotection and partial recovery of forelimb functions. Although FA-GC was tested in a thoracic injury model and demonstrated a neuroprotective effect before (Wu et al., 2014), my current study does not simply replicate its effect at another cord level. Rather, I revealed a new mechanism of FA-GC action on the blockade of acute vascular damages. The results can also be a proof of concept that early vascular injuries from the transitional zone exacerbate secondary damage of the local neurons.

A novel vascular-based strategy treating SCI

My study is novel as it is using a nanoparticle to seal the damaged blood vessels treating SCI. Previous work attempted on targeting vascular mechanisms following SCI mostly focused on posttraumatic hypotension/ischemia. Their strategies involved whole-blood transfusion or administration of dopamine to raise the spinal cord blood flow, resulting in no functional improvement (Dolan and Tator, 1982). This may be due to the risk of ischemia-reperfusion injury. My work aimed to target increased vascular permeability, which put the spinal cord in risk exposing to the toxic effects of inflammatory cells. Both hemorrhage and plasma protein extravasation from the disrupted blood vessel are neurotoxic (Bell et al., 2012, Zhong et al., 2008). However, the underlying mechanisms of barrier disruption and vascular leakage contributing to neurotoxicity remain elusive. Thus, my study could provide more information and potentially a promising strategy.

FA-GC effectively reduced vascular leakage and prevented neuronal loss

Wu et al. previously demonstrated targeted distribution of FA-GC in the injured spinal cord using a fluorescent-tagged FA-GC (**Fig. 4.1E**) (Wu et al., 2014). Here I showed a positive effect of FA-GC on reducing SCI-induced vascular leakage *in vivo* (**Fig. 4.2**). This evidence collectively suggests that FA-GC can prevent vascular leakage by sealing the damaged vascular membrane. Although the previous study has shown a significant locomotion recovery with FA-GC treatment, its exact mechanism contributing to functional recovery remained obscure. My data provided strong circumstantial evidence of FA-GC on repairing the microvasculature.

Next, the histological evidence showed FA-GC reduced the loss of ventral horn neurons in the transitional zone (**Fig. 4.3**). Ferulic Acid (FA), a derivative of curcumin, exhibited neuroprotective effects via anti-oxidative, anti-apoptotic, and anti-excitotoxic effects in various animal models (Cheng et al., 2010, Sung et al., 2014, Lin et al., 2013). On the other hand, chitosan-based therapy has been shown to promote vascular hemostasis and decrease blood loss (Hoekstra et al., 1998, Esposito et al., 2013, Kunio et al., 2013). The significance of my study is that I demonstrated FA-GC could prevent neuronal loss from secondary degeneration under the dual properties of neuroprotection and hemostasis.

Behavior deficits of cervical spinal cord injury model and forelimb functional recovery of FA-GC treatment

Since I observed histological evidence of neuroprotection by FA-GC treatment, it was of my interest to assess whether this improvement translated into functional recovery. However, there was no characterization of the functional deficits in my cervical SCI model yet. Thus, I first established the baseline of behavioral deficits in this specific injury model. I chose to assess four behavioral tests, including grip strength, adhesive removal, grid walking, and rotarod. The grip strength is utilized to assess forelimb muscle strength (Takeshita et al., 2017), whereas the adhesive removal test is used to test somatosensory dysfunction (Komotar et al., 2007). Both rotarod and grid walking were chosen to test motor function and coordination of the forelimb/hindlimb function (Shiotsuki et al., 2010, Horvath et al., 2015). In the present study, a C7 midline contusive SCI model showed the main behavioral deficits in forelimb muscle strength. No significant difference was shown in somatosensory functional impairment. Only early deficit was observed in the motor coordination of the forelimb/hindlimb function.

In the FA-GC treated animals, my behavior data showed significant improvement of forelimb muscle strength over 6 weeks post-injury. This is consistent with my histological results that neurons in the ventral horn, mostly motor neurons, were saved with FA-GC treatment. A retrograde tracing study suggests that motor neurons in the lower cervical spinal cord innervate forelimb muscles, including biceps brachii, triceps brachii, and deltoid, etc (Bacskai et al., 2013). However, no significant difference was detected in the other three behavioral tests. It is possible that the sensitivity of these behavior measurements was not optimal for this specific injury model. On the other hand, another possibility is due to the lack of optimal drug concentration.

Future studies

Here my study on the effects of FA-GC treatment was only preliminary. To investigate the maximum effect of FA-GC on preventing post-injury vascular disruption, FA-GC was designed to be delivered within 15 minutes after SCI. Additional studies which deliver FA-GC at different time points after injury are required to explore a clinically feasible time window of delivery. Also, future studies will be performed to understand the mechanisms of FA-GC-mediated vascular permeability changes and repair. An *in vitro* Blood-Brain Barrier (BBB) model with a monolayer of human brain microvascular endothelial cells (HBMEC) has been successfully established. In this *in vitro* model, I can examine the barrier properties after injury and FA-GC treatment, including permeability and transendothelial electrical resistance (TEER). Using immunofluorescent staining and westernblot, I can also assess the structural and molecular changes in the endothelial cell layer. Several junctional proteins can be tested, such as occludin, claudin-6, vascular endothelial cadherin (VE-Cadherin), and F-actin.

In summary, the results of this study suggest that the intravenous delivery of FA-GC effectively improved the progressively disrupted vascular changes, promoted acute neuroprotective benefits and a partial role in long-term functional recovery after an acute SCI. Albeit additional studies will be needed to further address the mechanism and potential clinical applications of FA-GC, my results affirm FA-GC as an effective neuroprotective drug that can target microvasculature repair in the acute phase of SCI.

CHAPTER 5

CONCLUSIONS

Spinal cord injury (SCI) is a major public health issue in the United States and an unmet medical need. Nowadays, more than a quarter of a million Americans experience SCI (NSCISC, 2019). Unfortunately, there is no effective treatment available. It is well-known that a cascade of vascular events occurs immediately following spinal cord injury (SCI). However, the acute vascular dynamic changes and underlying mechanisms have been understudied.

One major reason impeding research in vascular injury following SCI is the technical limitation – most analyses have been performed on post-mortem samples and are unable to capture the dynamic changes of the vascular network under traumatic conditions. It is important to develop a tool that teases out the mechanism and contributes information to find potential targets for treatment. In chapter 2, I reported a two-dye in vivo imaging method, using two-photon laser scanning microscopy (TPLSM), which can overcome the technical barricades and monitor acute vascular dynamic changes following contusive SCI. This approach allows detecting blood flow and vessel diameter at various sites of the same rat pre- and post-injury, as well as other vascular pathology. Using this tool, my preliminary study found an unconventional phenomenon that SCI acutely induced an immediate vascular disruption which was beyond the direct impact site. This finding was different from the conventional concept on the progression of SCI, which facilitated my next study characterizing a temporospatial profile of vascular and cellular changes following SCI.

In the characterization study, I hypothesized that there is a “transitional zone” in the non-epicenter regions, where vascular disruptions occur before other cellular damages. To identify this “transitional zone”, I analyzed three regions of the cervical spinal cord at injury epicenter (C7), adjacent area (C6) and remote zone (C5). The definition of “transitional zone” is that the non-epicenter spinal cord region where immediate vascular damage occurs and no signs of other cellular changes yet. Therefore, the area of “transitional zone” can vary based on animal models and injury severity. My results first affirmed that vascular changes went beyond the direct injury site after SCI. Collectively my data suggest that vascular damage has occurred in the transitional zone before any other cellular responses to the injury, which indicates a time window to delay or rescue neuronal and axonal loss at the transitional zone. This is against the conventional view, which claims the secondary injury is a result of the expansion from the initial injured site. My conclusion is that there is a time window between vascular injury and cellular changes in the transitional zone. This leads me to consider the potential involvement of local vascular damages on secondary degeneration of cord tissue. In the present study, I only observed transitional and remote zones rostral to the injury. I anticipate that caudal representative regions may also present with similar changes. The rationale behind this prediction is that each spinal cord segment receives blood irrigation from the segmental spinal artery bidirectionally, not a simple rostral-to-caudal pattern of blood circulation. However, for the animal welfare purpose, I did not expose too long of the spinal cord segments. This prediction needs further experimental pieces of evidence for confirmation. As of now, I also could not differentiate if the cause of the secondary injury is either local degeneration or expansion from the injury epicenter at the late stage of injury. A third possibility is that both processes contribute to the secondary degeneration. By illustrating the phenomenon above, I may partially unveil an alternative hypothesis to explain the progression of secondary injuries after a contusive spinal cord injury. Also, targeting these early vascular responses and protecting vascular integrity at an acute phase of SCI could provide early neuronal protection and delay the expansion of damaged tissue in the spinal cord.

In the third study, I hypothesized that a nanoparticle called FA-GC could seal the leaking blood vessels and prevent further vascular leakage, thereby less secondary degeneration, and better functional recovery. My results showed the effects of FA-GC on the improvement of the vascular damages, which provided neuroprotective effects and functional recovery in forelimb muscle strength in a cervical SCI model. Thus, targeting acute vascular injury is a potent therapeutic strategy to prevent secondary degeneration and therefore to improve functional recovery.

Collectively, this work provides some initial hope in a new aspect of neuroprotection toward SCI, but still a lot of questions remain to be answered. Future studies will further dissect FA-GC's mechanism of action on microvasculature repair in *in vitro* BBB models. Besides, I can assess the vascular changes caudal to the injury. It is also of my interest to see whether it is the same as the rostral part or a completely different pattern of changes.

In summary, the current study developed a new method allowing me to be able to monitor/study in vivo dynamic vascular changes after SCI. It reveals potential vascular-based targets and a time window to prevent vascular injury-induced neuronal damage. It also tested a proof-of-concept strategy that targeting vascular leakage using a nanoparticle can reduce neuronal loss. Finally, this study sheds light onto the temporal window of acute

BSCB opening for effective drug delivery which is crucial to many current pharmaceutical clinical studies.

APPENDIX

Below is the statement regarding permission from journals to use my first-author published manuscripts in my thesis:

Part of content in chapter 2 was reused with permission from Journal of Visualized Experiments, published by MyJove Corp., Cambridge, MA.

REFERENCES

ABBOTT, N. J., PATABENDIGE, A. A., DOLMAN, D. E., YUSOF, S. R. & BEGLEY, D. J. 2010. Structure and function of the blood-brain barrier. *Neurobiol Dis,* 37**,** 13-25.

ABBOTT, N. J., RONNBACK, L. & HANSSON, E. 2006. Astrocyte-endothelial interactions at the blood-brain barrier. *Nat Rev Neurosci,* 7**,** 41-53.

AIRD, W. C. 2007. Phenotypic heterogeneity of the endothelium: II. Representative vascular beds. *Circ Res,* 100**,** 174-90.

AJAMI, B., BENNETT, J. L., KRIEGER, C., TETZLAFF, W. & ROSSI, F. M. 2007. Local self-renewal can sustain CNS microglia maintenance and function throughout adult life. *Nat Neurosci,* 10**,** 1538-43.

ALIZADEH, A., DYCK, S. M. & KARIMI-ABDOLREZAEE, S. 2019. Traumatic Spinal Cord Injury: An Overview of Pathophysiology, Models and Acute Injury Mechanisms. *Front Neurol,* 10**,** 282.

ALMAD, A., SAHINKAYA, F. R. & MCTIGUE, D. M. 2011. Oligodendrocyte fate after spinal cord injury. *Neurotherapeutics,* 8**,** 262-73.

ANDERSON, K. D., SHARP, K. G. & STEWARD, O. 2009. Bilateral cervical contusion spinal cord injury in rats. *Exp Neurol,* 220**,** 9-22.

ANTHES, D. L., THERIAULT, E. & TATOR, C. H. 1996. Ultrastructural evidence for arteriolar vasospasm after spinal cord trauma. *Neurosurgery,* 39**,** 804-14.

ANWAR, M. A., AL SHEHABI, T. S. & EID, A. H. 2016. Inflammogenesis of Secondary Spinal Cord Injury. *Front Cell Neurosci,* 10**,** 98.

ARMULIK, A., GENOVE, G. & BETSHOLTZ, C. 2011. Pericytes: developmental, physiological, and pathological perspectives, problems, and promises. *Dev Cell,* 21**,** 193-215.

ASANO, T. 1980. [Current trend in the research of cerebral microcirculation (author's transl)]. *Kokyu to junkan. Respiration & circulation,* 28**,** 339-345.

ATTWELL, D., BUCHAN, A. M., CHARPAK, S., LAURITZEN, M., MACVICAR, B. A. & NEWMAN, E. A. 2010. Glial and neuronal control of brain blood flow. *Nature,* 468**,** 232-43.

BACSKAI, T., FU, Y., SENGUL, G., RUSZNAK, Z., PAXINOS, G. & WATSON, C. 2013. Musculotopic organization of the motor neurons supplying forelimb and shoulder girdle muscles in the mouse. *Brain Struct Funct,* 218**,** 221-38.

BARGER, S. W., GOODWIN, M. E., PORTER, M. M. & BEGGS, M. L. 2007. Glutamate release from activated microglia requires the oxidative burst and lipid peroxidation. *Journal of Neurochemistry,* 101**,** 1205-1213.

BARTANUSZ, V., JEZOVA, D., ALAJAJIAN, B. & DIGICAYLIOGLU, M. 2011. The blood-spinal cord barrier: morphology and clinical implications. *Ann Neurol,* 70**,** 194-206.

BEATTIE, M. S., FAROOQUI, A. A. & BRESNAHAN, J. C. 2000. Review of current evidence for apoptosis after spinal cord injury. *J Neurotrauma,* 17**,** 915-25.

BEGGS, S., LIU, X. J., KWAN, C. & SALTER, M. W. 2010. Peripheral nerve injury and TRPV1-expressing primary afferent C-fibers cause opening of the blood-brain barrier. *Mol Pain,* 6**,** 74.

BELL, R. D., WINKLER, E. A., SINGH, I., SAGARE, A. P., DEANE, R., WU, Z., HOLTZMAN, D. M., BETSHOLTZ, C., ARMULIK, A., SALLSTROM, J., BERK, B. C. & ZLOKOVIC, B. V. 2012. Apolipoprotein E controls cerebrovascular integrity via cyclophilin A. *Nature,* 485**,** 512-6.

BENTON, R. L. & HAGG, T. 2011. Vascular Pathology as a Potential Therapeutic Target in SCI. *Transl Stroke Res,* 2**,** 556-74.

BENTON, R. L., MADDIE, M. A., DINCMAN, T. A., HAGG, T. & WHITTEMORE, S. R. 2009a. Transcriptional activation of endothelial cells by TGFbeta coincides with acute microvascular plasticity following focal spinal cord ischaemia/reperfusion injury. *ASN Neuro,* 1.

BENTON, R. L., MADDIE, M. A., GRUENTHAL, M. J., HAGG, T. & WHITTEMORE, S. R. 2009b. Neutralizing endogenous VEGF following traumatic spinal cord injury modulates microvascular plasticity but not tissue sparing or functional recovery. *Curr Neurovasc Res,* 6**,** 124-31.

BENTON, R. L., MADDIE, M. A., MINNILLO, D. R., HAGG, T. & WHITTEMORE, S. R. 2008. Griffonia simplicifolia isolectin B4 identifies a specific subpopulation of angiogenic blood vessels following contusive spinal cord injury in the adult mouse. *J Comp Neurol,* 507**,** 1031-52.

BRANDENBERG, G., LEIBROCK, L. G., SHUMAN, R., MALETTE, W. G. & QUIGLEY, H. 1984. Chitosan: a new topical hemostatic agent for diffuse capillary bleeding in brain tissue. *Neurosurgery,* 15**,** 9-13.

BRIGHTMAN, M. W. & REESE, T. S. 1969. Junctions between intimately apposed cell membranes in the vertebrate brain. *J Cell Biol,* 40**,** 648-77.

CASELLA, G. T., BUNGE, M. B. & WOOD, P. M. 2006. Endothelial cell loss is not a major cause of neuronal and glial cell death following contusion injury of the spinal cord. *Exp Neurol,* 202**,** 8-20.

CASELLA, G. T., MARCILLO, A., BUNGE, M. B. & WOOD, P. M. 2002. New vascular tissue rapidly replaces neural parenchyma and vessels destroyed by a contusion injury to the rat spinal cord. *Exp Neurol,* 173**,** 63-76.

CHEN, C., ZHANG, Y. P., SUN, Y., XIONG, W., SHIELDS, L. B. E., SHIELDS, C. B., JIN, X. & XU, X. M. 2017. An In Vivo Duo-color Method for Imaging Vascular Dynamics Following Contusive Spinal Cord Injury. *J Vis Exp,* 130**,** e56565.

CHENG, C.-Y., SU, S.-Y., TANG, N.-Y., HO, T.-Y., LO, W.-Y. & HSIEH, C.-L. 2010. Ferulic acid inhibits nitric oxide-induced apoptosis by enhancing GABAB1 receptor expression in transient focal cerebral ischemia in rats. *Acta Pharmacologica Sinica,* 31**,** 889.

CHERRY, J. D., OLSCHOWKA, J. A. & O'BANION, M. K. 2014. Neuroinflammation and M2 microglia: the good, the bad, and the inflamed. *J Neuroinflammation,* 11**,** 98.

COHEN, D. M., PATEL, C. B., AHOBILA-VAJJULA, P., SUNDBERG, L. M., CHACKO, T., LIU, S. J. & NARAYANA, P. A. 2009. Blood-spinal cord barrier permeability in experimental spinal cord injury: dynamic contrast-enhanced MRI. *NMR Biomed,* 22**,** 332-41.

COOMBER, B. L. & STEWART, P. A. 1985. Morphometric analysis of CNS microvascular endothelium. *Microvasc Res,* 30**,** 99-115.

CROWE, M. J., BRESNAHAN, J. C., SHUMAN, S. L., MASTERS, J. N. & BEATTIE, M. S. 1997. Apoptosis and delayed degeneration after spinal cord injury in rats and monkeys. *Nat Med,* 3**,** 73-76.

DANEMAN, R. 2012. The blood-brain barrier in health and disease. *Ann Neurol,* 72**,** 648-72.

DANEMAN, R. & PRAT, A. 2015. The blood-brain barrier. *Cold Spring Harb Perspect Biol,* 7**,** a020412.

DANEMAN, R., ZHOU, L., KEBEDE, A. A. & BARRES, B. A. 2010. Pericytes are required for blood-brain barrier integrity during embryogenesis. *Nature,* 468**,** 562-6.

DANIEL, P. M., LAM, D. K. & PRATT, O. E. 1981. Changes in the effectiveness of the blood-brain and blood-spinal cord barriers in experimental allergic encephalomyelitis. *J Neurol Sci,* 52**,** 211-9.

DAVALOS, D. & AKASSOGLOU, K. 2012. In vivo imaging of the mouse spinal cord using two-photon microscopy. *J Vis Exp***,** e2760.

DAVALOS, D., GRUTZENDLER, J., YANG, G., KIM, J. V., ZUO, Y., JUNG, S., LITTMAN, D. R., DUSTIN, M. L. & GAN, W. B. 2005. ATP mediates rapid microglial response to local brain injury in vivo. *Nat Neurosci,* 8**,** 752-8.

DAVALOS, D., LEE, J. K., SMITH, W. B., BRINKMAN, B., ELLISMAN, M. H., ZHENG, B. & AKASSOGLOU, K. 2008. Stable in vivo imaging of densely populated glia, axons and blood vessels in the mouse spinal cord using two-photon microscopy. *J Neurosci Methods,* 169**,** 1-7.

DAVALOS, D., RYU, J. K., MERLINI, M., BAETEN, K. M., LE MOAN, N., PETERSEN, M. A., DEERINCK, T. J., SMIRNOFF, D. S., BEDARD, C., HAKOZAKI, H., GONIAS MURRAY, S., LING, J. B., LASSMANN, H., DEGEN, J. L., ELLISMAN, M. H. & AKASSOGLOU, K. 2012. Fibrinogen-induced perivascular microglial clustering is required for the development of axonal damage in neuroinflammation. *Nat Commun,* 3**,** 1227.

DAVIS, E. J., FOSTER, T. D. & THOMAS, W. E. 1994. Cellular forms and functions of brain microglia. *Brain Res Bull,* 34**,** 73-8.

DEL ZOPPO, G. J., MILNER, R., MABUCHI, T., HUNG, S., WANG, X. & KOZIOL, J. A. 2006. Vascular matrix adhesion and the blood-brain barrier. *Biochem Soc Trans,* 34**,** 1261-6.

DOHRMANN, G. J. & ALLEN, W. E. 1975. Microcirculation of traumatized spinal cord. A correlation of microangiography and blood flow patterns in transitory and permanent paraplegia. *The Journal of trauma,* 15**,** 1003-1013.

DOLAN, E. J. & TATOR, C. H. 1982. The effect of blood transfusion, dopamine, and gamma hydroxybutyrate on posttraumatic ischemia of the spinal cord. *J Neurosurg,* 56**,** 350-8.

DREW, P. J., SHIH, A. Y. & KLEINFELD, D. 2011. Fluctuating and sensory-induced vasodynamics in rodent cortex extend arteriole capacity. *Proc Natl Acad Sci U S A,* 108**,** 8473-8.

DUMONT, R. J., OKONKWO, D. O., VERMA, S., HURLBERT, R. J., BOULOS, P. T., ELLEGALA, D. B. & DUMONT, A. S. 2001. Acute spinal cord injury, part I: pathophysiologic mechanisms. *Clin Neuropharmacol,* 24**,** 254-64.

DURAFOURT, B. A., MOORE, C. S., ZAMMIT, D. A., JOHNSON, T. A., ZAGUIA, F., GUIOT, M. C., BAR-OR, A. & ANTEL, J. P. 2012. Comparison of polarization properties of human adult microglia and blood-derived macrophages. *Glia,* 60**,** 717-27.

EGAWA, G., NAKAMIZO, S., NATSUAKI, Y., DOI, H., MIYACHI, Y. & KABASHIMA, K. 2013. Intravital analysis of vascular permeability in mice using two-photon microscopy. *Sci Rep,* 3**,** 1932.

ESPOSITO, G., ROSSI, F., MATTEINI, P., SCERRATI, A., PUCA, A., ALBANESE, A., ROSSI, G., RATTO, F., MAIRA, G. & PINI, R. 2013. In vivo laser assisted microvascular repair and end-to-end anastomosis by means of indocyanine green-infused chitosan patches: a pilot study. *Lasers Surg Med,* 45**,** 318-25.

EVANS, T. A., BARKAUSKAS, D. S., MYERS, J. T. & HUANG, A. Y. 2014. Intravital imaging of axonal interactions with microglia and macrophages in a mouse dorsal column crush injury. *J Vis Exp***,** e52228.

FAGRELL, B. & NILSSON, G. 1995. Advantages and Limitations of One-Point Laser Doppler Perfusion Monitoring in Clinical Practice. *Vascular Medicine Review,* vmr-6**,** 97-101.

FARRAR, M. J., BERNSTEIN, I. M., SCHLAFER, D. H., CLELAND, T. A., FETCHO, J. R. & SCHAFFER, C. B. 2012. Chronic in vivo imaging in the mouse spinal cord using an implanted chamber. *Nat Methods,* 9**,** 297-302.

FASSBENDER, J. M., WHITTEMORE, S. R. & HAGG, T. 2011. Targeting microvasculature for neuroprotection after SCI. *Neurotherapeutics,* 8**,** 240-51.

FIGLEY, S. A., KHOSRAVI, R., LEGASTO, J. M., TSENG, Y. F. & FEHLINGS, M. G. 2014. Characterization of vascular disruption and blood-spinal cord barrier permeability following traumatic spinal cord injury. *J Neurotrauma,* 31**,** 541-52.

GARBUZOVA-DAVIS, S., SAPORTA, S., HALLER, E., KOLOMEY, I., BENNETT, S. P., POTTER, H. & SANBERG, P. R. 2007. Evidence of compromised blood-spinal cord barrier in early and late symptomatic SOD1 mice modeling ALS. *PLoS One,* 2**,** e1205.

GINHOUX, F., GRETER, M., LEBOEUF, M., NANDI, S., SEE, P., GOKHAN, S., MEHLER, M. F., CONWAY, S. J., NG, L. G., STANLEY, E. R., SAMOKHVALOV, I. M. & MERAD, M. 2010. Fate mapping analysis reveals that adult microglia derive from primitive macrophages. *Science,* 330**,** 841-5.

GIRIS, M., BIRELLER, S., KUCUKALI, C. I., HANAGASI, H., DEGIRMENCIOGLU, S. & TUZUN, E. 2017. Impact of Neuro-Behcet Disease Immunoglobulin G on Neuronal Apoptosis. *Noro Psikiyatr Ars,* 54**,** 67-71.

GOASDOUE, K., CHAND, K. K., MILLER, S. M., LEE, K. M., COLDITZ, P. B., WIXEY, J. A. & BJORKMAN, S. T. 2019. Seizures Are Associated with Blood-Brain Barrier Disruption in a Piglet Model of Neonatal Hypoxic-Ischaemic Encephalopathy. *Dev Neurosci***,** 1-16.

GOODMAN, J. H., BINGHAM, W. G., JR. & HUNT, W. E. 1979. Platelet aggregation in experimental spinal cord injury. Ultrastructural observations. *Arch Neurol,* 36**,** 197-201.

GORDON, G. R., HOWARTH, C. & MACVICAR, B. A. 2011. Bidirectional control of arteriole diameter by astrocytes. *Exp Physiol,* 96**,** 393-9.

GRIESSENAUER, C. J., RABORN, J., FOREMAN, P., SHOJA, M. M., LOUKAS, M. & TUBBS, R. S. 2015. Venous drainage of the spine and spinal cord: a comprehensive review of its history, embryology, anatomy, physiology, and pathology. *Clin Anat,* 28**,** 75-87.

GRIFFITHS, I. R., BURNS, N. & CRAWFORD, A. R. 1978. Early vascular changes in the spinal grey matter following impact injury. *Acta Neuropathol,* 41**,** 33-9.

GUSTAFSON, S. B., FULKERSON, P., BILDFELL, R., AGUILERA, L. & HAZZARD, T. M. 2007. Chitosan dressing provides hemostasis in swine femoral arterial injury model. *Prehosp Emerg Care,* 11**,** 172-8.

HAGEN, E. M., REKAND, T., GRONNING, M. & FAERESTRAND, S. 2012. Cardiovascular complications of spinal cord injury. *Tidsskr Nor Laegeforen,* 132**,** 1115-20.

HALL, C. N., REYNELL, C., GESSLEIN, B., HAMILTON, N. B., MISHRA, A., SUTHERLAND, B. A., O'FARRELL, F. M., BUCHAN, A. M., LAURITZEN, M. & ATTWELL, D. 2014. Capillary pericytes regulate cerebral blood flow in health and disease. *Nature,* 508**,** 55-60.

HAWKINS, B. T. & DAVIS, T. P. 2005. The blood-brain barrier/neurovascular unit in health and disease. *Pharmacol Rev,* 57**,** 173-85.

HEMLEY, S. J., TU, J. & STOODLEY, M. A. 2009. Role of the blood-spinal cord barrier in posttraumatic syringomyelia. *J Neurosurg Spine,* 11**,** 696-704.

HICKEY, W. F. & KIMURA, H. 1988. Perivascular microglial cells of the CNS are bone marrow-derived and present antigen in vivo. *Science,* 239**,** 290-2.

HILL, C. E. 2017. A view from the ending: Axonal dieback and regeneration following SCI. *Neurosci Lett,* 652**,** 11-24.

HILL, C. E., BEATTIE, M. S. & BRESNAHAN, J. C. 2001. Degeneration and sprouting of identified descending supraspinal axons after contusive spinal cord injury in the rat. *Exp Neurol,* 171**,** 153-69.

HOEKSTRA, A., STRUSZCZYK, H. & KIVEKAS, O. 1998. Percutaneous microcrystalline chitosan application for sealing arterial puncture sites. *Biomaterials,* 19**,** 1467-71.

HORVATH, G., REGLODI, D., FARKAS, J., VADASZ, G., MAMMEL, B., KVARIK, T., BODZAI, G., KISS-ILLES, B., FARKAS, D., MATKOVITS, A., MANAVALAN, S., GASZNER, B., TAMAS, A. & KISS, P. 2015. Perinatal positive and negative influences on the early neurobehavioral reflex and motor development. *Adv Neurobiol,* 10**,** 149-67.

HUBER, B. R., MEABON, J. S., HOFFER, Z. S., ZHANG, J., HOEKSTRA, J. G., PAGULAYAN, K. F., MCMILLAN, P. J., MAYER, C. L., BANKS, W. A., KRAEMER, B. C., RASKIND, M. A., MCGAVERN, D. B., PESKIND, E. R. & COOK, D. G. 2016. Blast exposure causes dynamic microglial/macrophage responses and microdomains of brain microvessel dysfunction. *Neuroscience,* 319**,** 206-20.

HUDSON, L. C., BRAGG, D. C., TOMPKINS, M. B. & MEEKER, R. B. 2005. Astrocytes and microglia differentially regulate trafficking of lymphocyte subsets across brain endothelial cells. *Brain Res,* 1058**,** 148-60.

ILL-RAGA, G., PALOMER, E., RAMOS-FERNANDEZ, E., GUIX, F. X., BOSCH-MORATO, M., GUIVERNAU, B., TAJES, M., VALLS-COMAMALA, V.,

JIMENEZ-CONDE, J., OIS, A., PEREZ-ASENSIO, F., REYES-NAVARRO, M., CABALLO, C., GIL-GOMEZ, G., LOPEZ-VILCHEZ, I., GALAN, A. M., ALAMEDA, F., ESCOLAR, G., OPAZO, C., PLANAS, A. M., ROQUER, J., VALVERDE, M. A. & MUNOZ, F. J. 2015. Fibrinogen nitrotyrosination after ischemic stroke impairs thrombolysis and promotes neuronal death. *Biochim Biophys Acta,* 1852**,** 421-8.

JACOBS, T. P., KEMPSKI, O., MCKINLEY, D., DUTKA, A. J., HALLENBECK, J. M. & FEUERSTEIN, G. 1992. Blood flow and vascular permeability during motor dysfunction in a rabbit model of spinal cord ischemia. *Stroke,* 23**,** 367-73.

JANZER, R. C. & RAFF, M. C. 1987. Astrocytes induce blood-brain barrier properties in endothelial cells. *Nature,* 325**,** 253-7.

JOHNSON, V. E., WEBER, M. T., XIAO, R., CULLEN, D. K., MEANEY, D. F., STEWART, W. & SMITH, D. H. 2018. Mechanical disruption of the blood-brain barrier following experimental concussion. *Acta Neuropathol,* 135**,** 711-726.

JU, F., RAN, Y., ZHU, L., CHENG, X., GAO, H., XI, X., YANG, Z. & ZHANG, S. 2018. Increased BBB Permeability Enhances Activation of Microglia and Exacerbates Loss of Dendritic Spines After Transient Global Cerebral Ischemia. *Front Cell Neurosci,* 12**,** 236.

KIM, T. N., GOODWILL, P. W., CHEN, Y., CONOLLY, S. M., SCHAFFER, C. B., LIEPMANN, D. & WANG, R. A. 2012. Line-scanning particle image velocimetry: an optical approach for quantifying a wide range of blood flow speeds in live animals. *PLoS One,* 7**,** e38590.

KOBRINE, A. I., DOYLE, T. F. & MARTINS, A. N. 1974. Spinal cord blood flow in the rhesus monkey by the hydrogen clearance method. *Surg Neurol,* 2**,** 197-200.

KOKSAL, O., OZDEMIR, F., CAM ETOZ, B., ISBIL BUYUKCOSKUN, N. & SIGIRLI, D. 2011. Hemostatic effect of a chitosan linear polymer (Celox(R)) in a severe femoral artery bleeding rat model under hypothermia or warfarin therapy. *Ulus Travma Acil Cerrahi Derg,* 17**,** 199-204.

KOMOTAR, R. J., KIM, G. H., SUGHRUE, M. E., OTTEN, M. L., RYNKOWSKI, M. A., KELLNER, C. P., HAHN, D. K., MERKOW, M. B., GARRETT, M. C., STARKE, R. M. & CONNOLLY, E. S. 2007. Neurologic assessment of somatosensory dysfunction following an experimental rodent model of cerebral ischemia. *Nat Protoc,* 2**,** 2345-7.

KOYANAGI, I., TATOR, C. H. & LEA, P. J. 1993a. Three-dimensional analysis of the vascular system in the rat spinal cord with scanning electron microscopy of vascular corrosion casts. Part 2: Acute spinal cord injury. *Neurosurgery,* 33**,** 285-91; discussion 292.

KOYANAGI, I., TATOR, C. H. & THERIAULT, E. 1993b. Silicone rubber microangiography of acute spinal cord injury in the rat. *Neurosurgery,* 32**,** 260-8; discussion 268.

KOZAI, T. D., VAZQUEZ, A. L., WEAVER, C. L., KIM, S. G. & CUI, X. T. 2012. In vivo two-photon microscopy reveals immediate microglial reaction to implantation of microelectrode through extension of processes. *J Neural Eng,* 9**,** 066001.

KRISHNA, V., ANDREWS, H., JIN, X., YU, J., VARMA, A., WEN, X. & KINDY, M. 2013. A contusion model of severe spinal cord injury in rats. *J Vis Exp*.

KULKARNI, M. V., MCARDLE, C. B., KOPANICKY, D., MINER, M., COTLER, H. B., LEE, K. F. & HARRIS, J. H. 1987. Acute spinal cord injury: MR imaging at 1.5 T. *Radiology,* 164**,** 837-43.

KUNIO, N. R., RIHA, G. M., WATSON, K. M., DIFFERDING, J. A., SCHREIBER, M. A. & WATTERS, J. M. 2013. Chitosan based advanced hemostatic dressing is associated with decreased blood loss in a swine uncontrolled hemorrhage model. *Am J Surg,* 205**,** 505-10.

LASJAUNIAS, P. & A., B. 1990. Spinal and spinal cord arteries and veins. *Surgical Neuroangiography: Functional Vascular Anatomy of Brain, Spinal Cord, and Spine.* New York: Springer-Verlag.

LEPORE, A. C. 2011. Intraspinal cell transplantation for targeting cervical ventral horn in amyotrophic lateral sclerosis and traumatic spinal cord injury. *J Vis Exp*.

LI, W. L., YU, S. P., CHEN, D., YU, S. S., JIANG, Y. J., GENETTA, T. & WEI, L. 2013. The regulatory role of NF-kappaB in autophagy-like cell death after focal cerebral ischemia in mice. *Neuroscience,* 244**,** 16-30.

LI, X. G., LIN, X. J., DU, J. H., XU, S. Z., LOU, X. F. & CHEN, Z. 2016. Combination of methylprednisolone and rosiglitazone promotes recovery of neurological function after spinal cord injury. *Neural Regen Res,* 11**,** 1678-1684.

LI, Y. Q., CHEN, P., JAIN, V., REILLY, R. M. & WONG, C. S. 2004. Early radiation-induced endothelial cell loss and blood-spinal cord barrier breakdown in the rat spinal cord. *Radiat Res,* 161**,** 143-52.

LIN, T. Y., LU, C. W., HUANG, S. K. & WANG, S. J. 2013. Ferulic acid suppresses glutamate release through inhibition of voltage-dependent calcium entry in rat cerebrocortical nerve terminals. *J Med Food,* 16**,** 112-9.

LIU, N. K. & XU, X. M. 2012. Neuroprotection and its molecular mechanism following spinal cord injury. *Neural Regen Res,* 7**,** 2051-62.

LIU, N. K., ZHANG, Y. P., TITSWORTH, W. L., JIANG, X., HAN, S., LU, P. H., SHIELDS, C. B. & XU, X. M. 2006. A novel role of phospholipase A2 in mediating spinal cord secondary injury. *Ann Neurol,* 59**,** 606-19.

LIU, X. Z., XU, X. M., HU, R., DU, C., MCDONALD, J. W., DONG, H. X., WU, Y. J., FAN, G. S., JACQUIN, M. F., HSU, C. Y. & CHOI, D. W. 1997. Neuronal and glial apoptosis after traumatic spinal cord injury. *J Neurosci,* 17**,** 5395-5406.

LOSCHER, W. & POTSCHKA, H. 2005. Blood-brain barrier active efflux transporters: ATP-binding cassette gene family. *NeuroRx,* 2**,** 86-98.

LOSEY, P. & ANTHONY, D. C. 2014. Impact of vasculature damage on the outcome of spinal cord injury: a novel collagenase-induced model may give new insights into the mechanisms involved. *Neural Regen Res,* 9**,** 1783-6.

LOY, D. N., CRAWFORD, C. H., DARNALL, J. B., BURKE, D. A., ONIFER, S. M. & WHITTEMORE, S. R. 2002. Temporal progression of angiogenesis and basal lamina deposition after contusive spinal cord injury in the adult rat. *J Comp Neurol,* 445**,** 308-24.

MAIKOS, J. T. & SHREIBER, D. I. 2007. Immediate damage to the blood-spinal cord barrier due to mechanical trauma. *J Neurotrauma,* 24**,** 492-507.

MANCUSO, C. & SANTANGELO, R. 2014. Ferulic acid: pharmacological and toxicological aspects. *Food Chem Toxicol,* 65**,** 185-95.

MANTOVANI, A., SICA, A., SOZZANI, S., ALLAVENA, P., VECCHI, A. & LOCATI, M. 2004. The chemokine system in diverse forms of macrophage activation and polarization. *Trends Immunol,* 25**,** 677-86.

MATSUI, T., SVENSSON, C. I., HIRATA, Y., MIZOBATA, K., HUA, X. Y. & YAKSH, T. L. 2010. Release of prostaglandin E(2) and nitric oxide from spinal microglia is dependent on activation of p38 mitogen-activated protein kinase. *Anesth Analg,* 111**,** 554-60.

MAUTES, A. E., WEINZIERL, M. R., DONOVAN, F. & NOBLE, L. J. 2000. Vascular events after spinal cord injury: contribution to secondary pathogenesis. *Phys Ther,* 80**,** 673-87.

MAZENSKY, D., DANKO, J., PETROVOVA, E., FLESAROVA, S., SUPUKA, P., SUPUKOVA, A., LUPTAKOVA, L. & PURZYC, H. 2015. Anatomical study of blood supply to the cervical spinal cord in the guinea pig. *Anim Sci J,* 86**,** 641-5.

MAZENSKY, D., FLESAROVA, S. & SULLA, I. 2017. Arterial Blood Supply to the Spinal Cord in Animal Models of Spinal Cord Injury. A Review. *Anat Rec (Hoboken),* 300**,** 2091-2106.

MCTIGUE, D. M. & TRIPATHI, R. B. 2008. The life, death, and replacement of oligodendrocytes in the adult CNS. *Journal of Neurochemistry,* 107**,** 1-19.

MERRILL, J. E., IGNARRO, L. J., SHERMAN, M. P., MELINEK, J. & LANE, T. E. 1993. Microglial cell cytotoxicity of oligodendrocytes is mediated through nitric oxide. *J Immunol,* 151**,** 2132-41.

MICHALAK, Z., LEBRUN, A., DI MICELI, M., ROUSSET, M. C., CRESPEL, A., COUBES, P., HENSHALL, D. C., LERNER-NATOLI, M. & RIGAU, V. 2012. IgG leakage may contribute to neuronal dysfunction in drug-refractory epilepsies with blood-brain barrier disruption. *J Neuropathol Exp Neurol,* 71**,** 826-38.

MITTAPALLI, R. K., MANDA, V. K., ADKINS, C. E., GELDENHUYS, W. J. & LOCKMAN, P. R. 2010. Exploiting nutrient transporters at the blood-brain barrier to improve brain distribution of small molecules. *Ther Deliv,* 1**,** 775-84.

MOES, P. & MAILLOT, C. 1981. [Superficial veins of the human spinal cord. An attempt at classification]. *Arch Anat Histol Embryol,* 64**,** 5-110.

MONCADA, S. & HIGGS, A. 1993. The L-arginine-nitric oxide pathway. *N Engl J Med,* 329**,** 2002-12.

NA, J. H., LEE, S. Y., LEE, S., KOO, H., MIN, K. H., JEONG, S. Y., YUK, S. H., KIM, K. & KWON, I. C. 2012. Effect of the stability and deformability of self-assembled glycol chitosan nanoparticles on tumor-targeting efficiency. *J Control Release,* 163**,** 2-9.

NAKA, Y., ITAKURA, T., NAKAI, K., NAKAKITA, K., IMAI, H., OKUNO, T., KAMEI, I. & KOMAI, N. 1987. Microangioarchitecture of the feline spinal cord. Three-dimensional observation of blood vessel corrosion casts by scanning electron microscopy. *J Neurosurg,* 66**,** 447-52.

NELSON, E., GERTZ, S. D., RENNELS, M. L., DUCKER, T. B. & BLAUMANIS, O. R. 1977. Spinal cord injury. The role of vascular damage in the pathogenesis of central hemorrhagic necrosis. *Arch Neurol,* 34**,** 332-3.

NESIC, O., LEE, J., YE, Z., UNABIA, G. C., RAFATI, D., HULSEBOSCH, C. E. & PEREZ-POLO, J. R. 2006. Acute and chronic changes in aquaporin 4 expression after spinal cord injury. *Neuroscience,* 143**,** 779-92.

NIMMERJAHN, A., KIRCHHOFF, F. & HELMCHEN, F. 2005. Resting microglial cells are highly dynamic surveillants of brain parenchyma in vivo. *Science,* 308**,** 1314-8.

NOBLE, L. J. & WRATHALL, J. R. 1985. Spinal cord contusion in the rat: morphometric analyses of alterations in the spinal cord. *Exp Neurol,* 88**,** 135-49.

NOBLE, L. J. & WRATHALL, J. R. 1988. Blood-spinal cord barrier disruption proximal to a spinal cord transection in the rat: time course and pathways associated with protein leakage. *Exp Neurol,* 99**,** 567-78.

NOBLE, L. J. & WRATHALL, J. R. 1989a. Correlative analyses of lesion development and functional status after graded spinal cord contusive injuries in the rat. *Exp Neurol,* 103**,** 34-40.

NOBLE, L. J. & WRATHALL, J. R. 1989b. Distribution and time course of protein extravasation in the rat spinal cord after contusive injury. *Brain Res,* 482**,** 57-66.

NOELL, S., WOLBURG-BUCHHOLZ, K., MACK, A. F., BEEDLE, A. M., SATZ, J. S., CAMPBELL, K. P., WOLBURG, H. & FALLIER-BECKER, P. 2011. Evidence for a role of dystroglycan regulating the membrane architecture of astroglial endfeet. *Eur J Neurosci,* 33**,** 2179-86.

NSCISC 2019. Facts and Figures at a Glance.

OKAMOTO, Y., WATANABE, M., MIYATAKE, K., MORIMOTO, M., SHIGEMASA, Y. & MINAMI, S. 2002. Effects of chitin/chitosan and their oligomers/monomers on migrations of fibroblasts and vascular endothelium. *Biomaterials,* 23**,** 1975-9.

OLDENDORF, W. H., CORNFORD, M. E. & BROWN, W. J. 1977. The large apparent work capability of the blood-brain barrier: a study of the mitochondrial content of capillary endothelial cells in brain and other tissues of the rat. *Ann Neurol,* 1**,** 409-17.

ONIFER, S. M., RABCHEVSKY, A. G. & SCHEFF, S. W. 2007a. Rat models of traumatic spinal cord injury to assess motor recovery. *ILAR J,* 48**,** 385-95.

ONIFER, S. M., RABCHEVSKY, A. G. & SCHEFF, S. W. 2007b. Rat models of traumatic spinal cord injury to assess motor recovery. *ILAR J.*

PAN, J. Z., NI, L., SODHI, A., AGUANNO, A., YOUNG, W. & HART, R. P. 2002. Cytokine activity contributes to induction of inflammatory cytokine mRNAs in spinal cord following contusion. *J Neurosci Res,* 68**,** 315-22.

PAN, W., BANKS, W. A. & KASTIN, A. J. 1997. Permeability of the blood-brain and blood-spinal cord barriers to interferons. *J Neuroimmunol,* 76**,** 105-11.

PEPPIATT, C. M., HOWARTH, C., MOBBS, P. & ATTWELL, D. 2006. Bidirectional control of CNS capillary diameter by pericytes. *Nature,* 443**,** 700-4.

PERSIDSKY, Y., GHORPADE, A., RASMUSSEN, J., LIMOGES, J., LIU, X. J., STINS, M., FIALA, M., WAY, D., KIM, K. S., WITTE, M. H., WEINAND, M., CARHART, L. & GENDELMAN, H. E. 1999. Microglial and astrocyte chemokines regulate monocyte migration through the blood-brain barrier in human immunodeficiency virus-1 encephalitis. *Am J Pathol,* 155**,** 1599-611.

PIERS, T. M., EAST, E., VILLEGAS-LLERENA, C., SEVASTOU, I. G., MATARIN, M., HARDY, J. & POCOCK, J. M. 2018. Soluble Fibrinogen Triggers Non-cell Autonomous ER Stress-Mediated Microglial-Induced Neurotoxicity. *Front Cell Neurosci,* 12**,** 404.

PINEAU, I. & LACROIX, S. 2007. Proinflammatory cytokine synthesis in the injured mouse spinal cord: multiphasic expression pattern and identification of the cell types involved. *J Comp Neurol,* 500**,** 267-85.

POLFLIET, M. M., ZWIJNENBURG, P. J., VAN FURTH, A. M., VAN DER POLL, T., DOPP, E. A., RENARDEL DE LAVALETTE, C., VAN KESTEREN-HENDRIKX, E. M., VAN ROOIJEN, N., DIJKSTRA, C. D. & VAN DEN BERG, T. K. 2001. Meningeal and perivascular macrophages of the central nervous system play a protective role during bacterial meningitis. *J Immunol,* 167**,** 4644-50.

POPOVICH, P. G. & JONES, T. B. 2003. Manipulating neuroinflammatory reactions in the injured spinal cord: back to basics. *TIPS,* 24**,** 13-17.

PROCKOP, L. D., NAIDU, K. A., BINARD, J. E. & RANSOHOFF, J. 1995. Selective permeability of [3H]-D-mannitol and [14C]-carboxyl-inulin across the blood-brain barrier and blood-spinal cord barrier in the rabbit. *J Spinal Cord Med,* 18**,** 221-6.

REESE, T. S. & KARNOVSKY, M. J. 1967. Fine structural localization of a blood-brain barrier to exogenous peroxidase. *J Cell Biol,* 34**,** 207-17.

RIVLIN, A. S. & TATOR, C. H. 1978. Regional spinal cord blood flow in rats after severe cord trauma. *J Neurosurg,* 49**,** 844-53.

ROTHWELL, N., ALLAN, S. & TOULMOND, S. 1997. The role of interleukin 1 in acute neurodegeneration and stroke: pathophysiological and therapeutic implications. *J Clin Invest,* 100**,** 2648-52.

SALAND, S. K. & KABBAJ, M. 2018. Sex Differences in the Pharmacokinetics of Low-dose Ketamine in Plasma and Brain of Male and Female Rats. *J Pharmacol Exp Ther,* 367**,** 393-404.

SANDLER, A. N. & TATOR, C. H. 1976. Effect of acute spinal cord compression injury on regional spinal cord blood flow in primates. *J Neurosurg,* 45**,** 660-76.

SANTILLAN, A., NACARINO, V., GREENBERG, E., RIINA, H. A., GOBIN, Y. P. & PATSALIDES, A. 2012. Vascular anatomy of the spinal cord. *J Neurointerv Surg,* 4**,** 67-74.

SCHACHTRUP, C., LU, P., JONES, L. L., LEE, J. K., LU, J., SACHS, B. D., ZHENG, B. & AKASSOGLOU, K. 2007. Fibrinogen inhibits neurite outgrowth via beta 3 integrin-mediated phosphorylation of the EGF receptor. *Proc Natl Acad Sci U S A,* 104**,** 11814-9.

SCHAFFER, C. B., FRIEDMAN, B., NISHIMURA, N., SCHROEDER, L. F., TSAI, P. S., EBNER, F. F., LYDEN, P. D. & KLEINFELD, D. 2006. Two-photon imaging of cortical surface microvessels reveals a robust redistribution in blood flow after vascular occlusion. *PLoS Biol,* 4**,** e22.

SCHELLENBERG, A. E., BUIST, R., YONG, V. W., DEL BIGIO, M. R. & PEELING, J. 2007. Magnetic resonance imaging of blood-spinal cord barrier disruption in mice with experimental autoimmune encephalomyelitis. *Magn Reson Med,* 58**,** 298-305.

SEIF, G. I., NOMURA, H. & TATOR, C. H. 2007. Retrograde axonal degeneration "dieback" in the corticospinal tract after transection injury of the rat spinal cord: a confocal microscopy study. *J Neurotrauma,* 24**,** 1513-28.

SHARMA, H. S. 2005. Pathophysiology of blood-spinal cord barrier in traumatic injury and repair. *Curr Pharm Des,* 11**,** 1353-89.

SHARMA, H. S., WINKLER, T., STALBERG, E., OLSSON, Y. & DEY, P. K. 1991. Evaluation of traumatic spinal cord edema using evoked potentials recorded from the spinal epidural space. An experimental study in the rat. *J Neurol Sci,* 102**,** 150-62.

SHEN, Z., LU, Z., CHHATBAR, P. Y., O'HERRON, P. & KARA, P. 2012. An artery-specific fluorescent dye for studying neurovascular coupling. *Nat Methods,* 9**,** 273-6.

SHEPRO, D. & MOREL, N. M. 1993. Pericyte physiology. *FASEB J,* 7**,** 1031-8.

SHIELDS, D. C., SCHAECHER, K. E., HOGAN, E. L. & BANIK, N. L. 2000. Calpain activity and expression increased in activated glial and inflammatory cells in penumbra of spinal cord injury lesion. *J Neurosci Res,* 61**,** 146-50.

SHIOTSUKI, H., YOSHIMI, K., SHIMO, Y., FUNAYAMA, M., TAKAMATSU, Y., IKEDA, K., TAKAHASHI, R., KITAZAWA, S. & HATTORI, N. 2010. A rotarod test for evaluation of motor skill learning. *J Neurosci Methods,* 189**,** 180-5.

SHUMAN, S. L., BRESNAHAN, J. C. & BEATTIE, M. S. 1997. Apoptosis of microglia and oligodendrocytes after spinal cord contusion in rats. *Journal of Neuroscience Research,* 50**,** 798-808.

SIMS, D. E. 1986. The pericyte--a review. *Tissue Cell,* 18**,** 153-74.

SINGH, A., TETREAULT, L., KALSI-RYAN, S., NOURI, A. & FEHLINGS, M. G. 2014. Global prevalence and incidence of traumatic spinal cord injury. *Clin Epidemiol,* 6**,** 309-31.

SOHET, F. & DANEMAN, R. 2013. Genetic mouse models to study blood-brain barrier development and function. *Fluids Barriers CNS,* 10**,** 3.

SOROKIN, L. 2010. The impact of the extracellular matrix on inflammation. *Nat Rev Immunol,* 10**,** 712-23.

SRINIVASAN, M., SUDHEER, A. R. & MENON, V. P. 2007. Ferulic Acid: therapeutic potential through its antioxidant property. *J Clin Biochem Nutr,* 40**,** 92-100.

STREIT, W. J., CONDE, J. R., FENDRICK, S. E., FLANARY, B. E. & MARIANI, C. L. 2005. Role of microglia in the central nervous system's immune response. *Neurol Res,* 27**,** 685-91.

SUNG, J. H., GIM, S. A. & KOH, P. O. 2014. Ferulic acid attenuates the cerebral ischemic injury-induced decrease in peroxiredoxin-2 and thioredoxin expression. *Neurosci Lett,* 566**,** 88-92.

TAKESHITA, H., YAMAMOTO, K., NOZATO, S., INAGAKI, T., TSUCHIMOCHI, H., SHIRAI, M., YAMAMOTO, R., IMAIZUMI, Y., HONGYO, K., YOKOYAMA, S., TAKEDA, M., OGURO, R., TAKAMI, Y., ITOH, N., TAKEYA, Y., SUGIMOTO, K., FUKADA, S. I. & RAKUGI, H. 2017. Modified forelimb grip strength test detects aging-associated physiological decline in skeletal muscle function in male mice. *Sci Rep,* 7**,** 42323.

TANG, P., ZHANG, Y., CHEN, C., JI, X., JU, F., LIU, X., GAN, W. B., HE, Z., ZHANG, S., LI, W. & ZHANG, L. 2015. In vivo two-photon imaging of axonal dieback, blood flow, and calcium influx with methylprednisolone therapy after spinal cord injury. *Sci Rep,* 5**,** 9691.

TATOR, C. H. & FEHLINGS, M. G. 1991. Review of the secondary injury theory of acute spinal cord trauma with emphasis on vascular mechanisms. *J Neurosurg,* 75**,** 15-26.

TATOR, C. H. & KOYANAGI, I. 1997. Vascular mechanisms in the pathophysiology of human spinal cord injury. *J Neurosurg,* 86**,** 483-92.

TEI, R., KAIDO, T., NAKASE, H. & SAKAKI, T. 2005. Secondary spinal cord hypoperfusion of circumscribed areas after injury in rats. *Neurol Res,* 27**,** 403-8.

THRIVIKRAMAN, K. V., HUOT, R. L. & PLOTSKY, P. M. 2002. Jugular vein catheterization for repeated blood sampling in the unrestrained conscious rat. *Brain Res Brain Res Protoc,* 10**,** 84-94.

THRON, A. & ROSSBERG, C. 1988. *Vascular Anatomy of the Spinal Cord: Neuroradiological Investigations and Clinical Syndromes.,* New York, Springer.

TURNBULL, I. M. 1973. Chapter 5. Blood supply of the spinal cord: normal and pathological considerations. *Clin Neurosurg,* 20**,** 56-84.

UNGER, E. R., SUNG, J. H., MANIVEL, J. C., CHENGGIS, M. L., BLAZAR, B. R. & KRIVIT, W. 1993. Male donor-derived cells in the brains of female sex-mismatched bone marrow transplant recipients: a Y-chromosome specific in situ hybridization study. *J Neuropathol Exp Neurol,* 52**,** 460-70.

VASS, K., HICKEY, W. F., SCHMIDT, R. E. & LASSMANN, H. 1993. Bone marrow-derived elements in the peripheral nervous system. An immunohistochemical and ultrastructural investigation in chimeric rats. *Lab Invest,* 69**,** 275-82.

WALDMAN, S. A. & MURAD, F. 1988. Biochemical mechanisms underlying vascular smooth muscle relaxation: the guanylate cyclase-cyclic GMP system. *J Cardiovasc Pharmacol,* 12 Suppl 5**,** S115-8.

WALKER, M. J., WALKER, C. L., ZHANG, Y. P., SHIELDS, L. B., SHIELDS, C. B. & XU, X. M. 2015. A novel vertebral stabilization method for producing contusive spinal cord injury. *J Vis Exp***,** e50149.

WATERMAN, A. E. & LIVINGSTON, A. 1978. Effects of age and sex on ketamine anaesthesia in the rat. *Br J Anaesth,* 50**,** 885-9.

WATSON, C. 2009. *The spinal cord : a Christopher and Dana Reeve Foundation text and atlas,* Amsterdam, Elsevier.

WATSON, C. & KAYALIOGLU, G. 2009. Chapter 1 - The Organization of the Spinal Cord. *In:* WATSON, C., PAXINOS, G. & KAYALIOGLU, G. (eds.) *The Spinal Cord.* San Diego: Academic Press.

WESTERGAARD, E. & BRIGHTMAN, M. W. 1973. Transport of proteins across normal cerebral arterioles. *J Comp Neurol,* 152**,** 17-44.

WHETSTONE, W. D., HSU, J. Y., EISENBERG, M., WERB, Z. & NOBLE-HAEUSSLEIN, L. J. 2003. Blood-spinal cord barrier after spinal cord injury: relation to revascularization and wound healing. *J Neurosci Res,* 74**,** 227-39.

WILLIAMS, K., ALVAREZ, X. & LACKNER, A. A. 2001. Central nervous system perivascular cells are immunoregulatory cells that connect the CNS with the peripheral immune system. *Glia,* 36**,** 156-64.

WITCHER, K. G., EIFERMAN, D. S. & GODBOUT, J. P. 2015. Priming the inflammatory pump of the CNS after traumatic brain injury. *Trends Neurosci,* 38**,** 609-620.

WOLBURG, H., WOLBURG-BUCHHOLZ, K., FALLIER-BECKER, P., NOELL, S. & MACK, A. F. 2011. Structure and functions of aquaporin-4-based orthogonal arrays of particles. *Int Rev Cell Mol Biol,* 287**,** 1-41.

WU, W., LEE, S. Y., WU, X., TYLER, J. Y., WANG, H., OUYANG, Z., PARK, K., XU, X. M. & CHENG, J. X. 2014. Neuroprotective ferulic acid (FA)-glycol chitosan (GC) nanoparticles for functional restoration of traumatically injured spinal cord. *Biomaterials,* 35**,** 2355-2364.

WU, X. & XU, X. M. 2016. RhoA/Rho kinase in spinal cord injury. *Neural Regen Res,* 11**,** 23-7.

WU, X., ZHANG, Y. P., QU, W., SHIELDS, L. B. E., SHIELDS, C. B. & XU, X. M. 2017. A Tissue Displacement-based Contusive Spinal Cord Injury Model in Mice. *J Vis Exp*.

XU, F., HUANG, J., HE, Z., CHEN, J., TANG, X., SONG, Z., GUO, Q. & HUANG, C. 2016. Microglial polarization dynamics in dorsal spinal cord in the early stages following chronic sciatic nerve damage. *Neurosci Lett,* 617**,** 6-13.

YAN, Y., SUN, X. & SHEN, B. 2017. Contrast agents in dynamic contrast-enhanced magnetic resonance imaging. *Oncotarget,* 8**,** 43491-43505.

YASHON, D., BINGHAM, W. G., JR., FADDOUL, E. M. & HUNT, W. E. 1973. Edema of the spinal cord following experimental impact trauma. *J Neurosurg,* 38**,** 693-7.

ZHANG, Y. P., BURKE, D. A., SHIELDS, L. B., CHEKMENEV, S. Y., DINCMAN, T., ZHANG, Y., ZHENG, Y., SMITH, R. R., BENTON, R. L., DEVRIES, W. H., HU, X., MAGNUSON, D. S., WHITTEMORE, S. R. & SHIELDS, C. B. 2008. Spinal cord contusion based on precise vertebral stabilization and tissue displacement measured by combined assessment to discriminate small functional differences. *J Neurotrauma,* 25**,** 1227-40.

ZHAO, J., QIU, H., CHEN, D. L., ZHANG, W. X., ZHANG, D. C. & LI, M. 2013. Development of nanofibrous scaffolds for vascular tissue engineering. *Int J Biol Macromol,* 56**,** 106-13.

ZHONG, Z., DEANE, R., ALI, Z., PARISI, M., SHAPOVALOV, Y., O'BANION, M. K., STOJANOVIC, K., SAGARE, A., BOILLEE, S., CLEVELAND, D. W. & ZLOKOVIC, B. V. 2008. ALS-causing SOD1 mutants generate vascular changes prior to motor neuron degeneration. *Nat Neurosci,* 11**,** 420-2.

ZHOU, D., XIONG, L., WU, Q., GUO, R., ZHOU, Z., ZHU, Q., JIANG, Y. & HUANG, J. 2013. Effects of transmyocardial jet revascularization with chitosan hydrogel on channel patency and angiogenesis in canine infarcted hearts. *J Biomed Mater Res A,* 101**,** 567-74.

ZLOKOVIC, B. V. 2008. The blood-brain barrier in health and chronic neurodegenerative disorders. *Neuron,* 57**,** 178-201.

CURRICULUM VITAE

CHEN CHEN

Education

Ph.D. Medical Neuroscience

2012-2019.

Indiana University

Advisor: Xiao-Ming Xu, M.D., Ph.D.

B.S. Biotechnology

2010.

Indiana University – Bloomington

B.S. Biotechnology

2008.

Hunan Agricultural University

Changsha, Hunan, P.R. China

Publications

Ying Wang, Wei Wu, Xiangbing Wu, Yan Sun, Yi P Zhang, Ling-Xiao Deng, Melissa Jane Walker, Wenrui Qu, **Chen Chen**, Nai-Kui Liu, Qi Han, Heqiao Dai, Lisa BE Shields, Christopher B Shields, Dale R Sengelaub, Kathryn J Jones, George M Smith, and Xiao-

Ming Xu (2018). Remodeling of lumbar motor circuitry remote to a thoracic spinal cord injury promotes locomotor recovery. *eLife*, 7, e39016. doi:10.7554/eLife.39016

Chen Chen, Yi Ping Zhang, Yan Sun, Wenhui Xiong, Lisa B. Shields, Christopher B. Shields, Xiaoming Jin, Xiao-Ming Xu. (2017). An In Vivo Duo-color Method for Imaging Vascular Dynamics Following Contusive Spinal Cord Injury. *Journal of visualized experiments* (130), 56565. doi:10.3791/56565

Lingxiao Deng, Yiwen Ruan, **Chen Chen**, Christian Corbin Frye, Wenhui Xiong, Xiaoming Jin, Kathryn Jones, Dale Sengelaub, Xiao-Ming Xu (2015). Characterization of dendritic morphology and neurotransmitter phenotype of thoracic descending propriospinal neurons after complete spinal cord transection and GDNF treatment. *Experimental neurology*, *277*, 103-114.

Nai-Kui Liu, Yi-Ping Zhang, Jian Zou, Tom Verhovshek, **Chen Chen**, Qing-Bo Lu, Chandler L. Walker, Christopher B. Shields, Xiao-Ming Xu (2014). A semicircular controlled cortical impact produces long-term motor and cognitive dysfunction that correlates well with damage to both the sensorimotor cortex and hippocampus. *Brain Research*. 1576. 10.1016/j.brainres.2014.05.042.

Awards & Honors

2018. Best oral presentation speaker, 2018 International Neural Regeneration Symposium, 2018, July 26-29th, Guangzhou, China

2014. Outstanding Abstract in the joint symposium of 4th International Neural Regeneration Symposium (INRS2014), 6th International Spinal Cord Injury Treatment and Trials Symposium (ISCITT) and 9th Asia Pacific Symposium on Neural Regeneration (APSNR)

Grants & Fellowships

2017-2019 Indiana Spinal Cord & Traumatic Brain Injury Research Fund Grant Program, Indiana State Department of Health

Fellowship, Indiana University, Indianapolis, IN, USA (2011 - present)

Research Experiences

Graduate Research

2012- 2019.

Stark Neuroscience Research Institute, IUSM – Indianapolis,

Indianapolis, IN, 46202.

Ph.D. Project: *Targeting early vascular dysfunction after spinal cord injury*

Mentor: Xiao-Ming Xu, M.D., Ph.D.

Undergraduate Research

2010.

Dept. of Biology, Indiana University – Bloomington,

Bloomington, IN, 47405.

Lab teaching assistant

Research Project: Identification of Vancomycin in Bacillus subtilis strains.

Mentor: Nancy Magill, Ph.D.

May - August 2009.

Laboratory of Bio-Nanotechnology and Molecular Engineering, Hunan University, Changsha, Hunan, China.

Lab technician

2005 -2008.

Botanical Laboratory, Hunan Agricultural University

Changsha, Hunan, China

B.S. Research Project: Optimization of tissue culture and rapid propagation of *Melastoma dodecandrum*

Conferences Posters & Presentations

- Chen, C., Xu, X.M. Targeting towards Early Vascular Responses following Contusive SCI. Poster session presented at the 47th Society for Neuroscience Annual Meeting; 2017 November 11-15th, Washington, DC

- Chen, C., Zhang, Y.P., Sun, Y., Shields, C.B., Xiong W., Jin, X., and Xu X.M. In vivo Observation of Acute Vascular Dysfunction following Spinal Cord Injury. Poster session presented at the 46th Society for Neuroscience Annual Meeting; 2016 November 12-16th; San Diego, CA

- Sun, Y., Bradley, R., Deng L., Chen, C., Ruan Y., Wu, W., Qu W., Zhang Y.P., Shields, C.B., Zhang, S.C., Xu, X.M. Transplantation of Human Embryonic Stem Cells-Derived Immature Astrocytes Promotes Long-term Survival and Functional Recovery after Spinal Cord Injury. Poster session presented at the 46th Society for Neuroscience Annual Meeting; 2016 November 12-16th; San Diego, CA

- Powerpoint presentation at the 34th Annual Symposium of the National Neurotrauma Society; 2016 June 26-29th; Lexington, KY

Invited Talks

- Title: *In vivo* imaging of vascular injury following SCI. 24th annual KSCHIRT Symposium, 2018, May 10th, Lexington, KY

- Title: Targeting vascular disruption following SCI. 2018 International Neural Regeneration Symposium, 2018, July 26-29th, Guangzhou, China